

DIRECTIONAL RECORDING OF SWELL FROM DISTANT STORMS

BY W. H. MUNK, G. R. MILLER, F. E. SNODGRASS AND N. F. BARBER

*Institute of Geophysics and Planetary Physics, University of California, La Jolla**(Communicated by G. E. R. Deacon, F.R.S.—Received 19 April 1962)*

[Plate 7]

CONTENTS

	PAGE		PAGE
1. INTRODUCTION	506	(e) Analysis by iteration	528
2. INSTALLATION	507	(f) Fourier-Bessel analysis	531
(a) Site	507	(g) Other methods	533
(b) Method of installation	509	8. RESULTS	540
(c) The Vibrotron pressure transducer	509	9. REFRACTION	543
(d) Recording	510	10. REFLEXION	549
3. SAMPLE RECORDS	512	11. IDENTIFICATION OF INDIVIDUAL EVENTS	551
4. DIGITAL ANALYSIS	512	(a) The hurricane of 23 October	556
(a) The detection of errors	512	(b) Antipodal swell	557
(b) 'Aliasing' and hydrodynamic filtering	512	(c) The quickly moving storm of 12·4 May	558
(c) Suppression of tides	513	(d) The end of the storm season	561
(d) The spectral matrix	513	(e) Narrow beams and sharp ridges	561
(e) The reliability of the computed spectra	514	(f) A discrepancy in wave direction?	562
5. FIRST INFERENCE	515	12. AN EXPERIMENT IN HETERODYNING	562
(a) Sample spectrum	515	(a) Removal of frequency shift	562
(b) Power spectra	515	(b) Heterodyne theory	563
(c) Direction finding	515	(c) The results	564
(d) Beam width	517	13. GENERATION AND DECAY	565
(e) Dispersion	518	(a) Ridge cuts	565
(f) Effect of finite depth on ridge lines	519	(b) Geometric spreading	566
6. GENERAL THEORY OF ARRAYS	520	(c) Attenuation	567
(a) Elementary wave trains	520	14. MEAN MONTHLY SPECTRA	567
(b) The spectrum	521	15. SCATTER AND ABSORPTION	571
7. INTERPRETATION OF THE CROSS-SPECTRAL MATRIX	523	(a) The evidence	571
(a) Conventional treatment	523	(b) Scattering by waves	572
(b) A best-fitting single wave train	524	(c) Scattering by turbulence	575
(c) A best-fitting pair of wave trains	526	(d) Island scattering	576
(d) Experimental test of the dispersion law	527	(e) Absorption	580
		16. THE SOUTHERN SWELL	581
		REFERENCES	583

We have measured the distribution of wave energy with frequency and direction for several months, and attempted to interpret the resulting field $E(f, \theta, t)$ in terms of pertinent geophysical processes. The fluctuating pressure on the sea bottom was measured with a triangular array of sensitive transducers located 2 miles off shore from San Clemente Island, California, at a depth of 100 m. The transducer output was brought ashore by undersea cable and telemetered to the laboratory at La Jolla, California, where it was digitally recorded. The analysis by means of high-speed computers consists of two distinct steps: (i) computing the spectral matrix $S_{ijk} = C_{ijk} + iQ_{ijk}$ between the records $x_i(t)$ and $x_j(t)$ ($i, j = 1, 2, 3$) at frequency k ($k = 1, 2, \dots, 100$); C_{ijk} , Q_{ijk} are the co- and quadrature spectra, and $S_{iik} = C_{iik}$ the ordinary power spectra of the three records; (ii) interpreting S_{ijk} in terms of the energy spectrum in frequency and direction (or equivalently in horizontal wave-number space). The problem is discussed in some detail. The method adapted is to find the energy and direction of a point source which can best account (in the least-square sense) for S_{ijk} ; to compute the matrix S'_{ijk} associated with this optimum point source; then to find the optimum point source of the 'residual matrix' $S_{ijk} - \gamma S'_{ijk}$ (we chose $\gamma = 0.1$), etc, for 100 iterations, or until the residual matrix vanishes. The calculation is made independently for each frequency. The iterative point-source method is satisfactory if the incoming radiation is associated with one or two strong sources.

From daily measurements over several months we obtain $E(f, \theta, t)$. The non-directional spectra, $E(f, t) = \int E(f, \theta, t) d\theta$ are contoured, and show pronounced slanting ridges associated with the dispersive arrivals from individual storms. Their slope and intercept give the distance and time of the source, respectively; the energy density along the ridge is associated with the wind speed, the width of the ridge with the storm duration, and the variation of width with the rate at which the storm approaches the station. The distribution of energy with direction along these ridge lines give the direction of the source (after correction for local refraction), some upper limit to source aperture and an indication of its motion normal to the line-of-site. With distance, direction, time and five other source characteristics thus derived from the wave records, the sources are fairly well specified. Comparison with weather maps leads to fair agreement in most instances. From June to September most sources lie in the New Zealand–Australia–Antarctic section or in the Ross Sea. In three instances the swell was generated in the Indian Ocean near the antipole and entered the Pacific along the great circle route between New Zealand and Antarctica. By October the southern winter has come to an end and the northern hemisphere takes over as the chief region of swell generation.

Antarctic pack ice may be a factor, by narrowing the 'window' between Antarctica and New Zealand or by impairing storm fetches in the Ross Sea. The northward travelling swell is further impaired by dense island groups in the South Pacific, and an attempt is made to estimate the resulting scattering. The recorded spectrum at frequencies below 0.05 c/s is in rough accord with what would be expected from typical storms after due allowance for geometric spreading; at higher frequencies the spectrum fails to rise in the expected manner. A resonant interaction between the swell and the trade wind sea may be responsible for back-scattering frequencies above 0.05 c/s. The observed widths of the beam (< 0.1 radian) and of the spectral peak ($\Delta f/f < 0.1$) put an upper limit on forward scattering over the transmission path of 10^4 wavelengths, and thus place some restriction on the energy of turbulent eddies with dimensions of the order of 1 km in the shallow layers of the sea. Finally, a comparison of mean monthly wave spectra with those from individual storm permits us to estimate the absorption time of the North Pacific basin. The resultant value of $\frac{1}{2}$ week is not inconsistent with the assumption that most of the swell energy is absorbed along the boundaries. The inferred coastal absorption is roughly in accord with what we found at San Clemente Island (beach slope 1:30): the coast line changes from a predominantly reflecting to a predominantly absorbing boundary as the frequency increases from 0.03 to 0.05 c/s.

1. INTRODUCTION

Almost fifteen years ago in the pages of this Journal, one of us presented power spectra of ocean waves and swell off Pendeen and Perranporth in north Cornwall (Barber & Ursell 1948). The outstanding feature of these spectra is the successive shift of peaks toward higher frequencies. This is the expected behaviour of dispersive wave trains from rather

well-defined sources. Storms generate a broad spectrum of frequencies; the low frequencies are associated with the largest group velocity and accordingly are the first to arrive at distant stations. The time rate of increase in the frequency of peaks determines the distance and time of origin. In this way Barber & Ursell were able to identify the dispersive arrivals with a low pressure area in the North Atlantic, a tropical storm off Florida, and a storm off Cape Horn, at distances of 1200, 2800, and 6000 miles, respectively, from the Cornish stations. The measurements were consistent with the simple classical result that each frequency, f , is propagated with its appropriate group velocity, $V = g/(4\pi f)$.

The present study is in a sense a refinement to the work of Barber & Ursell. The frequency resolution and sensitivity have each been increased by an order of magnitude, and this makes it possible to detect and resolve meteorological sources that have previously been out of reach. The antipodal swell from the Indian Ocean is a case in point.

Another feature of the present experiments is the use of an instrument array for determining the direction of travel of swell. The use of an array or its equivalent is not of course entirely new even in the study of sea waves (see Barber 1954; Barber & Doyle 1956; Cartwright 1962) but the present use of very sensitive and reliable instruments and the digital processing of the data have made it possible to determine the direction of travel of swell to within a few degrees even when its height is only a few millimetres. The use of three instruments makes it possible to distinguish between swell coming directly from the storm and swell that may have been scattered or reflected from a nearby coast. Three instruments serve also to discriminate between two or even three storm centres giving energy in the same frequency band. Probably no more detailed resolution is necessary in studies of ocean swell. It seems likely that the techniques of digital processing and analysis used in the present experiments might profitably be applied to studies of seismic noise.

2. INSTALLATION

(a) Site

Three Vibrotron pressure gauges were installed in an array on the seaward side of San Clemente Island, 60 miles due west of San Diego, California. As shown in figure 1, two of the gauges were installed along a line more or less parallel to shore and the third gauge to the seaward. The instruments form approximately an equilateral triangle with sides of about 900 ft. The distance from shore is 10 000 ft. and the depth at the site is relatively uniform at 55 fathoms (~ 100 m).

Each of the three gauges was connected by an 8000 ft. length of twisted-pair cable to a junction box 3000 ft. from shore in 100 ft. of water. From this point a single, heavily armoured, multiconductor cable carried the signals to shore. Other twisted-pair cables then carried the signal three miles inland to a telemetering tower on the island's ridge, 900 ft. above sea level.

At the tower the three signals were amplified, filtered, and added. The combined signals modulated the carrier of a 100 W f.m. transmitter operating at a frequency of 150 Mc/s. The radio signals were transmitted line-of-sight to a receiver on Mt Soledad in La Jolla. Commercial telephone lines coupled to the output of the radio receivers carried the signal from Mt Soledad to the laboratory at Scripps Institution of Oceanography. Specially

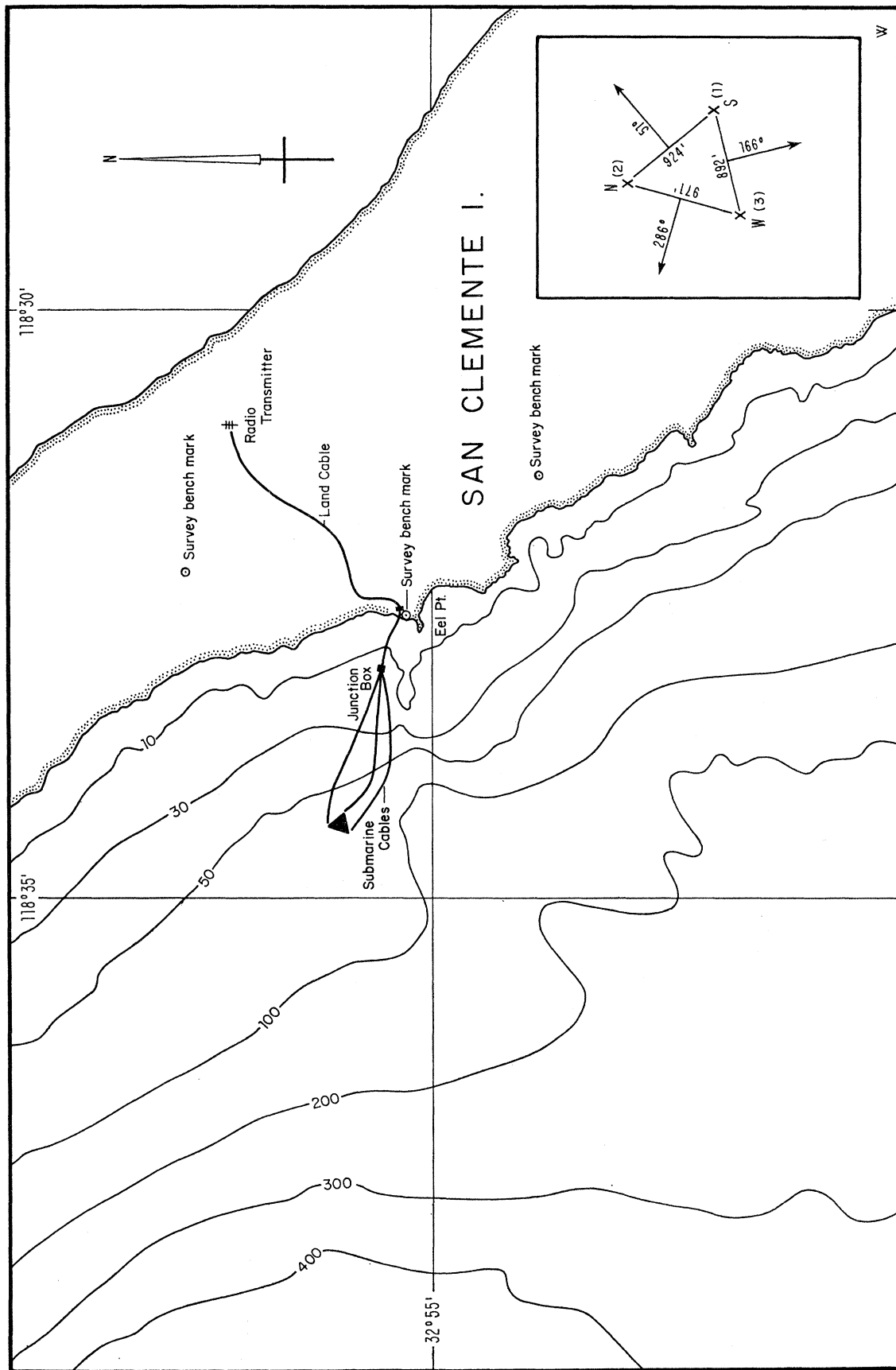


FIGURE 1. The site of the western side of San Clemente Island. Depth contours in fathoms. The dimensions of the triangular array are given in the inset.

designed band-pass filters separated the three Vibrotron signals. The separated signals were amplified and applied to the input of frequency-measuring instruments. The principal output is in the form of punched paper tape. To allow easy supervision, pen recordings (figures 2 and 3) were also made, and the digital output was printed as well as punched.

(b) *Method of installation*

The uncertainty of the location of the instruments introduces an uncertainty into the computed bearings of the waves. We wished to keep this uncertainty to less than 1° . This corresponds to an uncertainty of 100 nautical miles in the location of a source in the New Zealand area. In turn, the positions of the instruments on the sea bottom need to be known to within 10 ft. After a few unsuccessful attempts to meet this requirement, the following procedure was found satisfactory.

First we established three marker buoys, and these remained in position throughout the experiment. Each consisted of a 500 lb. steel anchor, a plastic-coated steel cable $\frac{5}{16}$ in. in diameter, and a double galvanized buoy about 3 ft in diameter which would be submerged to a depth of 100 ft. Specially designed non-metallic fittings were used to connect the cable to the anchor and to the buoy to avoid electrolysis between different metals. Floating spar buoys made of aluminum tube 3 in. in diameter and carrying flags were temporarily attached to the submerged buoys.

Powerful optical azimuth instruments were set up on the island at three well separated surveyed positions. The spar buoys were then located from shore to establish their positions within 10 ft. The buoys and anchors were moved until their positions were found satisfactory. Wind and sea would deflect the surface spar buoys relative to the positions of their anchors, but this deflexion was presumed to be the same for each one. The relative positions of the anchors were therefore known.

Each instrument, on the end of its electric lead, was then installed by a SCUBA (self-contained underwater breathing apparatus) diver who carried it down to the submerged buoy and shackled it loosely to the cable below. This shackle had a soluble magnesium link that would dissolve in 24 h. The instrument was then allowed to slide freely down to the sea bed where it was certain to lie within 2 ft of the anchor. The soluble link ensured that the instrument would later be free and could, when necessary, be recovered on its cable without disturbing the anchor and marker buoy. The ship then laid out the light-weight electric cable towards the shore and joined it to the cable from shore at the off-shore junction box (figure 1).

The temporary spar buoys were then removed since they could not be expected to survive long at sea. A SCUBA diver with a 'swimmer-carried SONAR' can readily rediscover a submerged buoy, provided he is guided to the proximity with the help of survey instruments ashore.

(c) *The Vibrotron pressure transducer*

The Vibrotron pressure transducer was originally developed by the Southwest Research Institute and is now being manufactured by the Borg-Warner Corporation, Santa Ana, California. The transducer has repeatedly been described in the literature (Poindexter 1952; Ohman 1955; Prast, Calhoun, Hartloff & Liske 1955; Snodgrass 1958), and we shall review only the essential features.

The gauge is constructed so that pressure signals vary the frequency of a wire vibrating in a magnetic field. The a.c. voltage induced in the vibrating wire can be amplified, transmitted, and recorded with all the advantages normally attributed to frequency modulation systems. The vibrating wire, which is a tungsten filament a few thousandths of an inch in diameter and a length of less than $\frac{1}{2}$ in., is stretched between a rigid support and a small diaphragm exposed to the pressure. The wire, magnets, and support structure are encased in an evacuated cylinder $\frac{3}{4}$ in. in diameter and approximately $3\frac{1}{2}$ in. in length with electrical connexions at one end and the diaphragm and pressure port at the other. As the pressure increases, the diaphragm is deflected inward, diminishing the tension in the wire and decreasing its natural frequency.

The vibrating wire and a second non-vibrating wire are connected in a bridge which is roughly balanced to d.c. voltages. The output of the bridge, being essentially the a.c. voltage induced in the vibrating wire, is amplified and fed back to the bridge in a sense required to maintain the wire in oscillation. A transistorized amplifier with a gain of 5000 and an output of 2 V provides the required feedback and gives sufficient power for output circuits. With proper impedance-matching transformers the output signal can be transmitted over several miles of cable. D.c. power (24 V at 4 mA) is fed to the Vibrotron gauge through the same two conductors that are used for the return signal.

The frequency of vibration of the wire depends slightly on the amplitude of its vibration. A constant amplitude of vibration is achieved by allowing the amplifier to overdrive in its last stage. The resulting distortion in output waveform is not troublesome. Harmonics do not cause transmission problems since multiplexing is not used. Measurement of the signal frequency depends only upon the number of cycles (zero crossings) and this is unaffected by waveform distortion except in extreme cases. Extreme distortion is satisfactorily corrected with simple filters.

(d) *Recording*

Laboratory calibration of the Vibrotron gauge indicates that the frequency, f , varies with pressure, p , according to the characteristic equation $f^2 = -Ap + B$. Variations in frequency associated with waves and tides amount to less than 1 % of the mean frequency; accordingly with good approximation the gauge sensitivity

$$\frac{df}{dp} = -\frac{A}{2f} \approx -\frac{A}{2\bar{f}}$$

can be taken as constant over the range of the experiment.

Typically our Vibrotron gauges had a pressure range of 150 m (0 to 220 Lb./in.²) with a corresponding frequency range of 19 to 10 kc/s. At the 100 m installation depth, a sensitivity of about 0.4 (c/s)/cm of water was obtained with the gauge operating near 12 kc/s.

To obtain adequate precision, we recorded the number of microseconds (by means of a precision quartz crystal) during a 'gate' interval determined by 10 000 Vibrotron oscillations (more precisely, 20 000 zero crossings). An increment by one count then corresponds to about $\frac{1}{2}$ mm of water pressure. This precision is adequate for the present purpose. The noise level of the instrument has been studied by recording the output from a Vibrotron in its usual location on the sea bottom, but with the pressure port capped. The analysis of this

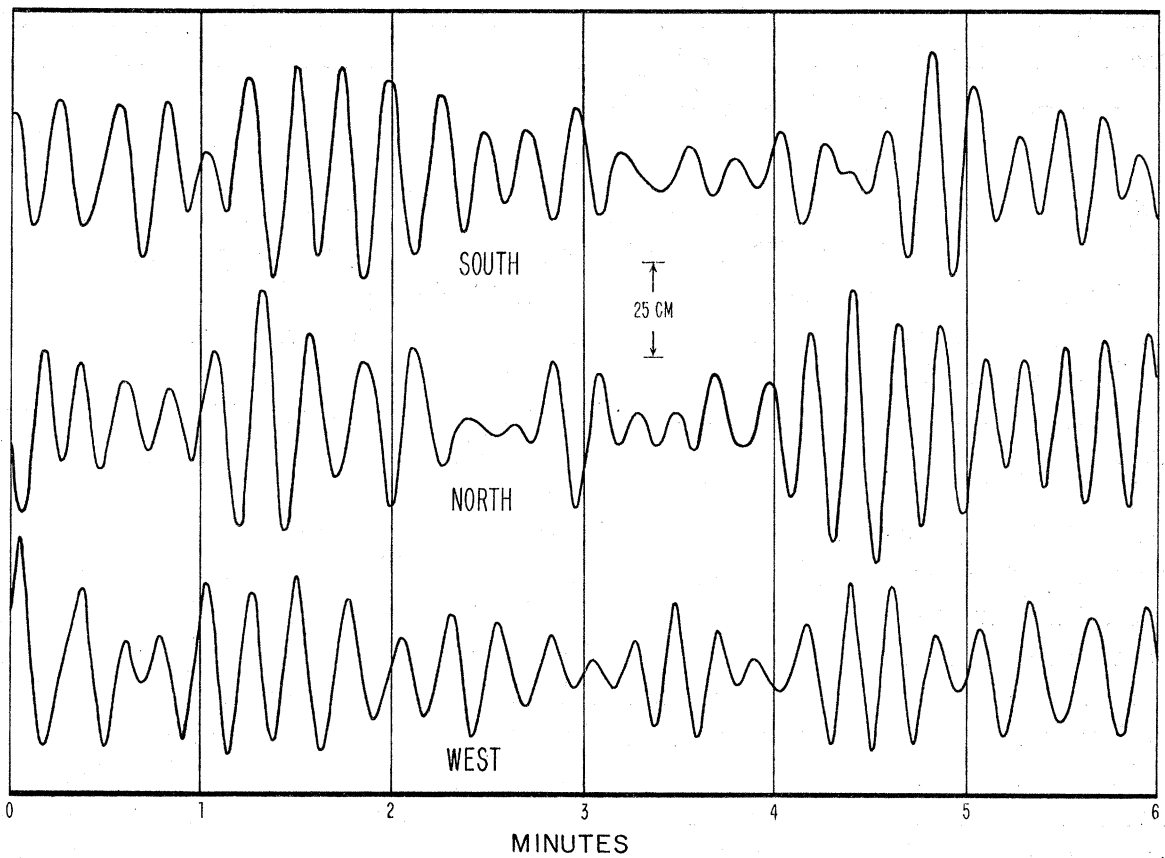


FIGURE 2. A 6 min sample of the record of 26 October 1959. The spectrum for this day (figure 4) shows a low peak at 36 c/ks (period 28 s), a higher peak at 50 c/ks (period 20 s), and a further rise toward higher frequencies.

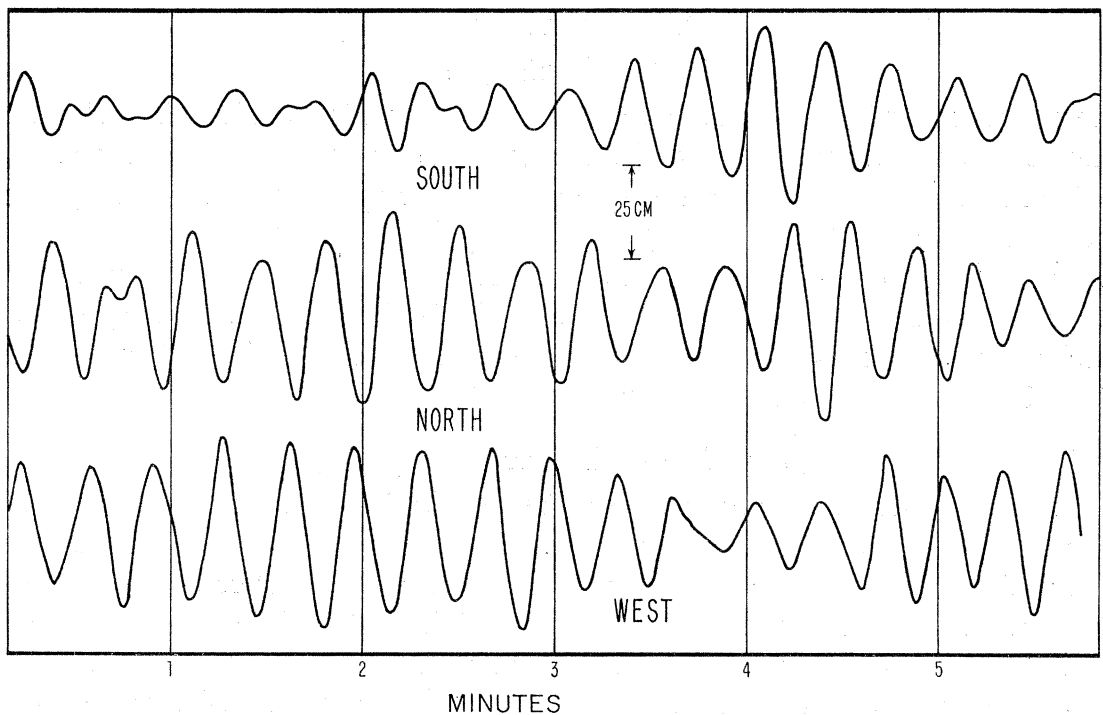


FIGURE 3. A 6 min sample of the record of 27 October 1959. The spectrum for this day (figure 5) shows a pronounced peak at 47 c/ks (period 21 s).

'zero-input' time series was performed in just the same manner as the analysis of actual wave records. It is found that at the frequencies of the sea and swell the noise spectrum is substantially below the recorded spectrum.

3. SAMPLE RECORDS

Figures 2 and 3 show 6 min record samples on two consecutive days. The corresponding spectra are plotted in figure 5. The essential feature is a very rapid development of peak A associated with a hurricane 3000 miles to the west. The energy in this peak increases by a factor of 100 in one day: On 26 October 1959 (figure 2) the record is dominated by the interference of relatively high-frequency waves from various sources, whereas on 27 October (figure 3) the hurricane swell (period ~ 21 s) dominates the record. There is no simple phase relation between the recordings from the three instruments. In figure 2 at the 1 min mark all records are approximately in phase; whereas at the 2 min mark, south and north are out of phase and west is in quadrature. In figure 3 north and west are active during the first 2 min; whereas south is inactive. This lack of consistency is altogether typical of many records that have been examined. At the actual time of recording we would often observe the three pen movements and attempt to infer the directions of the principal wave trains. Sometimes we could agree on a first-order estimate, only to find that a few minutes later the situation appeared to have changed. Yet a situation such as the one during 26 to 28 October is quite simple and well sorted out by analysis. It is found that the features can be accounted for by waves from two sources: a distant source to the south on about 18 October and a nearby source to the west on 22 October. Apparently it is difficult to disentangle correlations by visual inspection except in the most simple of circumstances. As we proceed to develop our method, the situation shown by figures 2 and 3 will continue to serve as illustration.

4. DIGITAL ANALYSIS

(a) *The detection of errors*

The present study involved the recording and analysis of something like 10^6 numbers. Of these, about one in a thousand was in error for some reason or another. It is characteristic of digital recording that errors are large, so large that a single error completely destroys the information contained in the analysis.

The first step of the analysis was for the digital computer to examine the first differences and to point out when these exceeded some specified limit. The faulty values were replaced by interpolated values. This simple procedure proved adequate. The principal source of errors was interference in the telemetering link.

(b) *'Aliasing' and hydrodynamic filtering*

Any oscillations whose frequency exceeds the Nyquist frequency (one-half the sampling frequency) will be indistinguishable from some lower frequency. Tukey calls this effect 'aliasing'. It is an inevitable consequence of the digital process. Heterodyning of the signal with the sampling frequency results in spurious (or 'aliased') signals at the difference frequency. To avoid aliasing one must make sure that the energy density above the Nyquist frequency is everywhere small as compared to the energy density within the frequency range of interest.

Pressures at all three instruments were sampled once every 4 s. This was the limiting speed of the punched paper tape equipment. The Nyquist frequency is half of this sampling frequency, or one cycle in 8 s = 125 cycles per kilosecond (c/ks). One must ensure that there is negligible power at frequencies higher than 125 c/ks. This was accomplished by placing the instruments on the bottom at a depth of 100 m. The resulting 'low-pass filtering' was then adequate for our purpose.†

Let $\rho g a \cos(2\pi ft)$ designate the pressure fluctuation at a fixed depth just beneath the surface, resulting from a wave of amplitude a and frequency f . Then the associated pressure fluctuation on the sea bottom at depth h is $r\rho g a \cos(2\pi ft)$, where

$$r(f, h) = \frac{1}{\cosh(2\pi kh)}, \quad 2\pi f^2 = gk \tanh(2\pi kh), \quad (4.1)$$

with $k(f, h)$ denoting the reciprocal of wavelength.‡ The following table gives a few selected values:

period (s)	100	40	20	13.3	10	8
f (c/ks)	10	25	50	75	100	125
$r^2(f, 100 \text{ m})$	0.99	0.76	0.30	0.04	0.0016	4×10^{-6}

The attenuation of the frequencies higher than 125 c/ks is therefore sufficient to avoid appreciable aliasing at the frequencies of interest, 100 c/ks and less.

All bottom spectra have been divided by $r^2(f)$ to yield surface spectra.

(c) *Suppression of tides*

Tides introduce high energy into low frequencies, and this gives rise to undesirable side bands. By using a numerical convolution, the tidal energy was reduced by a factor 10^4 before spectral analysis. The effect of the filter at the lowest two computed frequency bands is as follows:

f (c/ks)	1.25	2.5
energy response	0.263	0.998

At higher frequencies the effect of filtering is altogether negligible. For further details we refer to Munk, Snodgrass & Tucker (1959).

(d) *The spectral matrix*

The spectral analysis of the edited and filtered records was performed numerically on an IBM 709 at the Western Data Processing Center of the University of California, Los Angeles. The procedure for single records has been discussed by Blackman & Tukey (1958). The cross-spectral analysis between different records follows along quite similar lines, and a collection of pertinent formulae can be found§ in Munk *et al.* (1959). Here we shall merely indicate the principles of the analysis.

† A depth of this order also satisfied the requirement that the refractive turning of the wave train should be small (see 9(a), Refraction).

‡ The term wave number means the reciprocal of wavelength throughout the present paper and not $2\pi k$ as is the usage in some texts.

§ One change in notation has been found advisable: the present τ corresponds to $-\tau$ in the reference.

Let $\eta_r(t)$, $\eta_s(t)$ designate any two time series. The time average

$$\rho_{rs}(\tau) = \overline{\eta_r(t) \eta_s(t+\tau)}. \quad (4.2)$$

is called the covariance of the two series, and

$$\left. \begin{aligned} C_{rs}(f) &= \int_{-\infty}^{\infty} \rho_{rs}(\tau) \cos 2\pi f\tau \, d\tau, \\ Q_{rs}(f) &= \int_{-\infty}^{\infty} \rho_{rs}(\tau) \sin 2\pi f\tau \, d\tau, \end{aligned} \right\} \quad (4.3)$$

are associated co- and quadrature spectra. For the special case of $r = s$ we have $Q_{rr}(f) = 0$, and $C_{rr}(f)$ is then known as the power spectrum.

In general we may wish to refer to the cross-spectral matrix

$$S_{rs}(f) = C_{rs}(f) - iQ_{rs}(f). \quad (4.4)$$

In our case we perform all possible cross-spectra between the records from the three instruments (figure 1). The result can be visualized as a 3×3 complex matrix, $S_{rs}(f)$, at each frequency band. The matrix is Hermitian, $S_{rs} = S_{sr}^*$. The three diagonal terms are real and represent the power spectra. This leaves nine real numbers to describe the matrix at each frequency. But the three power spectra are essentially identical, so that there are only seven independent numbers at each frequency band.

In the case of a triangular array it is convenient to adopt a single subscript notation (this would not be convenient for more elaborate arrays):

$$\left. \begin{aligned} \text{spectrum:} & \quad C_0 = (C_{SS} C_{NN} C_{WW})^{\frac{1}{3}}, \\ \text{co-spectra:} & \quad C_1 = C_{NW}, \quad C_2 = C_{WS}, \quad C_3 = C_{SN}, \\ \text{quadrature spectra:} & \quad Q_1 = Q_{NW}, \quad Q_2 = Q_{WS}, \quad Q_3 = Q_{SN}, \end{aligned} \right\} \quad (4.5)$$

where the subscripts S, N, W, refer to the three instruments (inset, figure 1). The symmetry of the notation is apparent. The cross-spectral matrix is made up from seven independent parameters at each frequency band $C_0, C_1, C_2, C_3, Q_1, Q_2, Q_3$. For each day's recording the parameters were computed for 101 frequency bands, extending in equal intervals from zero frequency to 125 c/ks. The resulting 707 numbers are the starting point of all subsequent analyses.

For plotting the results one usually finds it more satisfactory to refer to the coherence, R , and the phase, ϕ , defined by

$$\left. \begin{aligned} C_{rs}(f) &= [C_{rr}(f) C_{ss}(f)]^{\frac{1}{2}} R_{rs}(f) \cos \phi_{rs}(f), \\ Q_{rs}(f) &= -[C_{rr}(f) C_{ss}(f)]^{\frac{1}{2}} R_{rs}(f) \sin \phi_{rs}(f), \end{aligned} \right\} \quad (4.6)$$

so that

$$R_{rs} e^{i\phi_{rs}} = \frac{C_{rs} - i Q_{rs}}{(C_{rr} C_{ss})^{\frac{1}{2}}}.$$

With this convention, $\phi_{rs}(f)$ is the phase of $\eta_s(t)$ minus the phase of $\eta_r(t)$ at frequency f .

(e) *The reliability of the computed spectra*

A typical record consisted of $3\frac{1}{2}$ h of values at intervals of $\Delta t = 4$ s, or a total of about 3000 values. Spectral estimates were obtained at frequencies

$$j\Delta f, \quad j = 0, 1, \dots, m, \quad \Delta f = (2m\Delta t)^{-1}.$$

We used $m = 100$, $\Delta t = 4$ s; hence $\Delta f = 1.25$ c/ks. The degrees of freedom associated with

the spectral values equal twice the number of data points divided by m , or about 60. For 60 degrees of freedom there is a 95 % probability that the true spectral value lies between 0.7 and 1.5 times the computed value.

5. FIRST INFERENCE

In this section we discuss the elementary interpretation of cross-spectra from a single instrument pair. This prepares the way for the general array theory in §6. In addition it provides the basis for the analysis of the earlier records, based on the north-south pair of instruments only.

(a) *Sample spectrum*

Figure 4 illustrates a sample spectrum. This includes the power spectra for the south and north instruments, the relative coherence and phase, and the directions inferred from the phase. The spectra were computed up to 125 c/ks, but the plots extend only to 90 c/ks. Similar plots were prepared for each day. During October 1959 a third instrument was installed, and three such diagrams were prepared for each day of recording, giving the corresponding relations between the south and north instruments, the north and west instruments, and the west and south instruments, respectively. To keep the reduction of the observations from becoming too much of a chore, all steps in this operation, including the plotting were done by machines.

The plotted spectra are useful for purposes of illustrating the analysis, and they permit some early inferences to be drawn. In fact it is found that the computed spectra are not the end, but rather a starting point for further analysis, the goal being an estimate of $E(f, \theta, t)$, the time-variable distribution of energy as a function of frequency and direction. Accordingly the machine was programed to provide the spectral matrix on punched cards in a form suitable for further machine calculations.

(b) *Power spectra*

The spectra of the sample are corrected for water depth in accordance with (4.1). The power spectra are alike in all essential details, as they should be. The essential features are a flat spectral level of about $0.01 \text{ cm}^2/(\text{c/ks})$ at frequencies below 30 c/ks; a peak at 38 c/ks, a second peak at 52 c/ks, and a gradual rise to a relatively flat spectral level between 10 and $100 \text{ cm}^2/(\text{c/ks})$ for frequencies above 70 c/ks.

(c) *Direction finding*

We note that for peak A the north and south instruments are virtually in phase. This would indicate that the wave crests are nearly parallel with the line connecting the two instruments. The direction normal to the instrument line is 231° T (figure 1, inset), so we conclude that the waves are approaching either from the open ocean to the south-west or from the shore of the island to the north-east; one might receive waves from the shore if the shore were a good reflector. For peak B, the records have a phase difference which shows that wave crests pass over the south instrument first. They may be coming from the ocean to the south or from the shore to the east. Such ambiguities in direction are inherent in any two-point array; our choice of a three-point array was precisely to remove this ambiguity and so permit us to estimate the amount of reflected energy.

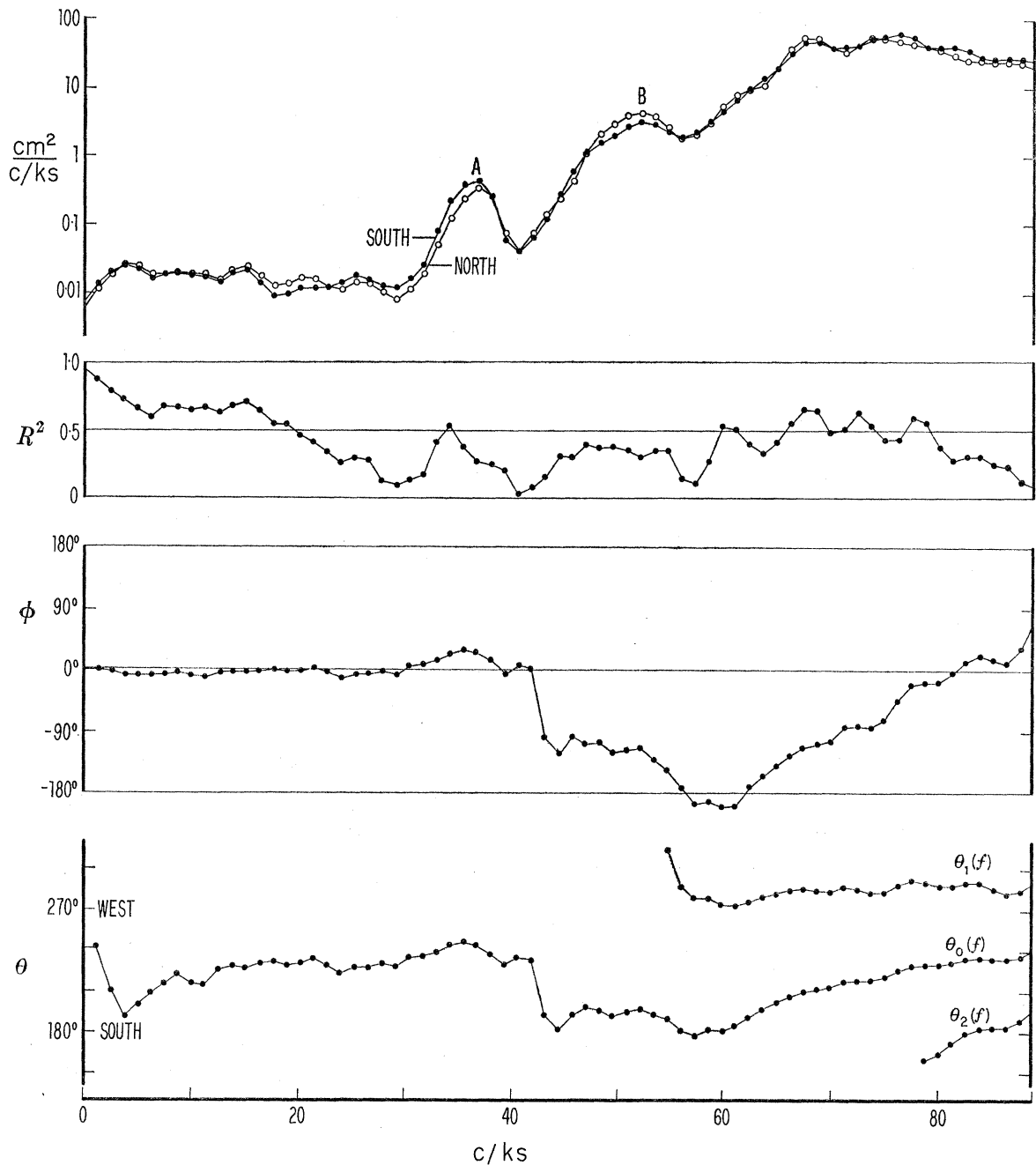


FIGURE 4. The upper curves show the surface spectra from the north and south instruments, respectively, for 26 October 1959. The next curve gives coherence, R^2 , and the third curve, the phase lead, ϕ , of the north instrument relative to the south instrument. The bottom curves show the direction(s) of a single point source on the seaward side of the array consistent with the observed phase, $\phi(f)$.

Consider an elementary wave train of frequency f from direction α measured clockwise relative to the instrument normal (231° T). The resulting signal at the south and north instruments can be written

$$\eta_S = A \cos(2\pi ft - \phi), \quad \eta_N = A \cos 2\pi ft, \quad (5.1)$$

respectively, where

$$\phi = 2\pi kD \sin \alpha \quad (5.2)$$

is the phase difference between the two instruments which are separated by a distance D . So there are always two possible wave directions, namely α and $180^\circ - \alpha$ that suit our observed phase difference ϕ .

The directions plotted at the bottom of figure 4 were computed from ϕ in accordance with (5.2) but adopting in each case only the direction from the seaward side of the instrument pair. For each computed value of α there is an additional solution $\alpha' = 180^\circ - \alpha$, so that for each computed direction, $\theta = 231^\circ + \alpha$, as plotted, there is another possible direction $\theta' = 282^\circ - \theta$, from the shoreward side of the array.

A further ambiguity arises when the waves are so short that the difference in phase at the two instruments exceeds half a cycle†. In comparing records one can estimate only the principal value of ϕ , that is, its value in the range $\pm\pi$. Its actual value may differ from this by any multiple of 2π . So there may be numerous possible values of the direction α , given by

$$\sin \alpha_j = (\phi + 2\pi j)/(2\pi kD), \quad (5.3)$$

where j is 0, ± 1 , ± 2 , etc., up to the largest value for which $\sin \alpha_j$ still lies between ± 1 .

The directions plotted at the bottom of figure 4 were computed in accordance with (5.3), ignoring those directions from the landward side of the pair of instruments. The direction is unique for frequencies below 55 c/ks, but two solutions and then three solutions appear as one moves to higher frequencies. For the higher frequencies it seems reasonable to adopt the curve of directions that is continuous with the unique curve of directions at the lower frequencies. In figure 4, $\theta_0(f)$ is the obvious choice between the three possible directions at the high-frequency limit. In practice we have found it possible to determine wave directions for wavelengths as short as $\frac{1}{2}D$ (as compared to the limit $2D$ for experiments conducted at a single frequency). This illustrates the benefit of working in a frequency continuum.

(d) Beam width

The coherence R is a guide to the angular spread of the waves. Consider for instance two wave trains having the same amplitude, a , but slightly different frequencies, f_1 and f_2 , coming from directions α_1 and α_2 respectively, relative to the normal of the pair of instruments. The corresponding phase differences are ϕ_1 and ϕ_2 , where

$$\phi_1 = 2\pi k_1 D \sin \alpha_1, \quad \phi_2 = 2\pi k_2 D \sin \alpha_2.$$

Thus the wave signals at the instruments may be written

$$\begin{aligned} \eta_N &= a \cos 2\pi f_1 t + a \cos 2\pi f_2 t, \\ \eta_S &= a \cos (2\pi f_1 t - \phi_1) + a \cos (2\pi f_2 t - \phi_2). \end{aligned}$$

On computing the quantities defined in §4(d) one finds

$$\begin{aligned} \rho_{NN}(\tau) &= \rho_{SS}(\tau) = a^2 \cos 2\pi f_1 \tau + a^2 \cos 2\pi f_2 \tau, \\ \rho_{SN}(\tau) &= a^2 \cos \phi_1 \cos 2\pi f_1 \tau + a^2 \cos \phi_2 \cos 2\pi f_2 \tau. \end{aligned}$$

If now we ignore the slight difference between f_1 and f_2 , writing each as f , we get

$$\begin{aligned} C_{SS} &= C_{NN} = 2a^2, \\ C_{SN} &= a^2(\cos \phi_1 + \cos \phi_2), \quad Q_{SN} = a^2(\sin \phi_1 + \sin \phi_2), \end{aligned}$$

and in particular $R = \cos \frac{1}{2}(\phi_1 - \phi_2)$, $\phi = \frac{1}{2}(\phi_1 + \phi_2)$.

† There is a close analogy with the problem of aliasing (§4(b)) when the frequency exceeds half the sampling frequency.

Because ϕ is the mean of the actual phase differences ϕ_1 and ϕ_2 , the direction α that one would deduce from ϕ lies between the true directions α_1 and α_2 . But because R is less than unity, one can infer that the waves do not come as a pencil beam from any single direction. In fact if R is near to unity, one can write the angular spread as

$$\Delta\alpha = \alpha_1 - \alpha_2 = (1 - R^2)^{\frac{1}{2}} / (\pi k D \cos \alpha),$$

$$\sin \alpha = \phi / (2\pi k D).$$

For peak A, we find $R^2 \approx 0.5$, $\phi = 30^\circ$, $2\pi k D = 2.2$; hence $\alpha = 14^\circ$ and $\Delta\alpha = \sim 40^\circ$. For peak B the coherence is lower, but the wavelength shorter. We find $R^2 = 0.4$, $\phi = -120^\circ$, $\alpha = -37^\circ$, $\Delta\alpha = 32^\circ$.

The interpretation of beam widening from a single pair of instruments is rather hazardous. Loss of coherence can be due to many different circumstances: instrumental noise, faulty recording, clock errors, and lack of stationarity (such as the variation in depth during a tidal cycle). In this sense the beam width inferred here must be regarded as an upper limit. In any case a rather better understanding of the wave system is reached by considering all three instruments.

(e) *Dispersion*

Comparison of the spectra of three successive days shows a progressive shift of the peaks toward high frequencies (figure 5). The frequency of peak A increases by 5 c/ks in a day; peak B increases by 8 c/ks per day. This progressive increase in frequency is characteristic of all records. On figure 17 peaks A and B appear as slanting ridges on a contour chart of spectral density as a function of frequency and time. The two ridges slant at different angles and intersect on 30 October. The ridges are found to be remarkably straight, so that df/dt is nearly constant for any one ridge.

The ridges can be accounted for in terms of classical wave theory. Let x be the distance from a source to a recorder, t_0 , the time of generation, and t , the time of recording. The source is assumed a point in space-time. This implies that linear dimensions are small compared to travel distances, and duration small compared to travel time.

The group velocity, $V(f)$, is the speed with which some frequency f , is propagated from source to receiver:

$$V(f) = x / (t - t_0). \quad (5.4)$$

In deep water $V(f) = g / 4\pi f$. (5.5)

It follows that $f = g(t - t_0) / 4\pi x$, (5.6)

so that on a plot of f against t a single event lies along a straight line with slope

$$df/dt = g / 4\pi x.$$

The intercepts with $f = 0$ occurs at $t = t_0$. Each of the ridge lines can then be immediately associated with a source of known time and distance. For peaks A and B the results are:

A: $t_0 = 2300$ P.D.T. on 22 October, $\Delta = 59^\circ$, $\theta = 245^\circ$ T,

B: $t_0 = 1200$ P.D.T. on 18 October, $\Delta = 96^\circ$, $\theta = 195^\circ$ T.

Here Δ is the distance expressed in terms of the angle subtended at the earth's centre between source and receiver. The directions and widths of the sources have previously been estimated. Evidently the two storms are located in widely different areas of the Pacific Ocean.

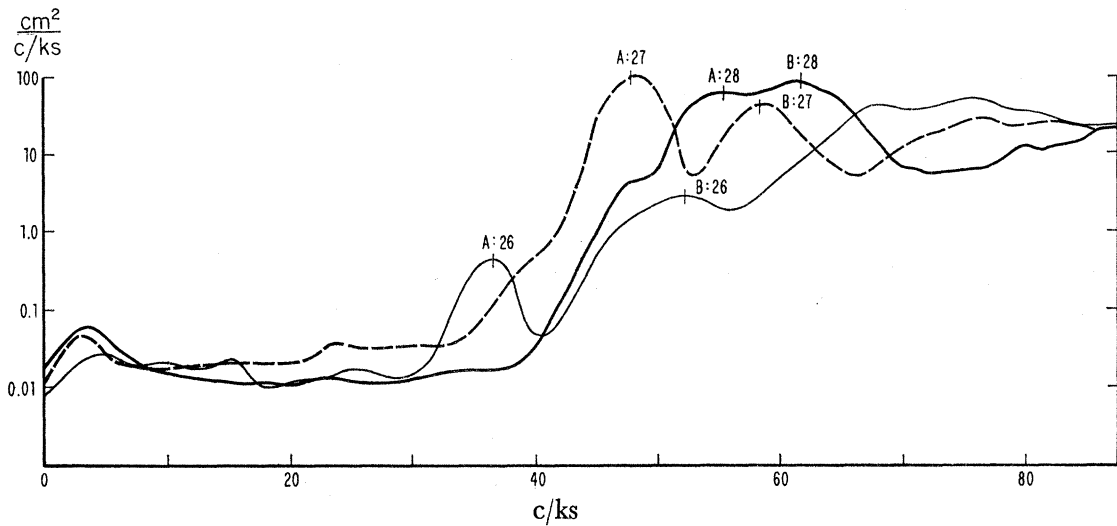


FIGURE 5. Spectra of recordings on 26, 27 and 28 October show two peaks (marked A and B). Both peaks progress toward higher frequency; peak A varies more rapidly as it is associated with a closer storm. Compare to spectral contour diagram, figure 16.

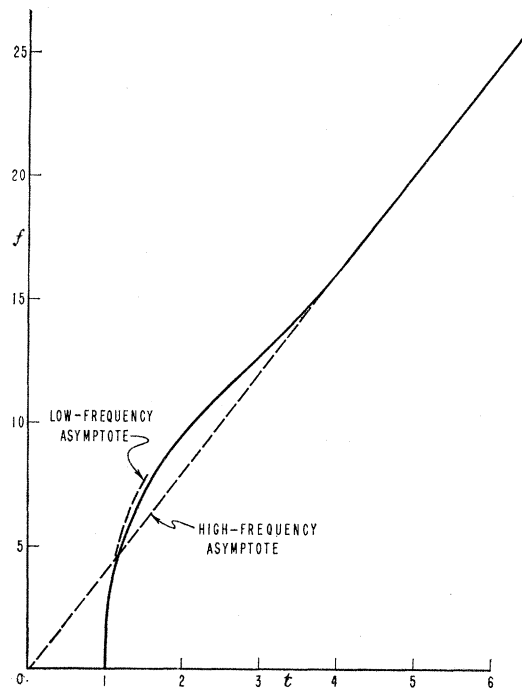


FIGURE 6. The derived relation $f(t)$ for a source at a distance $\Delta = 110^\circ$. The ocean depth is taken as $h = 4$ km. Unit time refers to Δ/\sqrt{gh} . f in c/ks.

(f) *Effect of finite depth on ridge lines*

To allow for the effect of the finite depth of the oceans (5.5) is replaced by

$$V(f) = \frac{1}{2}V_0 \left(1 + \frac{2\mu}{2\sin\mu} \right) \left(\frac{\tanh\mu}{\mu} \right)^{\frac{1}{2}},$$

where $V_0 = \sqrt{gh}$ is the asymptotic value for the group velocity as $f \rightarrow 0$, and where

$$\mu = 2\pi kh = (2\pi h/C)f.$$

For very low frequencies $V = V_0(1 - \frac{1}{2}\mu^2)$, $\mu = 2\pi\sqrt{(h/g)}f$.

It follows that
$$t - t_0 = \frac{x}{V_0} \left[1 + \frac{4\pi^2 h}{g} f^2 \right],$$

where x/V_0 is the time of the earliest arrival. At high frequencies the solution approaches

$$t - t_0 = 4\pi x f / g,$$

as previously. The general relation $f(t)$ is shown in figure 6 for the case $h = 4$ km, $\Delta = 110^\circ$. The ridge does not deviate appreciably from a straight line for frequencies above 15 c/ks.

6. GENERAL THEORY OF ARRAYS

(a) Elementary wave trains

Consider a wave whose measurable value of η varies with the space co-ordinates x , y and the time co-ordinate t according to

$$\eta = a \exp i 2\pi(lx + my + ft + \alpha). \quad (6.1)$$

This does not of course represent a real sea wave since the values of η are complex, but it will be apparent that a wave with real values can be created by adding two complex waves that differ only in the sign of i . A positive sign has been used before ft for the sake of symmetry. It implies that a wave whose 'space frequencies' l , m and 'time frequency' f are all positive is one that approaches the space origin from the positive region of x and y . For a locus of constant phase, a 'wavecrest', is a line

$$lx + my + ft + \alpha = \text{constant},$$

and its points of intersection with the x and y axes move with velocities $-f/l$, $-f/m$.

Wave analysis will be concerned with finding the coefficients in (6.1), in particular l and m . When l and m have been found for a wave train such as that sketched in figure 7 (a), one may use them as rectangular coordinates to plot a point P as shown in figure 7 (b). The bearing of P from the l - m origin is the same as the direction from which the wave is approaching the site. The distance of P from the origin measures the wave number (the reciprocal of wave length). One may record the wave 'power' a^2 at point P . Many wave trains can be summarized by a diagram such as figure 7 (b). The wave number k and the direction θ are the polar coordinates corresponding to

$$l = k \cos \theta, \quad m = k \sin \theta.$$

So figure 7 (b) is sometimes called a plot in 'wave-number space', and l and m are 'components of wave number'.

The coefficients l and m are the rates of change of phase (in cycles) with the space co-ordinates x and y , just as f is the rate of change of phase with time t . They may be found by observing how the phase depends on x , y , and t . In the complex wave of (6.1), the phase of the wave is the argument (in cycles) of the wave value η . If one knows wave values at two places and instants, say (x, y, t) and $(x+X, y+Y, t+T)$ then the amount by which the phase of the wave at the second point exceeds that at the first is the argument of the conjugate product

$$\eta^*(x, y, t) \eta(x+X, y+Y, t+T) = a^2 \exp i 2\pi(lX + mY + fT). \quad (6.3)$$

The argument varies linearly with the interval X , Y , and T . The modulus of the product is instructive in the sense that it is a^2 , the squared modulus of the wave amplitude. Since in real waves this is related to wave energy, a^2 is called the wave 'power'.

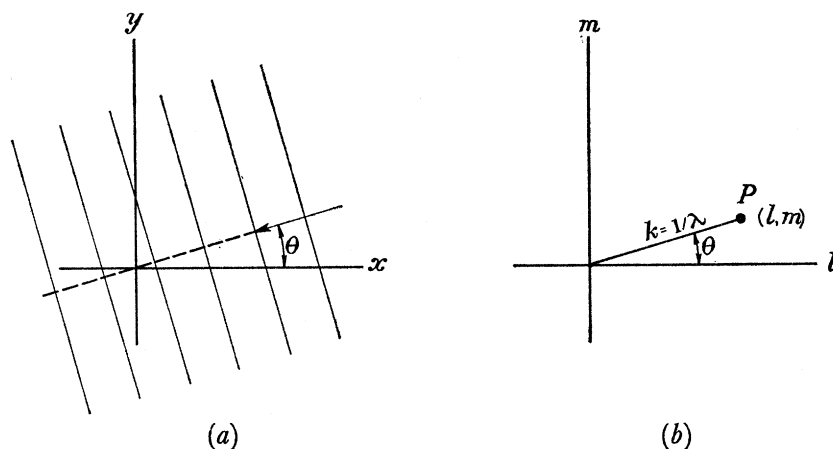


FIGURE 7. A wave train in real space (a) and its representation in wave-number space (b).

(b) *The spectrum*

In a more complicated wave system comprising many complex wave trains whose l , m , or f values are different one has

$$\eta = \sum_1^{n=\infty} a_n \exp i 2\pi(l_n x + m_n y + f_n t + \alpha_n). \quad (6.4)$$

A conjugate product formed in the manner of expression (6.3) is not now independent of the actual coordinates x , y , and t that were chosen; but if one averages the product over wide ranges in x , y , and t but keeping the intervals X , Y , and T constant, it becomes

$$\overline{\eta^*(x, y, t) \eta(x+X, y+Y, t+T)} = \sum_1^{n=\infty} a_n^2 \exp i 2\pi(l_n X + m_n Y + f_n T).$$

It is a function of the intervals X , Y , and T and may be called $\rho(X, Y, T)$, the 'correlogram' of the wave. Its argument is in some sense a weighted average of the phase differences that the different waves produce. The right-hand side can be written differently if one supposes that there are very many waves in any small range of l , m , and f and that the sum of the powers a_n^2 of these waves in any small range is proportional to the size of the range according to a power density $E(l, m, f)$. Then

$$\rho(X, Y, T) = \iiint_{-\infty}^{\infty} E(l, m, f) \exp i 2\pi(lX + mY + fT) dl dm df, \quad (6.5)$$

where $E(l, m, f)$ is the power spectrum. Thus the power spectrum $E(l, m, f)$ is the Fourier transform of the correlogram (X, Y, T) each being in three dimensions.

When the wave signals η are all real, one must suppose that every wave train such as equation (6.1) presumes the presence of another,

$$a \exp i 2\pi(-lx - my - ft - \alpha), \quad (6.6)$$

so that together they create a purely real sinusoid with amplitude $2a$. These complex wave trains each have the same squared modulus. With real waves therefore, equal power density

occurs at every pair of values (l, m, f) and $(-l, -m, -f)$. This symmetry in $E(l, m, f)$ causes the general relation (6.5) to become

$$\rho(X, Y, T) = \iiint_{-\infty}^{\infty} E(l, m, f) \cos 2\pi(lX + mY + fT) \, dl \, dm \, df. \quad (6.7)$$

It is usual to suppose that the wave systems under study have 'stationary' properties so that the correlations ρ need only be established by averages over one of the variables x, y , and t instead of all three. This means in practice that one can use an array of detectors that does not extend over a great area of sea but is maintained for a long time so that correlations can be obtained by a time average. Then one has a finite number of instruments, say M , giving as signals the various time series of real values,

$$\eta_r(t) \quad (r = 1 \dots M),$$

and if the displacement of the s th instrument from the r th is written X_{rs}, Y_{rs} , the 'cross-correlogram' of the two signals, the lag being T , is the time-averaged product,

$$\overline{\eta_r(t) \eta_s(t+T)} = \rho(X_{rs}, Y_{rs}, T). \quad (6.8)$$

This is a track of values through the three-dimensional continuum $\rho(X, Y, T)$, the track being a line parallel to the T -axis through X_{rs}, Y_{rs} . It will be seen that the 'cross-correlogram' can also be written

$$\overline{\eta_r(t) \eta_s(t+T)} = \overline{\eta_s(t) \eta_r(t-T)} = \rho(-X_{rs}, -Y_{rs}, -T),$$

and so it also represents a track in the direction $-T$ through the point $-X_{rs} - Y_{rs}$. Each of the 'cross-correlograms' of the different pairs of instruments, therefore, provides values of ρ along two tracks in the continuum. Each 'auto-correlogram' represents the track $\rho(0, 0, T)$. The assembly of the 'correlograms' shows all that is known about the three-dimensional distribution $\rho(X, Y, T)$.

The first step in using (6.7) is to make a transformation in T . This is straightforward because the correlation data are continuous in T . Equation (6.7) can be written as

$$\begin{aligned} \rho(X, Y, T) = & \int_{-\infty}^{\infty} \cos 2\pi f T \, df \int_{-\infty}^{\infty} \int_{-\infty}^{\infty} E(l, m, f) \cos 2\pi(lX + mY) \, dl \, dm \\ & - \int_{-\infty}^{\infty} \sin 2\pi f T \, df \int_{-\infty}^{\infty} \int_{-\infty}^{\infty} E(l, m, f) \sin 2\pi(lX + mY) \, dl \, dm. \end{aligned}$$

This shows that if one knows the values of ρ as a function of T for any assigned XY and if one calculates its cosine transform, say $C(X, Y, f)$, then $C(X, Y, f)$ must be the function

$$C(X, Y, f) = \int_{-\infty}^{\infty} \int_{-\infty}^{\infty} E(l, m, f) \cos 2\pi(lX + mY) \, dl \, dm. \quad (6.9)$$

Similarly the sine transform, say $Q(X, Y, f)$ is the function

$$Q(X, Y, f) = - \int_{-\infty}^{\infty} \int_{-\infty}^{\infty} E(l, m, f) \sin 2\pi(lX + mY) \, dl \, dm. \quad (6.10)$$

For purposes of discussion one can combine these two into the relation

$$C(X, Y, f) - iQ(X, Y, f) = \int_{-\infty}^{\infty} \int_{-\infty}^{\infty} E(l, m, f) \exp i 2\pi(lX + mY) \, dl \, dm. \quad (6.11)$$

At any prescribed frequency f_0 , $C - iQ$ can therefore be thought of as a space correlogram with complex values, whose transform is the 'directional spectrum' $E(l, m, f_0)$ for that frequency. The functions C and Q are precisely those computed from the recordings (§4(d)).

7. INTERPRETATION OF THE CROSS-SPECTRAL MATRIX

The next step in the analysis is to deduce the directional spectrum $E(l, m, f)$ from the observed values, $C(X, Y, f)$ and $Q(X, Y, f)$. The inverse of (6.11) is

$$E(l, m, f) = \int_{-\infty}^{\infty} \int_{-\infty}^{\infty} [C(X, Y, f) - iQ(X, Y, f)] \exp[-i2\pi(lX + mY)] dX dY, \quad (7.1)$$

and it would be a straightforward matter to calculate $E(l, m, f)$ if one knew the C 's and Q 's as continuous functions of X and Y . Unfortunately one knows the C 's and Q 's only at discrete values of X and Y , namely those intervals between the various instruments taken in pairs. The present section discusses ways of evading this practical limitation.

The interval distances will now be written more briefly as

$$(X_n, Y_n) \text{ and } (-X_n, -Y_n) \quad (n = 1 \dots N)$$

and the corresponding C 's and Q 's as C_n, Q_n . If there are M instruments the number N is of course $\frac{1}{2}M(M-1)$.

(a) Conventional treatment

One conventional but unconvincing assumption would treat all the unknown values of $C - iQ$ as zero and weight the known values by delta functions of arbitrary weights b_n . With this treatment, the true power distribution $E(l, m, f)$ in 7.1 becomes an approximate distribution $E'(l, m, f)$

$$E'(l, m, f) = b_0 C_0 + 2 \sum_1^{n=N} b_n C_n \cos 2\pi(lX_n + mY_n) - 2 \sum_1^{n=N} b_n Q_n \sin 2\pi(lX_n + mY_n).$$

Thus, the spectrum is pictured as the sum of N sinusoids plus a constant. In the present experiments there are only three instruments ($M = 3$) and consequently only three instrument pairs ($N = 3$) so the spectrum is made up of only three sinusoids. One is at liberty to choose the weights b_n in any way that seems best. There is some advantage in choosing them each to be $\frac{1}{7}$. If, for example, the C 's and Q 's are in fact due to only a single well-directed swell of power A_0 and wave numbers l_0, m_0 , then from (6.9) and (6.10):

$$\left. \begin{aligned} C_0 &= A_0, \\ C_n &= A_0 \cos 2\pi(l_0 X_n + m_0 Y_n), \\ Q_n &= -A_0 \sin 2\pi(l_0 X_n + m_0 Y_n). \end{aligned} \right\} \quad (7.2)$$

The calculated distribution E' is then (b_n being $\frac{1}{7}$)

$$E'(l, m, f) = \frac{1}{7} \left[C_0 + 2 \sum_1^{n=3} C_n \cos 2\pi(lX_n + mY_n) - 2 \sum_1^{n=3} Q_n \sin 2\pi(lX_n + mY_n) \right]. \quad (7.3)$$

For the stated values of the C 's and Q 's this reduces to

$$E'(l, m, f) = A_0 \frac{1}{7} \left\{ 1 + 2 \sum_1^{n=3} \cos 2\pi[X_n(l - l_0) + Y_n(m - m_0)] \right\}. \quad (7.4)$$

The maximum value of this occurs at l_0, m_0 and is numerically equal to A_0 , the actual power of the swell. The choice of the b 's as $\frac{1}{7}$ has brought this about. But this does not prevent the spectrum E' from extending repetitively to indefinitely large wave numbers. This unconvincing result arises from the unconvincing assumption made at the start.

(b) *A best-fitting single wave train*

For local geophysical reasons one may expect to receive mainly well-directed swells from distant storms. A reasonable treatment would be to fit the measured C 's and Q 's as well as possible in a least-square error sense by one or more such wave trains. Now a single wave train of power A_0 , wave numbers, l_0, m_0 , would give the C 's and Q 's listed in (7.2), and these imply perfect coherence, which is never observed experimentally. But one may note that the sum of the squares of the differences between the observed C 's and Q 's and those expected for a single wave train is

$$\begin{aligned} H &= (C_0 - A_0)^2 + 2 \sum_1^{n=3} [C_n - A_0 \cos 2\pi(l_0 X_n + m_0 Y_n)]^2 + 2 \sum_1^{n=3} [Q_n + A_0 \sin 2\pi(l_0 X_n + m_0 Y_n)]^2 \\ &= C_0^2 + 2 \sum_1^{n=3} (C_n^2 + Q_n^2) + 7A_0^2 \\ &\quad - 2A_0 \left[C_0 + 2 \sum_1^{n=3} C_n \cos 2\pi(l_0 X_n + m_0 Y_n) - 2 \sum_1^{n=3} Q_n \sin 2\pi(l_0 X_n + m_0 Y_n) \right]. \end{aligned}$$

We may choose A_0, l_0 and m_0 so as to minimize this squared error. The quantity in square brackets is merely seven times $E'(l_0, m_0, f_0)$, the power density that would be predicted from the observed C 's and Q 's for wave numbers l_0, m_0 by the conventional treatment of (7.3). The choice of A_0 that minimizes H is seen to be

$$A_0 = E'(l_0, m_0, f_0). \quad (7.5)$$

Then
$$H = C_0^2 + 2 \sum_1^{n=3} (C_n^2 + Q_n^2) - 7 [E'(l_0, m_0, f_0)]^2. \quad (7.6)$$

The choice of l_0, m_0 that minimizes H and so represents a 'best fitting' wave train is merely that which makes $[E'(l_0, m_0, f_0)]^2$ as great as possible.

So the conventional treatment is useful after all. The indicated procedure is as follows: Compute $E'(l, m, f)$ according to (7.3), using the observed seven quantities C_n, Q_n and using trial values for l, m . The particular values, l_0, m_0 , for which $[E'(l, m, f)]^2$ is greatest define the best fitting single wave train in the least-square sense; and the corresponding value $E'(l_0, m_0, f)$ is the power of the wave train. In making this choice one, of course, ignores any l, m values for which E' proves to be negative.

An example is shown in figure 8. Writing $l = k \sin \alpha, m = k \cos \alpha$, we have chosen various values of k in the vicinity of the theoretical value of k at the frequency under consideration. For each trial value of k we computed $H(k, \alpha)$ for various α , and determined its minimum value, $H_{\min.}(k)$, corresponding to $\alpha = \alpha_0$. The curve $H_{\min.}(k)$ has a minimum at some value $k = k_0$. In the example shown the value of k_0 does not differ measurably from k_{theory} . Furthermore, values of α_0 remained unchanged throughout the interval here under consideration. This is essentially the result of many other such determinations; k remains close to k_{theory} throughout the frequencies of the sea and swell. At the very low frequencies the

determination becomes unstable. Thus we have determined k_0 and α_0 (or alternatively l_0, m_0) without recourse to wave theory. However, in the routine computations we considered k_0 as a known function of f , and this reduced the number of unknowns by one (§7(d)).

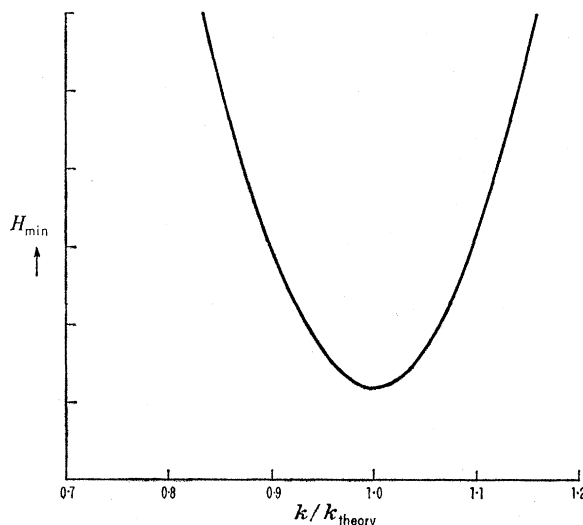


FIGURE 8. Empirical determination of wave number. The example pertains to 29 October for a frequency band centred on 46 c/ks.

Perhaps the most rapid means of determining l_0 and m_0 is as follows. The distribution of $E'(l, m, f)$ is merely the sum of three sinusoids in l, m space and can in fact be written

$$E'(l, m, f) = \frac{1}{7} \left[C_0 + 2 \sum_1^{n=3} T_n \cos \alpha_n \right],$$

where

$$T_n \cos \psi_n = C_n, \quad T_n \sin \psi_n = Q_n, \\ \alpha_n = \psi_n + 2\pi(lX_n + mY_n).$$

The problem now is to find what set of angles α_1, α_2 and α_3 maximize E' ; the values l_0, m_0 that provide these angles can be calculated afterwards.

It should be noted that since the separations X_n and Y_n are taken in cyclic order round the triangle of detectors then

$$\sum_1^{n=3} X_n = \sum_1^{n=3} Y_n = 0$$

so that the sum of the three angles α is a known constant

$$\sum_1^{n=3} \alpha_n = \sum_1^{n=3} \psi_n.$$

Begin therefore by noting the two greatest amplitudes, say T_1 and T_2 , and supposing that α_1 and α_2 are zero. Evaluate E' knowing that α_3 is $\sum_1^{n=3} \psi_n$. Then try in turn values of α_1 and α_2 that are not zero, knowing that α_3 must be

$$\alpha_3 = \sum_1^{n=3} \psi_n - \alpha_1 - \alpha_2.$$

Values that produce an increased E' are adopted. This 'hunting' process rapidly establishes the values of α_1 and α_2 that maximize E' and from them one calculates l_0, m_0 .

Of course the set of values α_1 , α_2 and α_3 is not unique. Any of them may be varied by some integral multiple of 2π . This leads to an infinite set of points l_0 , m_0 . To choose between them one needs other geophysical information, usually a dispersion formula that suggests what the wave number

$$k_0 = (l_0^2 + m_0^2)^{\frac{1}{2}}$$

is likely to be at the frequency that is being considered.

It is of interest to note that if one applies the least-square error method to only a single pair of instruments, the expression for E' contains only a single sinusoid in l , m ; and the values of l_0 , m_0 that give the best fit have loci that are just the 'crest' lines of this sinusoid in l , m space. If one uses wave number, k_0 , and direction, α_0 , instead of l_0 and m_0 , the relation between k_0 and α_0 is precisely that obtained previously in (5.3).

(c) *A best-fitting pair of wave trains*

The information given by the seven C and Q values is more than enough to determine a single wave train for this has only three unknown characters, A_0 , l_0 , and m_0 . Indeed one should be able to fit two wave trains, determining six unknown characters. Methods of doing this were devised but were not much used in the present experiments. These methods will be outlined, however, since they may be of use in other work.

(1) If one chooses any two points, say (l_1, m_1) and (l_2, m_2) in wave-number space, then the best amplitudes to choose for these waves are A_1 and A_2 , that fulfil the relations

$$E'_1 = A_1 + F_{12}A_2, \quad E'_2 = A_2 + F_{21}A_1.$$

Here E'_1 and E'_2 are the values calculated for wave numbers (l_1, m_1) and (l_2, m_2) by the conventional method from the observed C 's and Q 's. The factor F_{12} is the E' that would be calculated for wave numbers (l_1, m_1) using C 's and Q 's that would arise from a single wave train of unit power having wave numbers (l_2, m_2) .

The best fit to the observed C 's and Q 's is obtained when one chooses (l_1, m_1) and (l_2, m_2) so as to maximize

$$A_1 E'_1 + A_2 E'_2.$$

These results readily follow by arguments like those used in §(b), for deciding the best fit for a single wave train.

(2) If the wave data arise solely from two well-directed wave trains, then the C 's and Q 's will be found to obey the relation

$$T_0(T_0^2 - T_1^2 - T_2^2 - T_3^2) + 2T_1T_2T_3 \cos(\psi_1 + \psi_2 + \psi_3) = 0 \quad (7.7)$$

where T and ψ are defined by $T_n \exp i\psi_n = C_n - iQ_n$.

One may write A for the power of the first wave train and $\alpha_1, \alpha_2, \alpha_3$ for the phase differences it alone would display at the three pairs of instruments. Similarly $B, \beta_1, \beta_2, \beta_3$ may represent the power and the phase differences of the second wave train. Then it must follow that the observed C 's and Q 's when both waves are present are merely the sums of what would be observed with each wave alone, or

$$\begin{aligned} T_0 &= A + B, \\ T_1 \exp i\psi_1 &= A \exp i\psi_1 + B \exp i\psi_1, \\ T_2 \exp i\psi_2 &= A \exp i\psi_2 + B \exp i\psi_2, \\ T_3 \exp i\psi_3 &= A \exp i\psi_3 + B \exp i\psi_3. \end{aligned}$$

It should be noted that for any single wave train the phases have a zero total, or

$$\alpha_1 + \alpha_2 + \alpha_3 = 0 = \beta_1 + \beta_2 + \beta_3.$$

Then A , B , α_2 , and β_2 can be eliminated from these equations (and their conjugates) to show that $\exp i\alpha_1$ and $\exp i\beta_1$ are the two roots of the equation

$$T_0 T_1 \exp i\psi_1 - T_2 T_3 \exp -i(\psi_2 + \psi_3) - Z(T_0^2 + T_1^2 - T_2^2 - T_3^2) \\ + Z^2[T_0 T_1 \exp -i\psi_1 - T_2 T_3 \exp i(\psi_2 + \psi_3)] = 0.$$

Analogous equations give α_2 and β_2 , α_3 , β_3 .

Rather than solve the equations numerically it is perhaps easier to make a graphical construction. If one plots in an Argand diagram the points

$$(T_1/T_0) \exp i\psi_1 \quad \text{and} \quad (T_2 T_3/T_0^2) \exp \{-i(\psi_2 + \psi_3)\},$$

then a chord through the first point perpendicular to the line joining the two points cuts the unit circle at the points $\exp i\alpha_1$ and $\exp i\beta_1$. Thus α_1 and β_1 are found. Also the first point divides the chord in the ratio A/B , while the sum of A and B is of course T_0 . Analogous constructions give α_2 and β_2 , α_3 and β_3 . When these phase angles are known, it is a straightforward matter to determine the l_1 , m_1 values.

One cannot expect that any set of data will exactly satisfy (7.7). One may choose to use $(1 - \epsilon) T_0$ instead of T_0 in the whole analysis, arguing that some instrumental noise may have contributed to the spectral value T_0 but not, of course, to the cross-spectra. This is an acceptable method if the value of ϵ satisfying (7.7) is small and positive, but it does not have the virtue of fitting the two sources to the experimental data by least-square error.

(d) *Experimental test of the dispersion law*

For waves in water of depth h , theory predicts that the wave number and frequency should be related by the classical dispersion relation

$$2\pi f^2 = gk \tanh(2\pi kh). \quad (7.8)$$

So far this relation has not entered the analysis.

If the relation were not exactly known one might determine it experimentally. At each frequency one would find a best-fitting wave train by the method described in §7 (b), and if the fit proved good, one would calculate k_0 from

$$k_0^2 = l_0^2 + m_0^2.$$

This would give an empirical dispersion relation $k_0(f)$. Of course there are many alternative values for l_0 , m_0 , and some approximate prior knowledge of the dispersion relation is necessary.

A number of swell recordings were treated in this way. It was consistently found that when the single wave train gave a good fit, the calculated wave number k_0 agreed closely with that predicted by the theoretical formula (7.8). Figure 8 illustrates such a case. Various trial wave numbers were used for the single wave train and in each case a direction α was chosen that minimized the squared error H . The curve shows how these minimum errors vary with the assigned wave number k . The least error occurs at a wave number very close to that predicted by theory. It seems therefore that the theoretical law in (7.8) is closely obeyed by actual swell.

In other geophysical problems one may have no clear theoretical formula for dispersion. In the case of microseisms for example the dispersion depends on the details of the subsurface structure and not even the precise form of the relation can be considered as given. In such problems the array theory provides a powerful tool for deriving the dispersion relation by empirical methods.

The bulk of the swell data were analysed on the assumption that wave trains have the wave number $k(f)$ that theory would predict. Then with $k(f)$ known, the best-fitting single wave train is characterized by only two unknown parameters: the power, A_0 , and the direction, θ_0 . The procedure is to substitute $l(f) = k(f) \cos \theta$, $m(f) = k(f) \sin \theta$ in (7.3) and to determine by trial the particular value of θ (θ_0 , say) for which $E'(\theta, f)$ has a maximum value. Then θ_0 is the direction of approach of the wave train, and $E'(\theta_0, f) = A_0$ is its power.

All determinations of A_0 and θ_0 were made with the high-speed computer. First $\partial E'(\theta, f) / \partial \theta$ was evaluated at 5° intervals, and the roots determined by linear interpolation. In the case of multiple maxima, the highest maximum was chosen.

In order to test the 'goodness of fit' of the point-source model to the data, two criteria were used. The first compares $H(A_0, \theta_0)$, the minimum value H , to the value \tilde{H} that would have been obtained if the energy were equally distributed in all directions:

$$\mathcal{H}_1 = 1 - H(A_0, \theta_0) / \tilde{H}. \quad (7.9)$$

The second criterion compares the power A_0 of the single wave train to the total observed energy, C_0 :

$$\mathcal{H}_2 = (A_0 - \tilde{A}) / (C_0 - \tilde{A}). \quad (7.10)$$

Here again \tilde{A} refers to an isotropic radiation.

Both \mathcal{H}_1 and \mathcal{H}_2 are numbers between 0 and 1, the lower limit corresponding to isotropic radiation and the upper limit to a point source. At the spectral peaks both criteria are generally above 0.5; between spectral peaks the criteria are very low, as expected.

It is not certain that this method of fitting a single wave train is any speedier than the general method of §7(b) but once the dispersion law has been established, this method is the correct one to use for the iteration process described in the next section, 7(e).

(e) Analysis by iteration

The consistent results obtained under favourable circumstances by fitting a single wave train to the data suggests the search for the pair of wave trains that fit the data best and ultimately for an iterative scheme. The power distribution $E(\theta, f)$ is subject to the restraint that it must everywhere be positive. An obvious scheme is to proceed as follows: (i) Calculate A_0 and θ_0 from the observed C_n and Q_n according to the method described in the preceding section; (ii) Compute the matrix components

$$\left. \begin{aligned} C'_0 &= A_0, \\ C'_n &= A_0 \cos 2\pi(l_0 X_n + m_0 Y_n), \\ Q'_n &= -A_0 \sin 2\pi(l_0 X_n + m_0 Y_n), \end{aligned} \right\} \quad (7.11)$$

that would be produced by this wave train, where

$$l_0 = k_0(f) \cos \theta_0, \quad m_0 = k_0(f) \sin \theta_0.$$

(iii) Form the residual matrix $C_n - C'_n$, $Q_n - Q'_n$; this presumably would have been the observed spectral matrix if the most energetic source had been absent. (iv) Calculate the optimum point source for the residual matrix, etc. The procedure is followed independently for each frequency band.

The difficulty with this scheme is that the first computed wave train tends to include some of the energy that actually comes from somewhat different directions so that the subtracted matrix C'_n , Q'_n is rather too large. As a result it often happens that the residual matrix is fitted best by a wave train coming from a direction 180° different from that of the first train.

Clearly one wants to subtract at each step only a fraction of the initial wave train. We chose the fraction 0.1, and continued for 100 iterations, or until the residual matrix vanished, whichever came first. In a typical computation the first 10 or 20 iterations gave directions clustered within a 5° band, followed by the first indication of the direction of the secondary source.† In subsequent iterations the directions would jump back and forth between the two directions.

The method was tested in various artificial examples, some of which are displayed in figure 9. A power distribution was assumed; the corresponding C 's and Q 's were calculated and these were then analyzed by the iteration process. The diagrams compare the true power distribution, shown by a thin curve or by thin ordinates, with the power distribution suggested by the iteration process which is displayed as a histogram. The two do not agree in detail although the power distribution in the histogram always satisfies the calculated C and Q values very closely. With the continuous distributions shown on the left, the histogram emphasizes the peak and indicates the over-all spread. When power comes from two well-defined directions as in the centre diagrams, or from three as in the diagrams on the right, these are not resolved in the histogram unless the directions are well separated.

The iterative analyses were made for all October observations. Figures 10, 11 and 12 show the results for the same three days that have previously been used for illustration (figures 2, 3, 4, 5). The most interesting case is that of 27 October. The low-frequency peak (peak A) is associated with a western source. Peak B is associated with a southern source, as previously inferred. The transition at 53 c/ks is remarkably sharp. The directional distribution at the transition clearly show the superposition of the two wave trains. Outside the transition zone, the variation with frequency is smooth, and on comparison it is found to be in quite satisfactory agreement with the directions inferred from the south-north pair of instruments only. At very low frequencies the measured direction swings normal to shore as the result of refraction (§9).

On the preceding day the transition zones are not as nicely developed. Peak A is confined to the lower frequencies, and the southern swell (peak B) predominates over most of the range. At frequencies above those of peak B there is evidence of further radiation from the west. On 28 October the western swell associated with peak A now dominates the entire frequency band except at the very lowest frequencies, where a new southern source makes itself felt. The direction of peak A tends northward with increasing frequency, probably as a result of a southward movement of the storm (§14).

† At this stage of the computation the program was altered to save computing time. We now consider this variation in the computing scheme to have been undesirable. The details are rather cumbersome and will be omitted inasmuch as they do not affect the results appreciably.

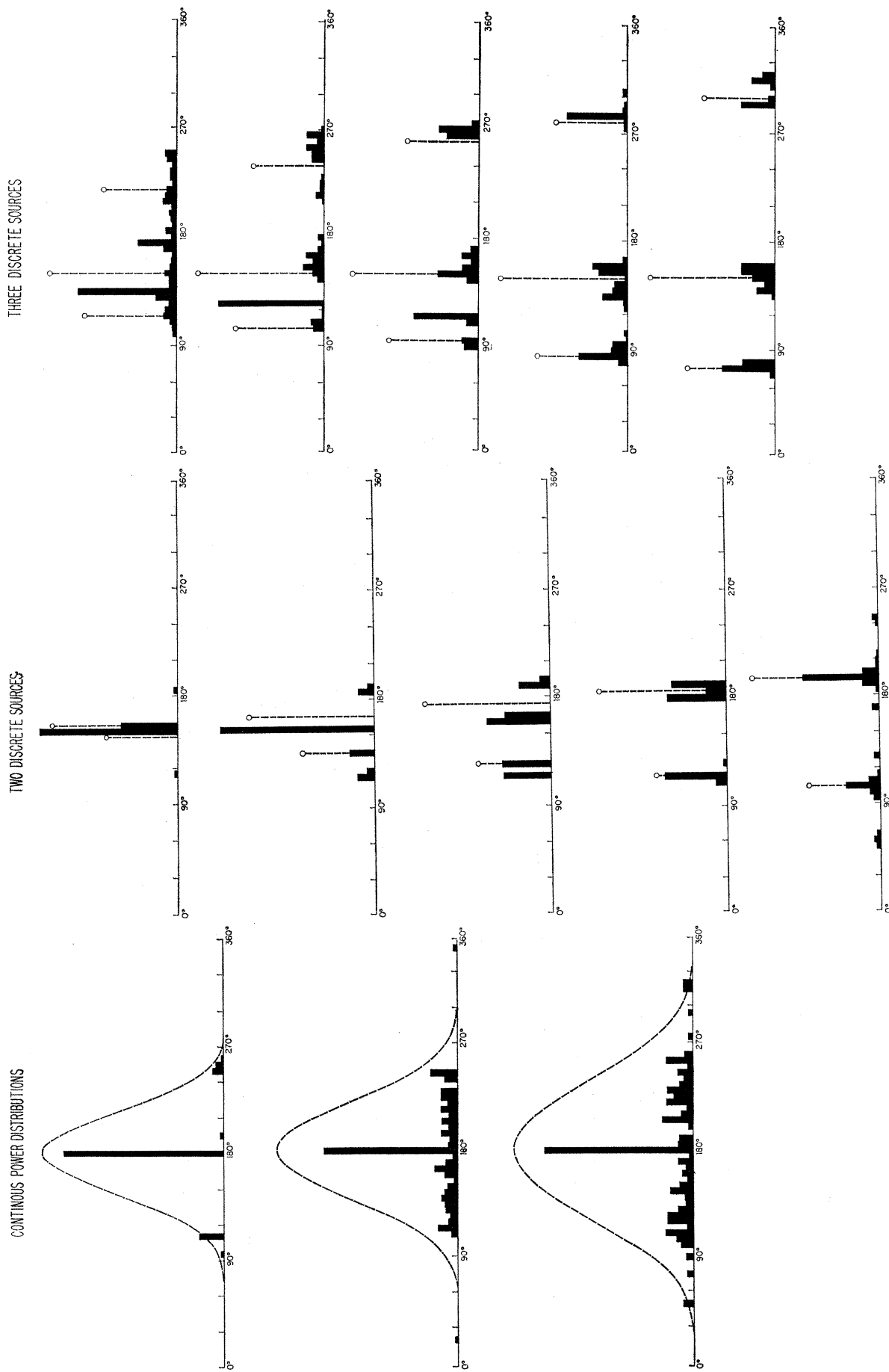


FIGURE 9. Some artificial examples of the iteration method of analysis. The histograms show the distribution of power as found by the iteration method. In the three examples on the left the true distribution of power is continuous as shown by the thin curves. In the five examples in the middle, the power actually came from two directions only, as shown by the thin ordinates. In the five examples on the right, the power came from three directions. The histogram length is taken as 2.1 times the side of the triangle. The histograms give some indication of these true distributions of power.

The performance of the iterative method can be judged in two ways: from the continuity in the results between adjoining frequency bands, and from the degree to which the cross-spectral matrix has been made to vanish at the end of the procedure. The performance is erratic. The method often fails above 60 c/ks. As might be expected, the convergence is best when most of the energy is within a single narrow band.

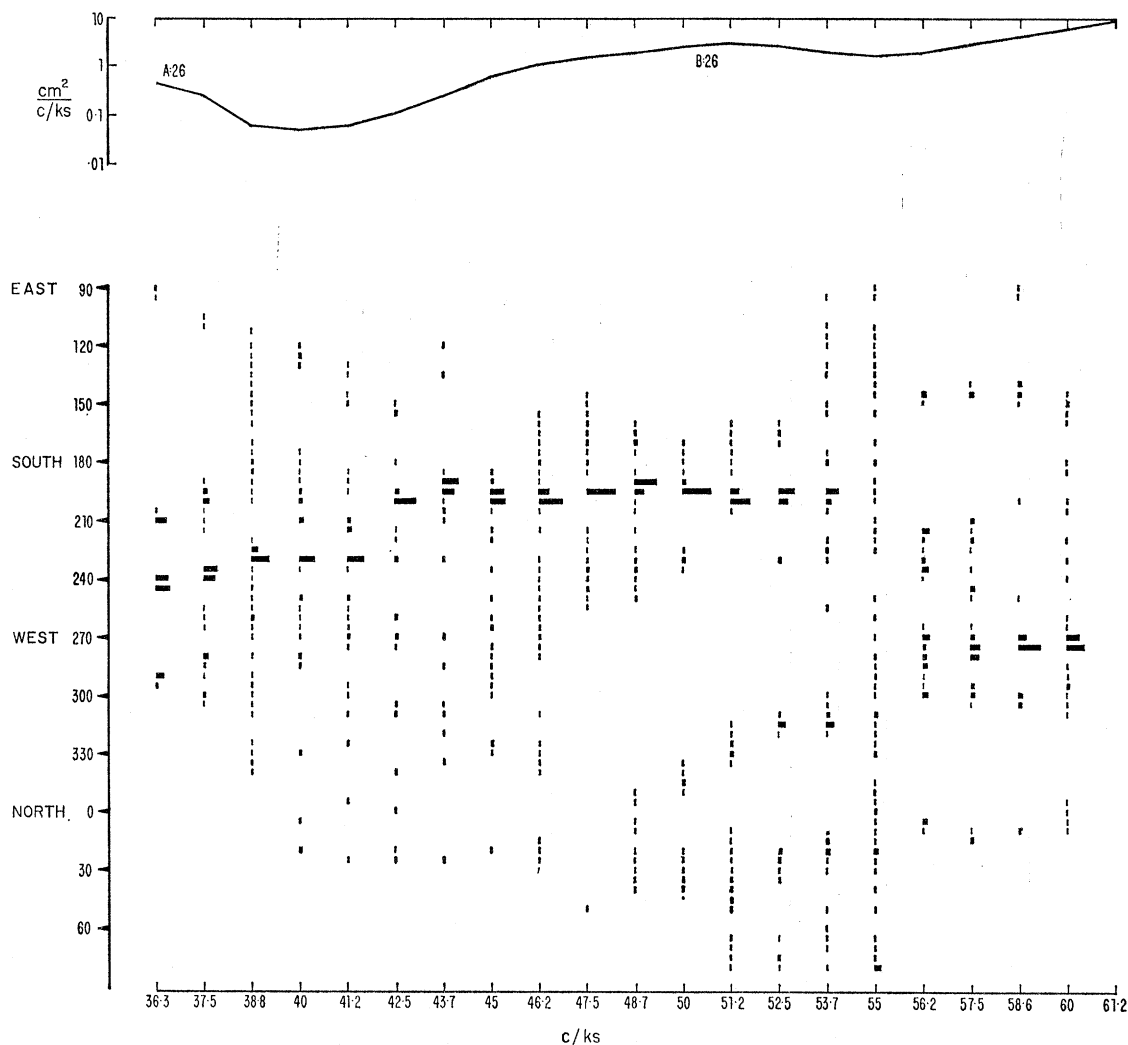


FIGURE 10. The top curve gives energy as a function of frequency on 26 October 1959. The central diagram gives the distribution of this energy among various directions, thus corresponding to a vertical cut in figure 17. For each frequency band the *relative* contribution of energy from directional bands of 5° width are indicated by the histogram. Unit histogram length is the ordinate distance between successive frequency bands. A single block of this length would imply that all energy is concentrated in this 5° interval. The sum of all blocks for any one frequency interval is unity. For example, in the frequency interval centred at 36.3 c/ks, 23% of the energy is between 242.5° and 247.5° T; 30% between 247.5° and 252.5° T; etc.

(f) *Fourier-Bessel analysis*

Another method that has been tried and discarded deserves a brief discussion. Suppose the power density at some fixed frequency is expanded in a Fourier series

$$E(\theta) = a_0 + \sum_{r=1}^R (a_r \cos r\theta + b_r \sin r\theta), \quad (7.12)$$

the dependence of E , a_r , b_r , on frequency being understood. We now evaluate C and Q according to (6.9, 6.10), setting

$$l = k \cos \theta, \quad m = k \sin \theta,$$

$$X_n = D_n \cos \theta_n, \quad Y_n = D_n \sin \theta_n,$$

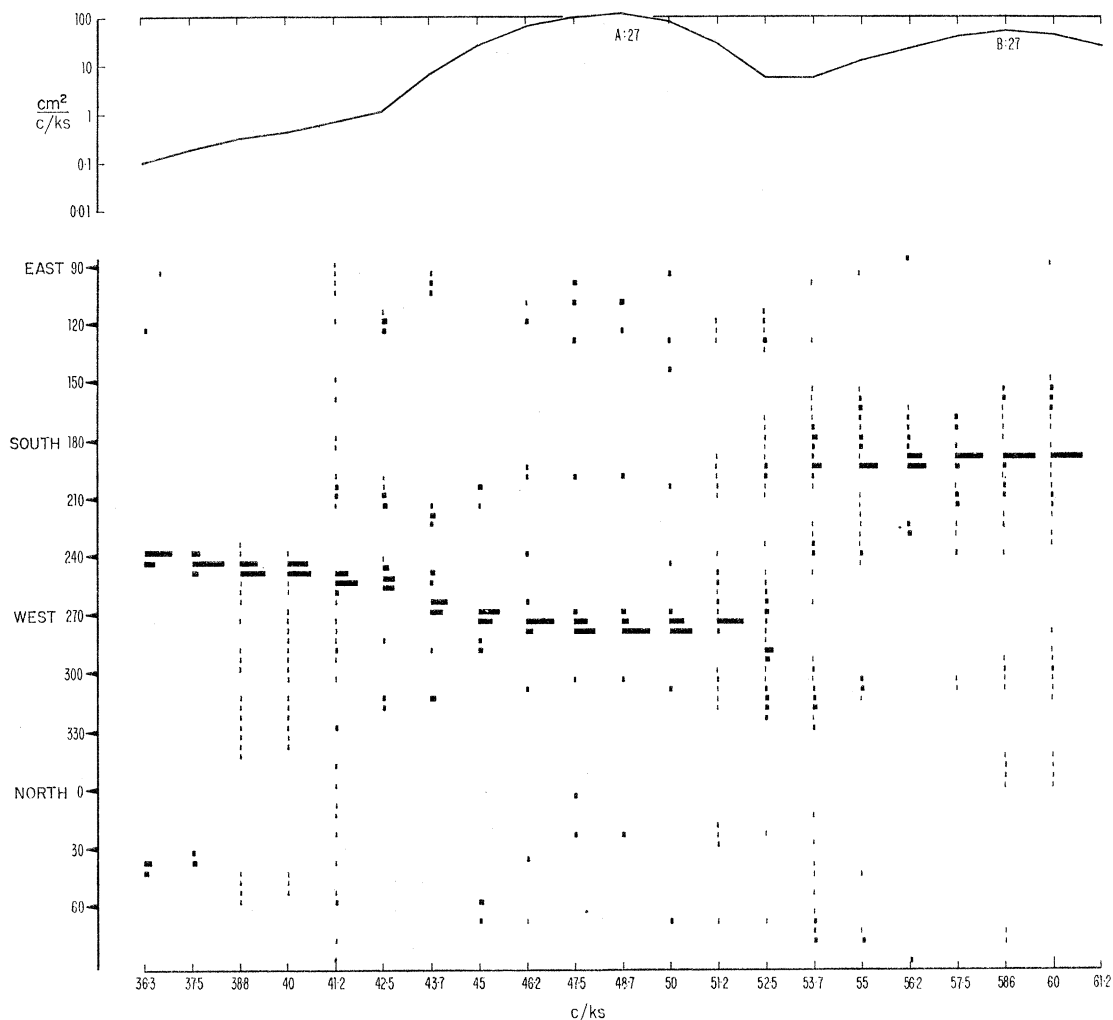


FIGURE 11. The directional wave spectrum on 27 October 1959 (see legend to figure 10).

where θ_n is the direction of the line connecting a pair of instruments and D_n their separation; the subscript $n = 1, 2, 3$ is in accordance with our previous sign convention. The result is

$$\left. \begin{aligned} C_0 &= \pi a_0, \\ C_n &= 2\pi \sum_{r=0, 2, 4, \dots} (a_r \sin r\theta_n - b_r \cos r\theta_n) J_r(2\pi k D_n), \\ Q_n &= 2\pi \sum_{r=1, 3, 5, \dots} (a_r \cos r\theta_n + b_r \sin r\theta_n) J_r(2\pi k D_n). \end{aligned} \right\} \quad (7.13)$$

Here are only seven equations relating the unknown Fourier coefficients. It is of some help that the Bessel coefficients of high order are small and might be ignored. Thus for wave of length three times the separation of the detectors the coefficient $J_5(2\pi k D)$ is only 0.01. If the geophysical situation were such that one could expect a very broad angular distribution of power (and this might well be the case in an area of wave generation), one might

ignore Fourier harmonics of order higher than 2. This would leave only five unknowns, a_0 , a_1 , b_1 , a_2 and b_2 to be fitted by least-square methods to the seven equations. But waves from distant storms tend to have a well-defined direction and the Fourier harmonics of high order are not small. The Fourier-Bessel analysis seems more appropriate to experiments with more detectors (four instruments for example would provide thirteen equations) and

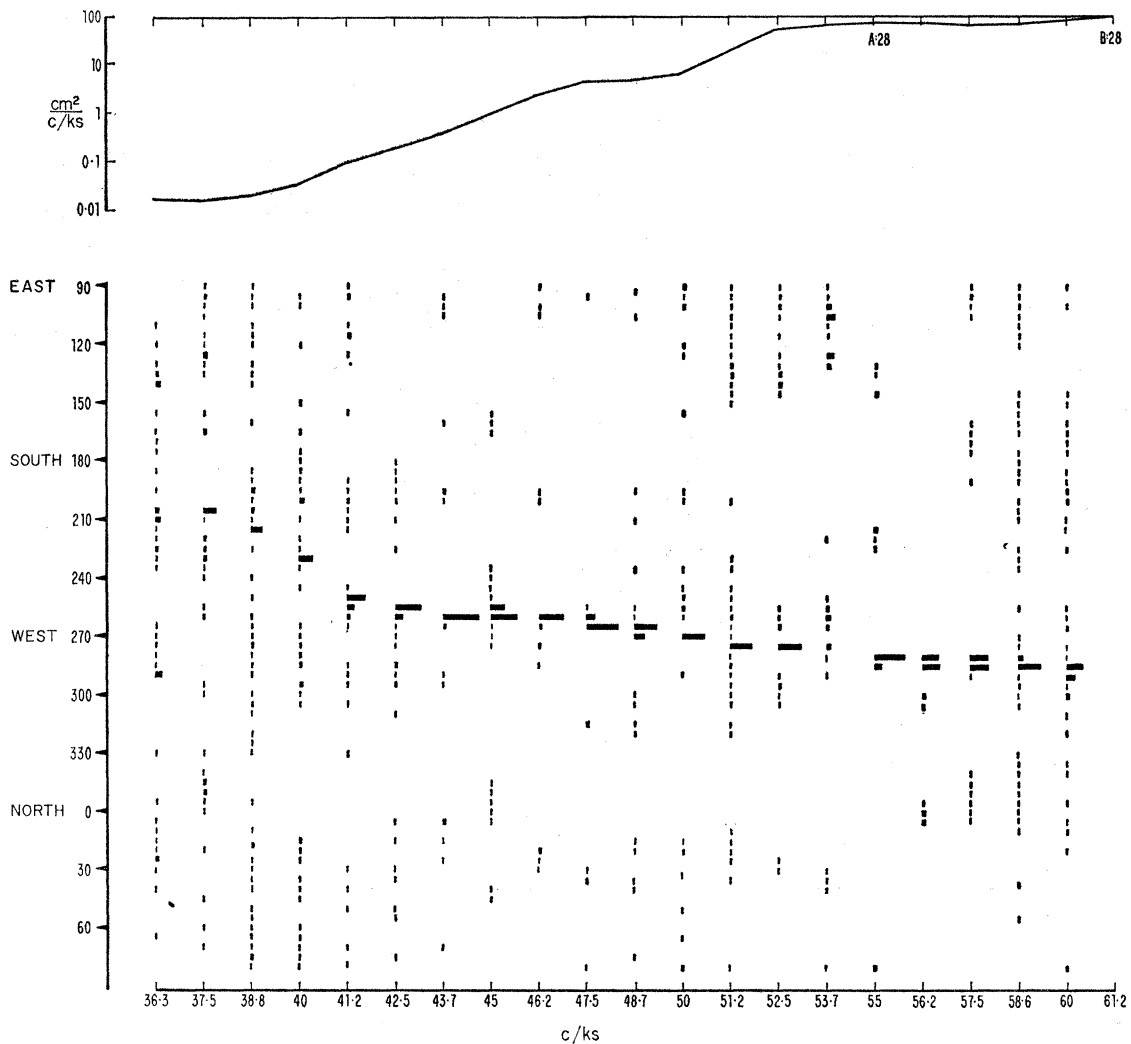


FIGURE 12. The directional wave spectrum on 28 October 1959 (see legend to figure 10).

to cases where the wave energy varies more gradually with wave direction. In the present experiment it seems better to fit the data as well as possible by one or more well directed wave trains such as would be produced by one or more storms at a great distance.

(g) Other methods

A number of attempts were made to use more fully the seven items of information given by the C 's and Q 's. At the assigned (theoretical) wave number some angular distribution of power was chosen that could be described by seven parameters, and the C 's and Q 's were used to decide the parametric values. These attempts were unsuccessful, perhaps for the

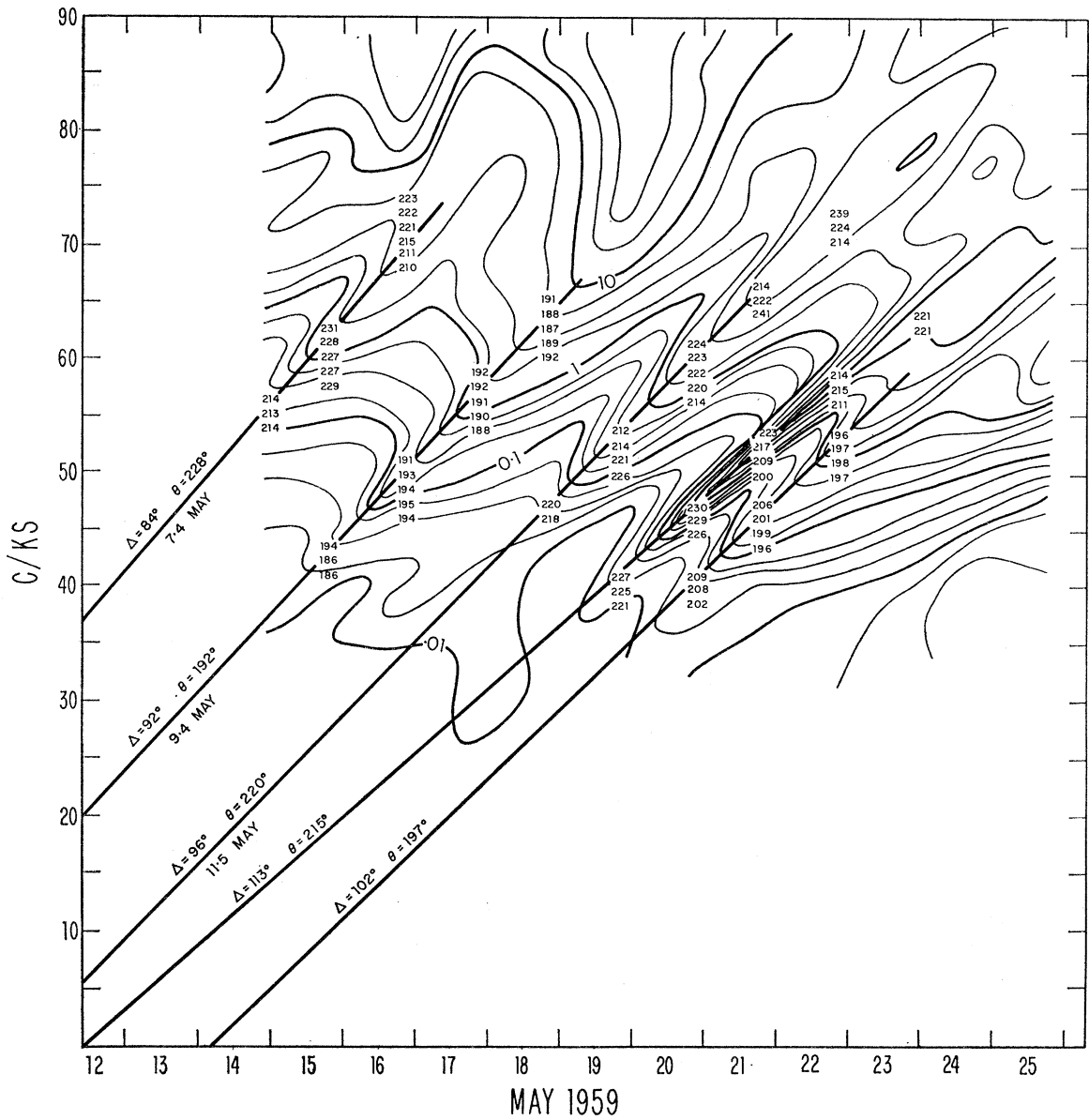


FIGURE 13. Contours of equal power density, $E(f, t)$, on a frequency-time plot. The contours are at equal intervals of $\log E(f, t)$. Heavy contours correspond to 0.01, 0.1, 1.0, and 10 $\text{cm}^2/(\text{c}/\text{ks})$. On the time axis the ticks designate midnight u.r. The ridge lines correspond to the dispersive arrivals from a single source, and their slope is inversely proportional to the distance from the source. For each ridge line we have marked the estimated direction, θ , of the source (clockwise from true north) and the great circle distance Δ in degrees. The small numbers give some computed directions of the optimum point source, $\theta_0(f, t)$.

following reasons. At low frequencies kD_n is always small, and then (7.10) shows that the Q 's tend to have a zero total

$$\sum_1^{n=3} Q_n = 0.$$

There are then only six items of information and seven parameters become indeterminate. At higher frequencies this restriction does not hold, but in all the experiments it must be

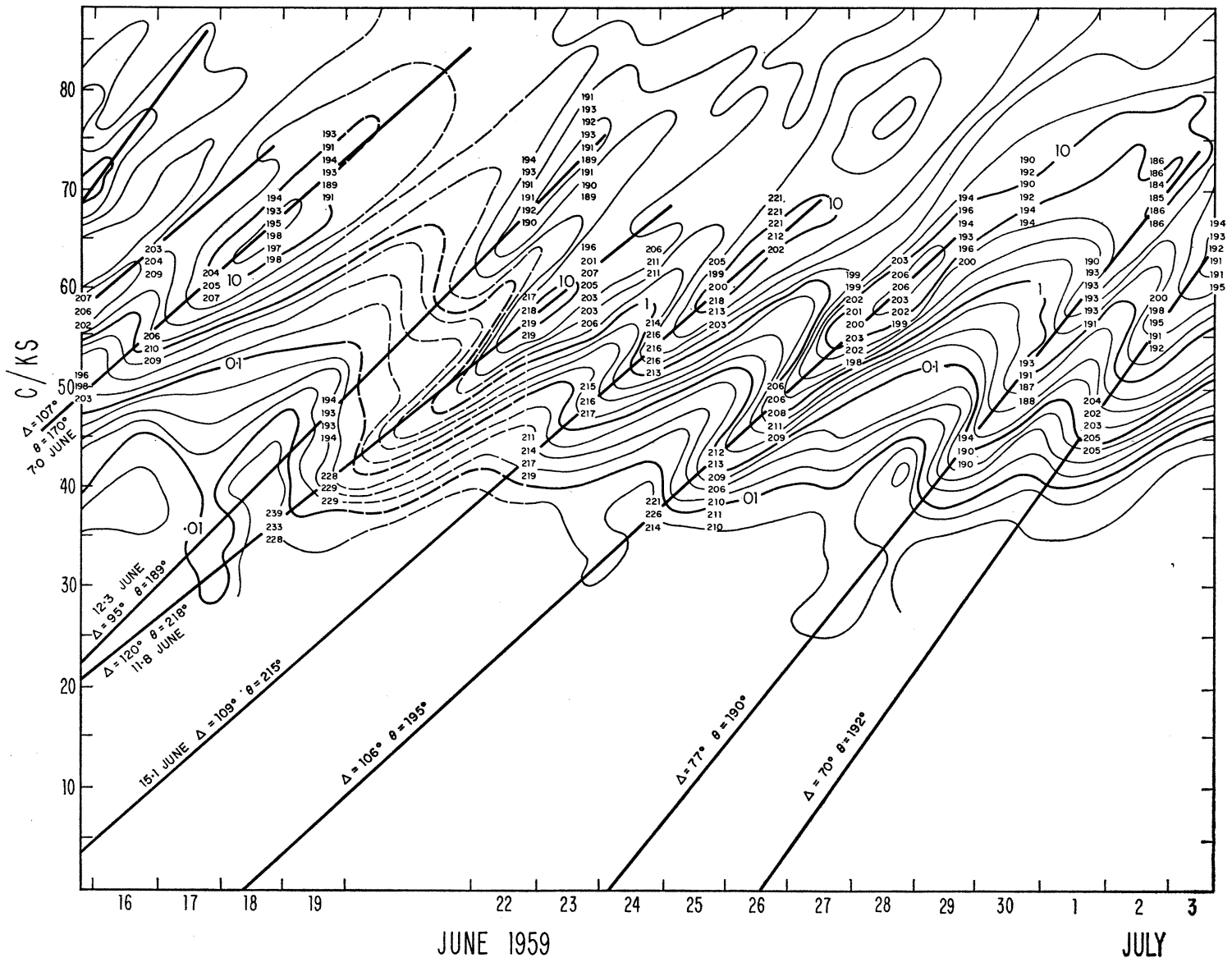
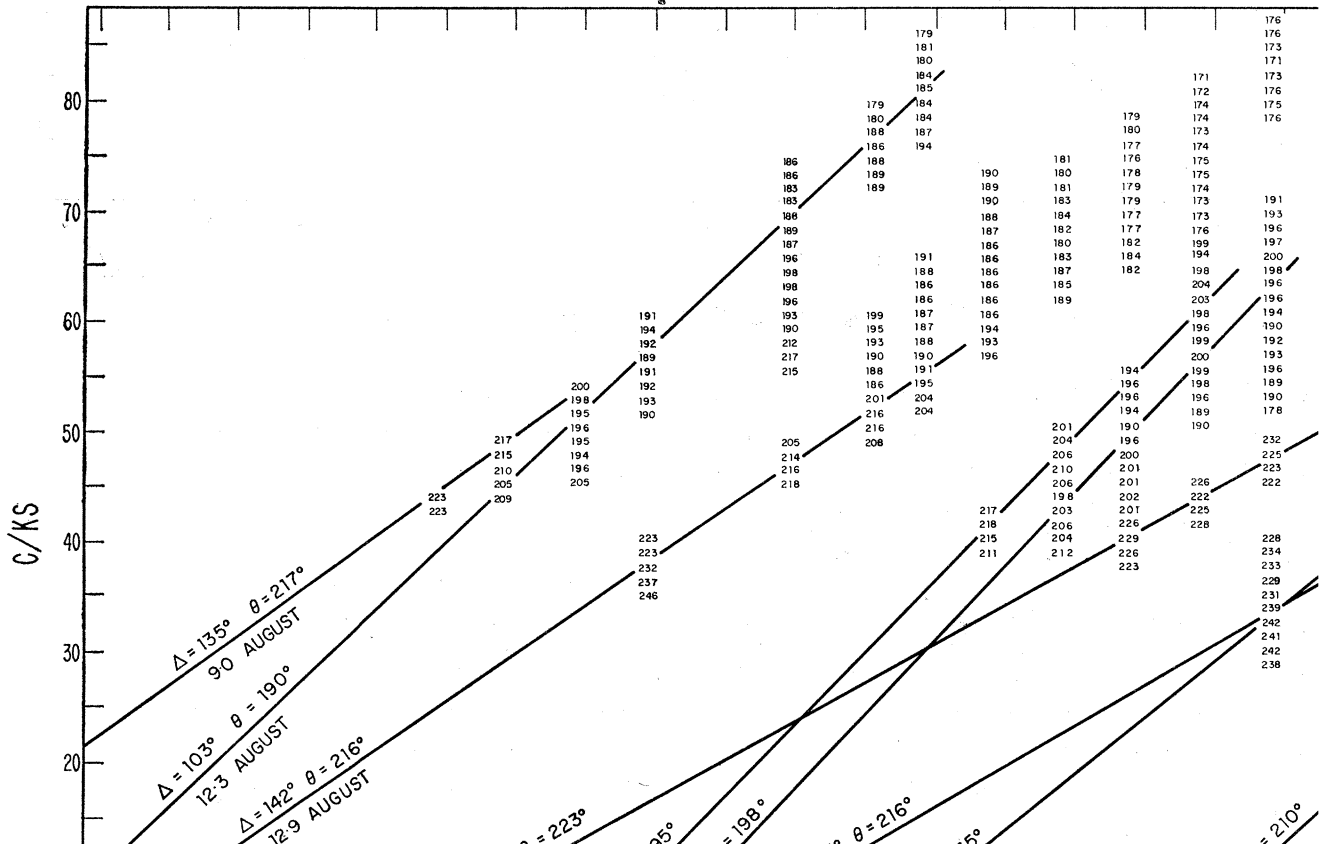
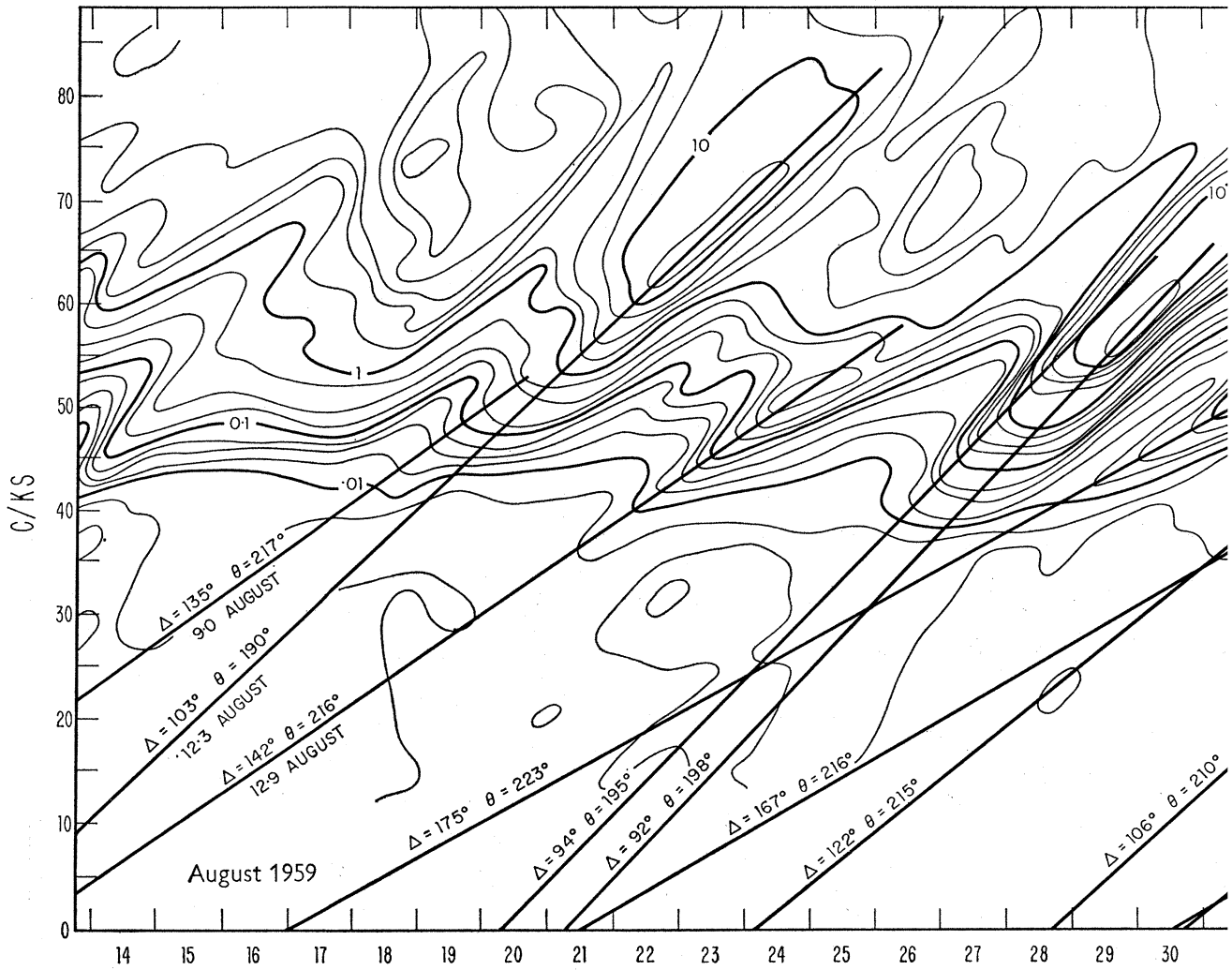
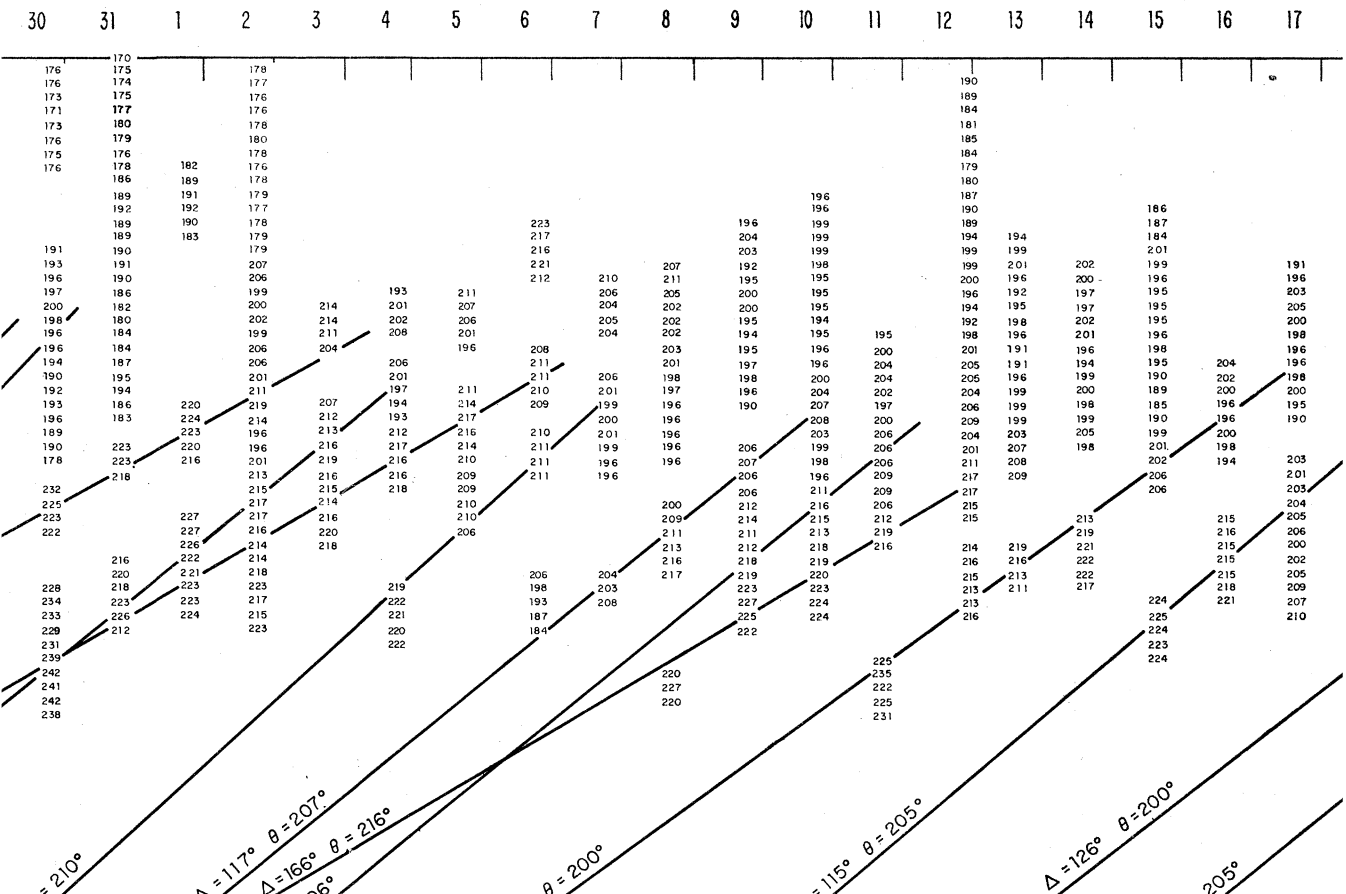
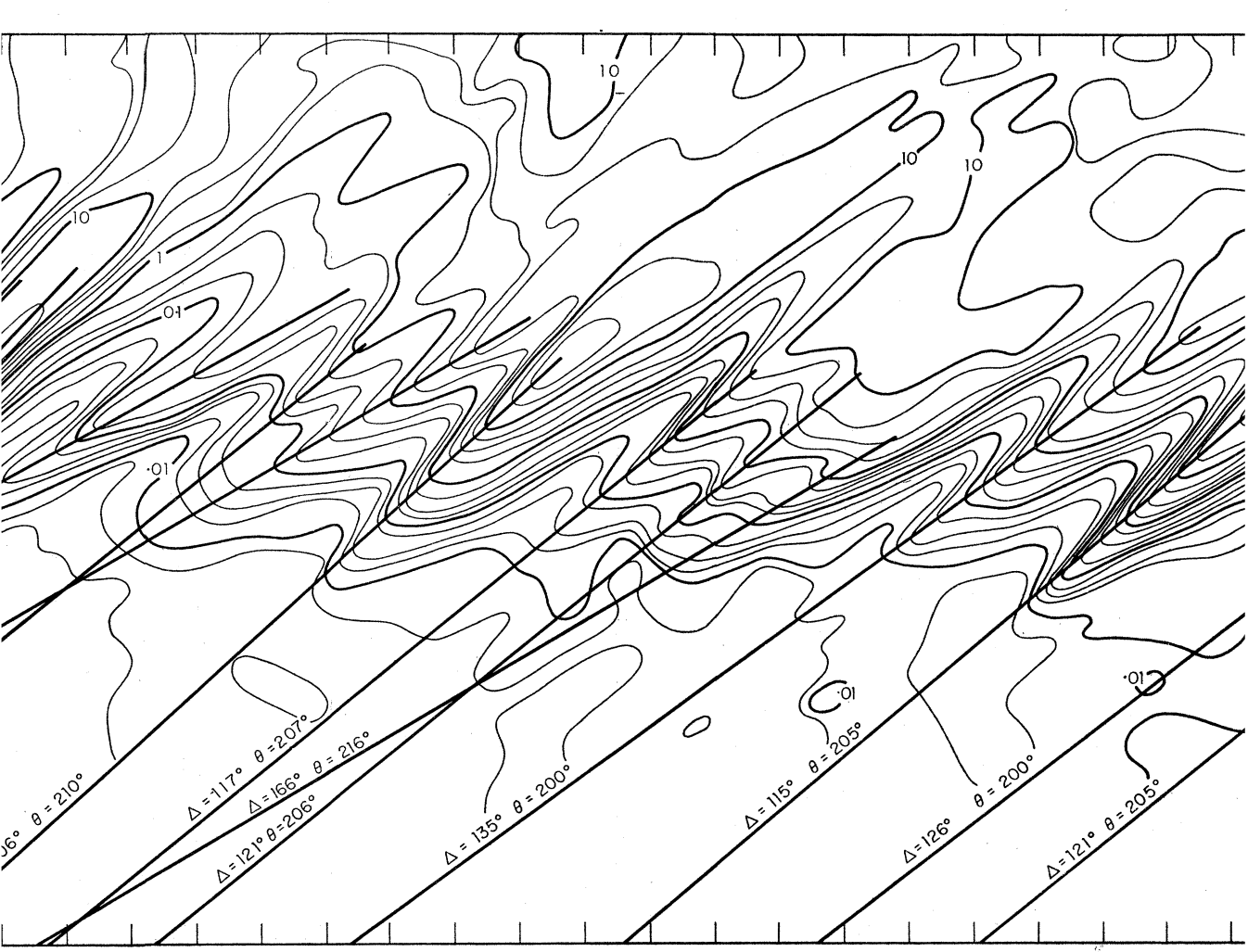


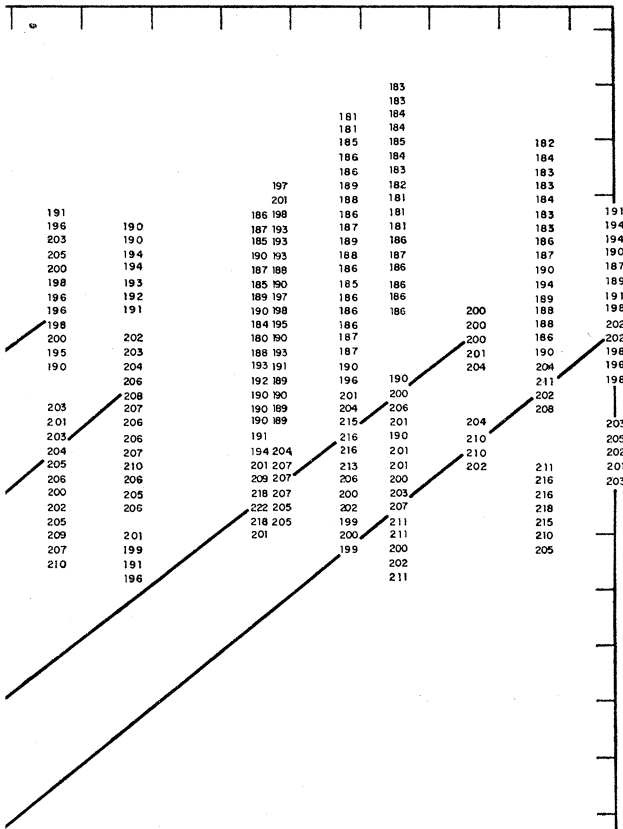
FIGURE 14. See legend to figure 13.

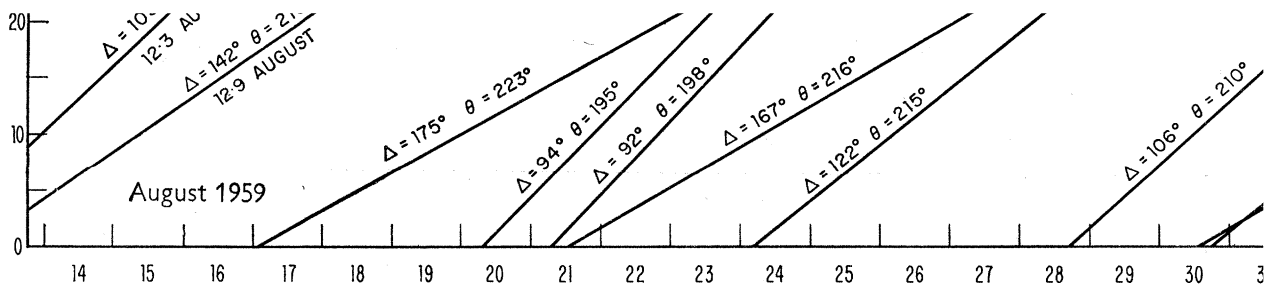
recognized that the C 's and Q 's are not completely stable. They are subject to random errors whose standard deviation is about 13% of the true value (in consequence of the 60 degrees of freedom mentioned in §4(e)). Attempts to make an exact fit might well call for occasional negative values of incident power or cause the calculated power distribution to vary in an erratic way with frequency.

All the data were examined by finding a best-fitting single wave train. The only more elaborate method of analysis that was extensively used was the iteration system described in §7(d). Its results satisfy the two essential physical requirements that the power distribution it describes is nowhere negative and that power is associated only with waves of the correct wave number. It has been shown from artificial examples (figure 9) that in favourable circumstances the iteration process can distinguish waves from two or even three different directions.









Above. FIGURE 15. For legend see in figure 13. Directions are plotted in figure 16.

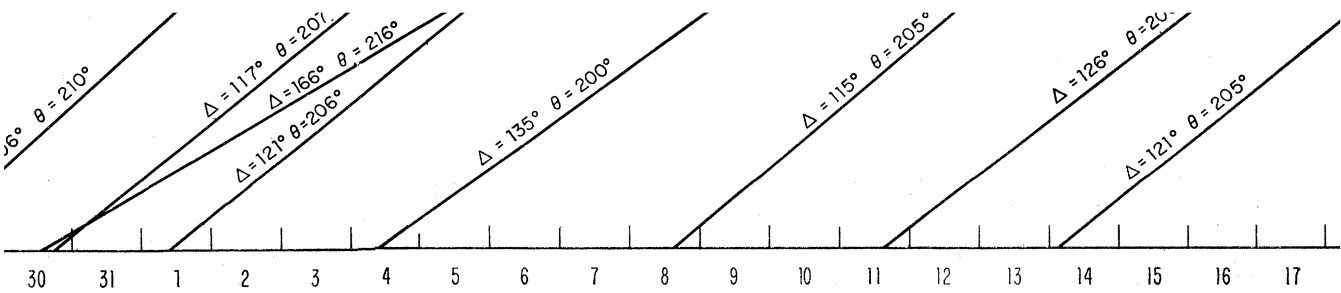
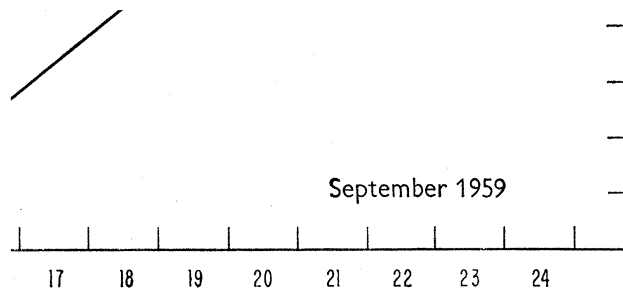
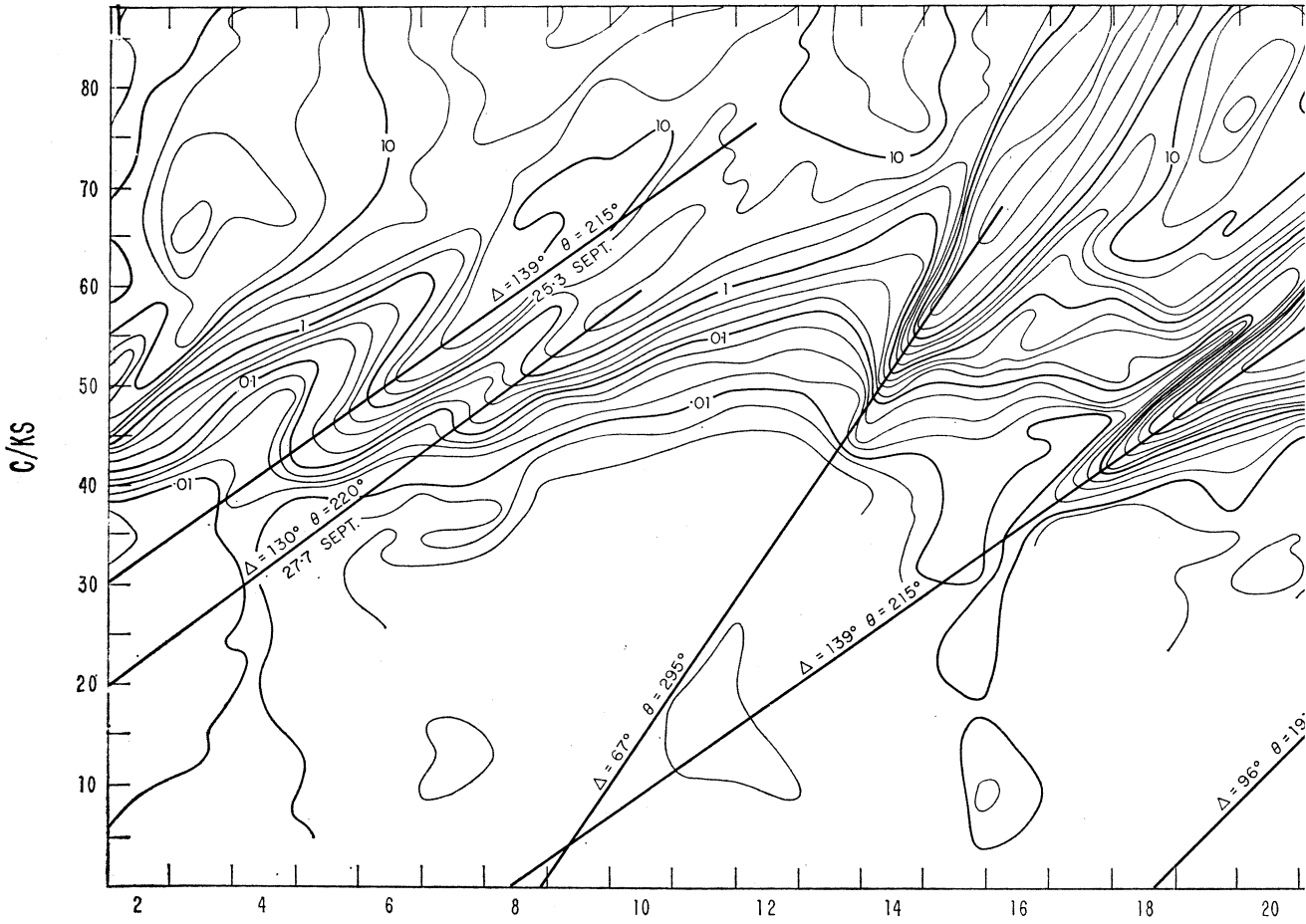


Figure 16.

Below. FIGURE 16. Direction of the optimum point sources, $\theta_0(f, t)$. The end

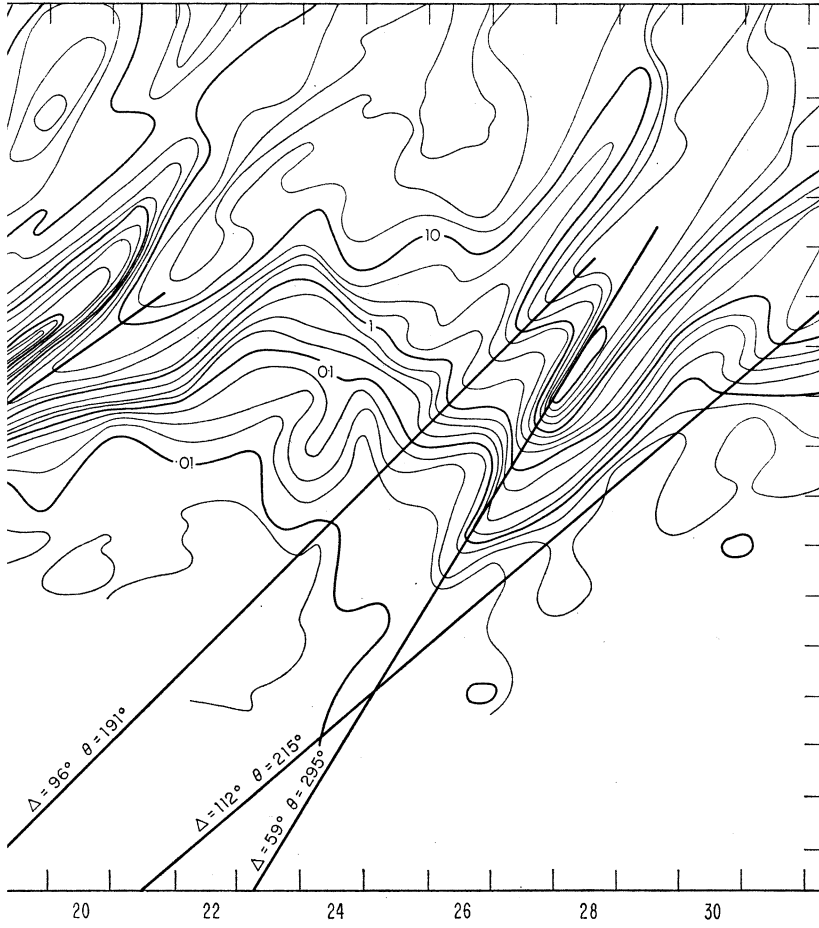


The energy spectrum is plotted in figure 15.

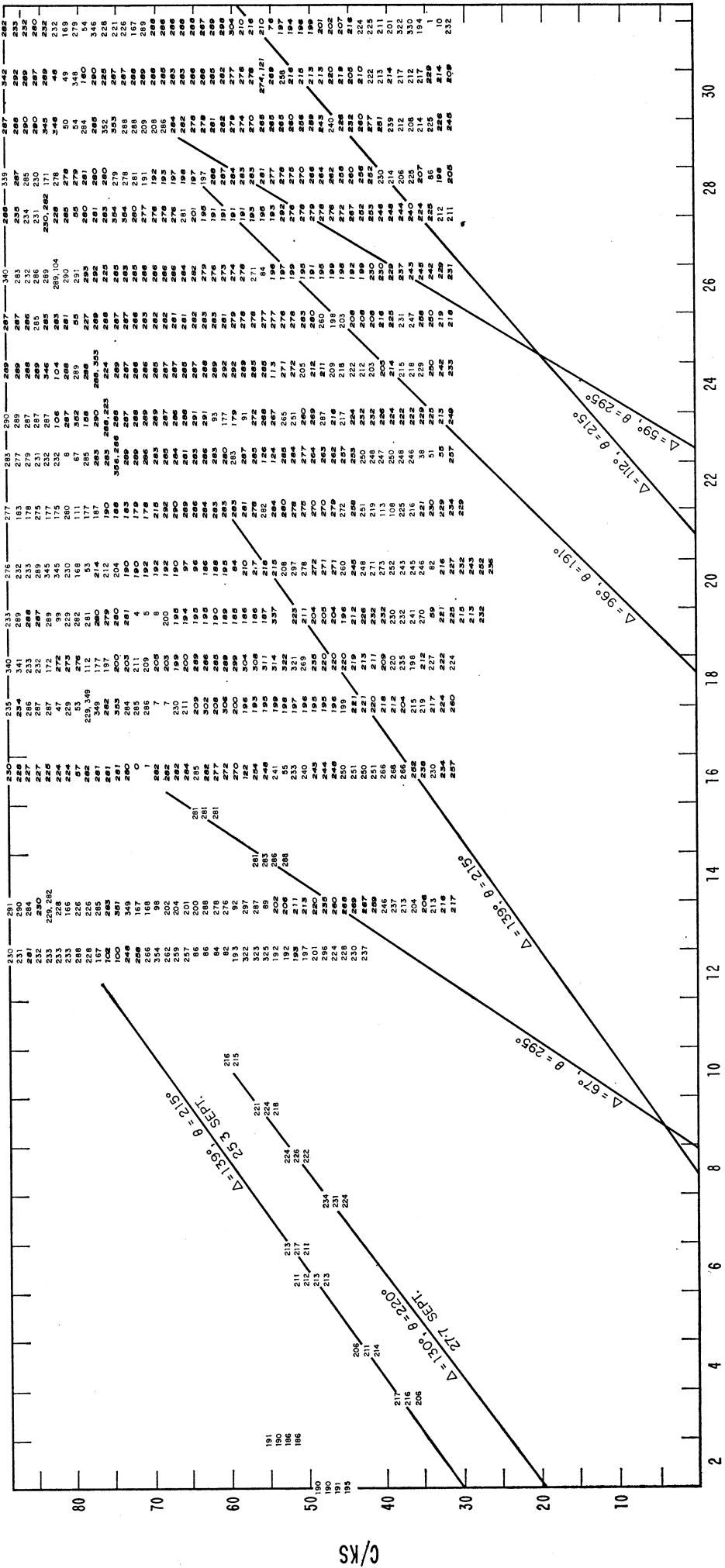


OCTOBER 1959

FIGURE 17. For legend see 13. Directions are plotted in figure 18. Cuts along fixed fre



; fixed frequencies are plotted in figures 20, 21 and 22.



OCTOBER 1959

FIGURE 18. The directions of the principal point sources as function of frequency and time. The bold numbers refer to cases when the point-source hypothesis is supported by the condition $\mathcal{H}_1 > 0.4$, or $\mathcal{H}_2 > 0.4$, or both (see §7(d)). For analyses based on two instruments only, the directions are entered along ridge lines but not elsewhere. Straight lines designate the ridges in the $E(f, t)$ topography (figure 17), with distances and directions indicated.

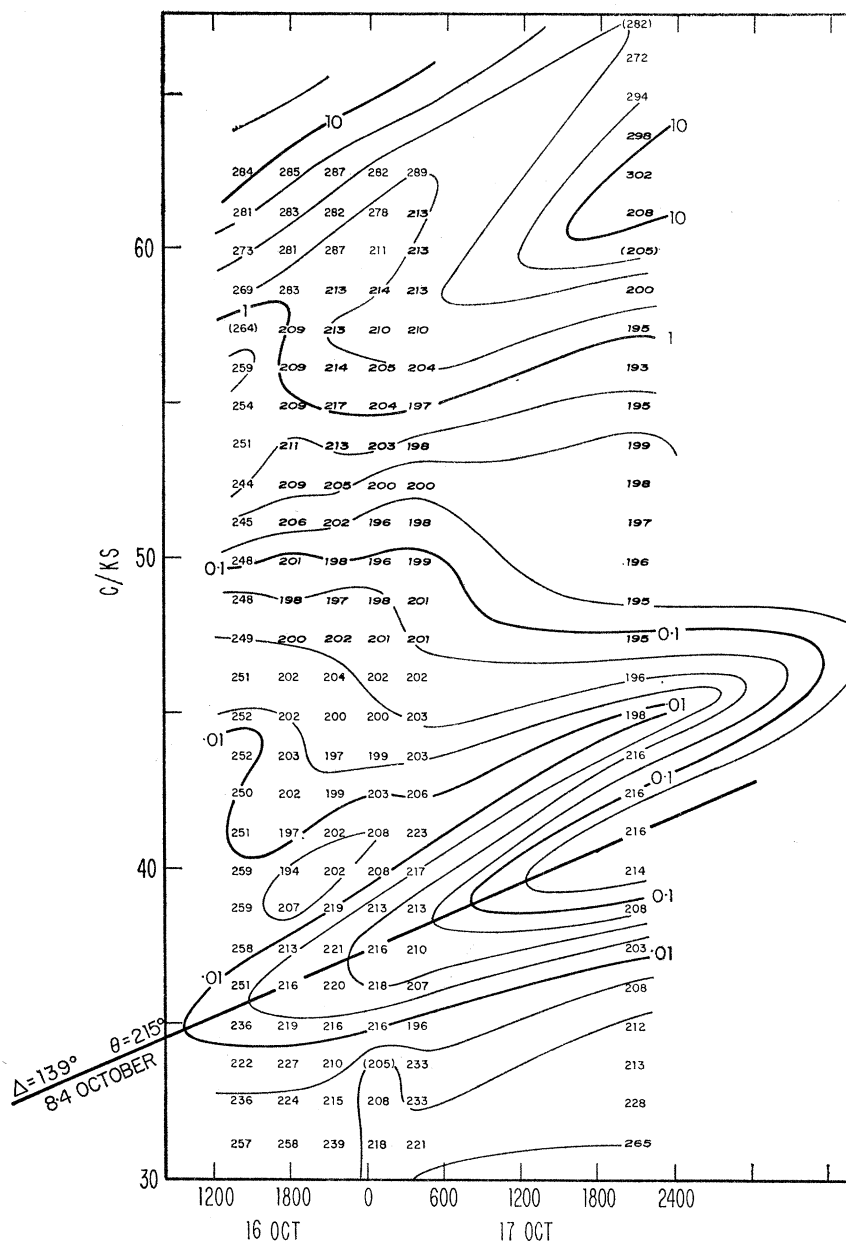


FIGURE 19. $E(f, t)$ and $\theta(f, t)$ on an expanded time scale, based on analyses at approximately 3 h intervals.

8. RESULTS

The results got by fitting a single wave train are summarized in figures 13 to 19. These display the relations $E(f, t)$, $\theta(f, t)$ and $E(\theta, t)$ respectively.

Figures 13, 14, 15, and 17 are contour charts of energy density as a function of frequency and time. For each day, the frequencies of standard energy levels were read off the power spectra (figure 4, for example) and marked along vertical lines. All points corresponding to a given level were then connected. The variations from day to day are continuous and there is little leeway in drawing these contours. Energy peaks associated with a given event appear as slanting ridges. The dispersion relation (5.6) predicts that these ridges should be straight, and they are.

The background level consists of a flat valley near $10^{-2} \text{ cm}^2/(\text{c/ks})$ for frequencies below 40 c/ks rising steeply to $10 \text{ cm}^2/(\text{c/ks})$ at 80 c/ks . Typically the ridges extend 10 to 100 times above the background level. Some ridges project into the low-frequency plain. The outstanding case is the ridge associated with the hurricane on 22 October which projects to

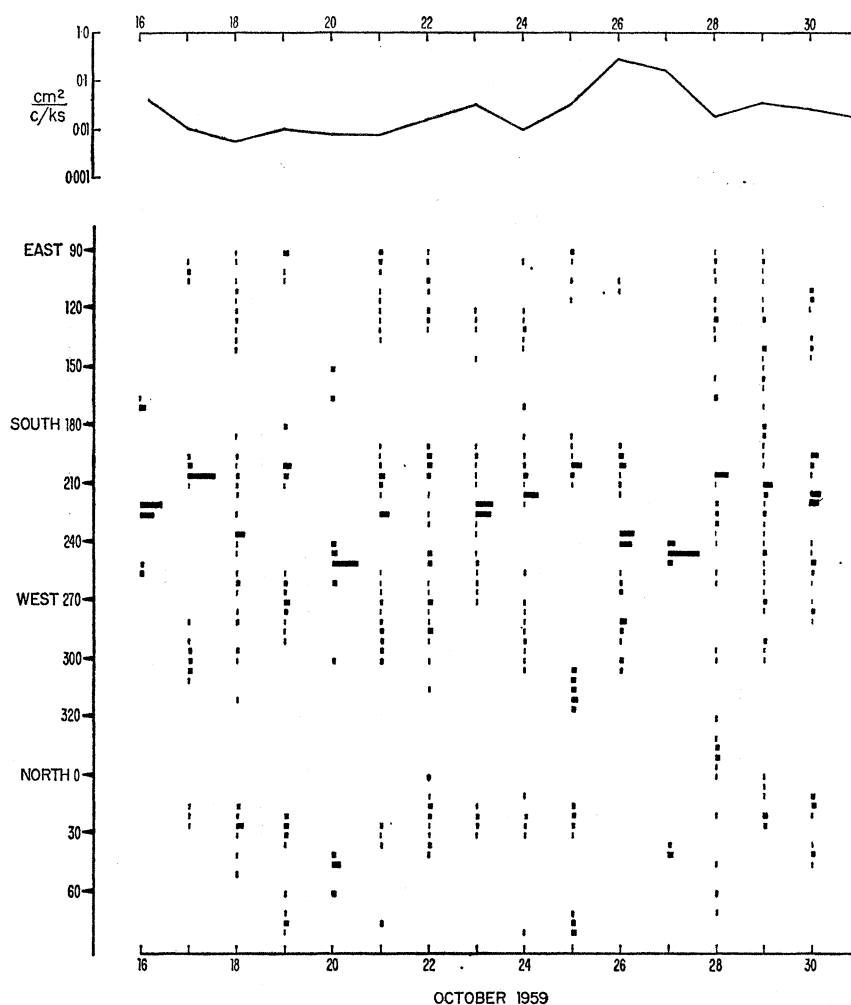


FIGURE 20. The top curve shows the energy density as a function of time in a narrow frequency band centred at 37.5 c/ks . This corresponds to a horizontal cut in figure 17. The central diagram gives the distribution of this energy among various directions. For each day the *relative* contribution of energy from directional bands of 5° width are indicated by the histogram. Unit histogram length is the ordinate distance between successive days. A single block of this length would imply that all energy is concentrated in this one 5° band. The sum of all blocks for any one day is unity. For example, on 27 October the energy density at 37.5 c/ks is $0.15 \text{ cm}^2/(\text{c/ks})$, and 64% of this energy comes from a directional interval 242.5 to 247.5° T .

frequencies as low as 30 c/ks (period 33 s). The corresponding deep-water wavelength is about a mile. The energy associated with the earliest arrival is roughly 0.1 cm^2 , and the r.m.s. amplitude is accordingly 3 mm. This appears to be the longest swell on record.

The slope of the ridge lines gives the distance of the source. Most ridges are associated with distances of the order of 100° ($\sim 10000 \text{ km}$). Exceptions are the relatively nearby

source of 22 October, due to a north Pacific hurricane, and three very distant events in August which have been traced to storms in the Indian Ocean (see § 14).

For the period May to September 1959 (figures 13 to 16), only the south-north pair of instruments was in operation. The directions of the major ridges have been determined by the method discussed in § 5, and the results are entered on the figures. During October all

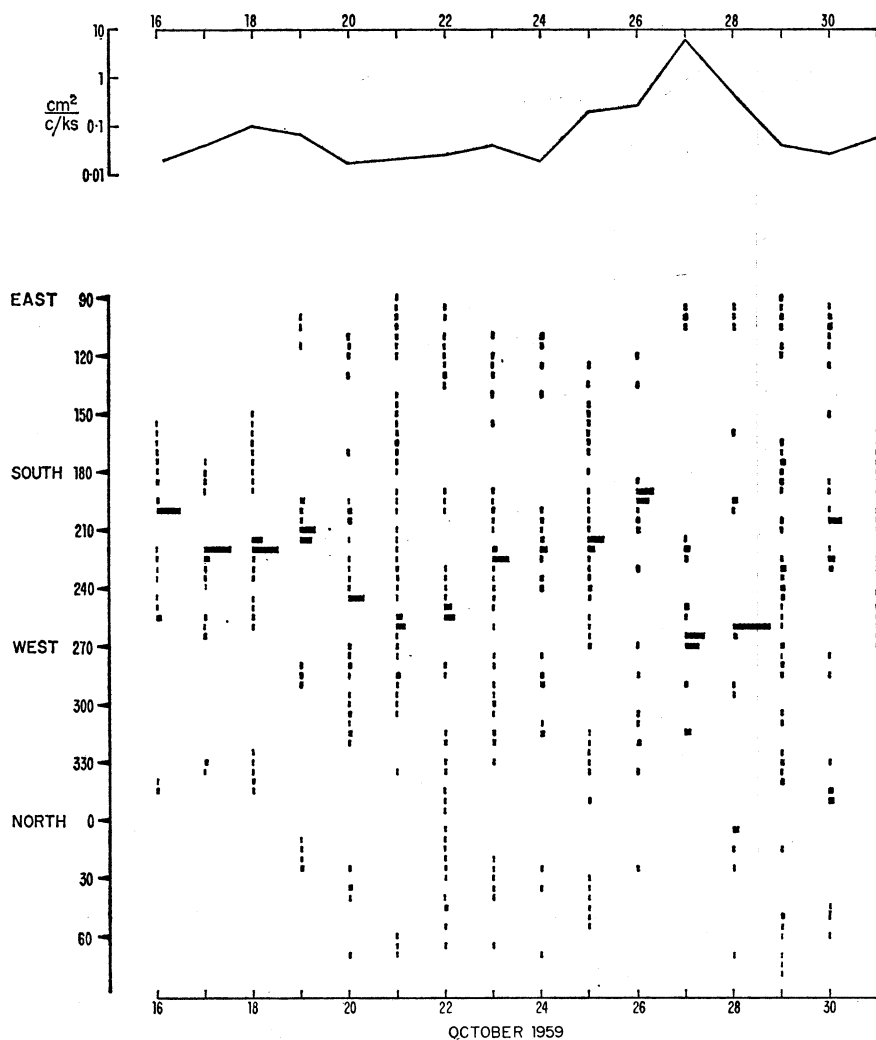


FIGURE 21. The distribution of wave energy among various directions for a frequency band centred at 44 c/ks during 16 successive days (see legend to figure 20).

three instruments were in operation, and it seemed worthwhile to present the complete field of $\theta(f, t)$ (figure 18). Figure 19 shows the fields of $E(f, t)$ for 16–17 October when spectra were taken at 3 h intervals (rather than the customary daily interval). At these close time intervals the energy and direction show the expected degree of continuity.

The contour charts of energy and direction on the $f-t$ diagrams contain most of the information obtained in our experiment. There are a number of interesting cuts. Vertical cuts (at a fixed time) reproduce the original spectra on which the contour charts are based. Horizontal cuts (at a fixed frequency) reveal a marked asymmetry of the slopes on the two sides of the ridges and give some information about the arrival of scattered energy. Cuts

along the ridge lines can be interpreted in terms of generation and decay processes. Examples are presented in the geophysical discussion.

The dependence on time of the directional distribution of energy at fixed frequencies is shown in figures 20 to 22.

Some results obtained by the iteration process are shown in figures 20 to 22. These purport to show the distribution of energy with direction at three selected frequencies and the manner in which this changes from day to day.

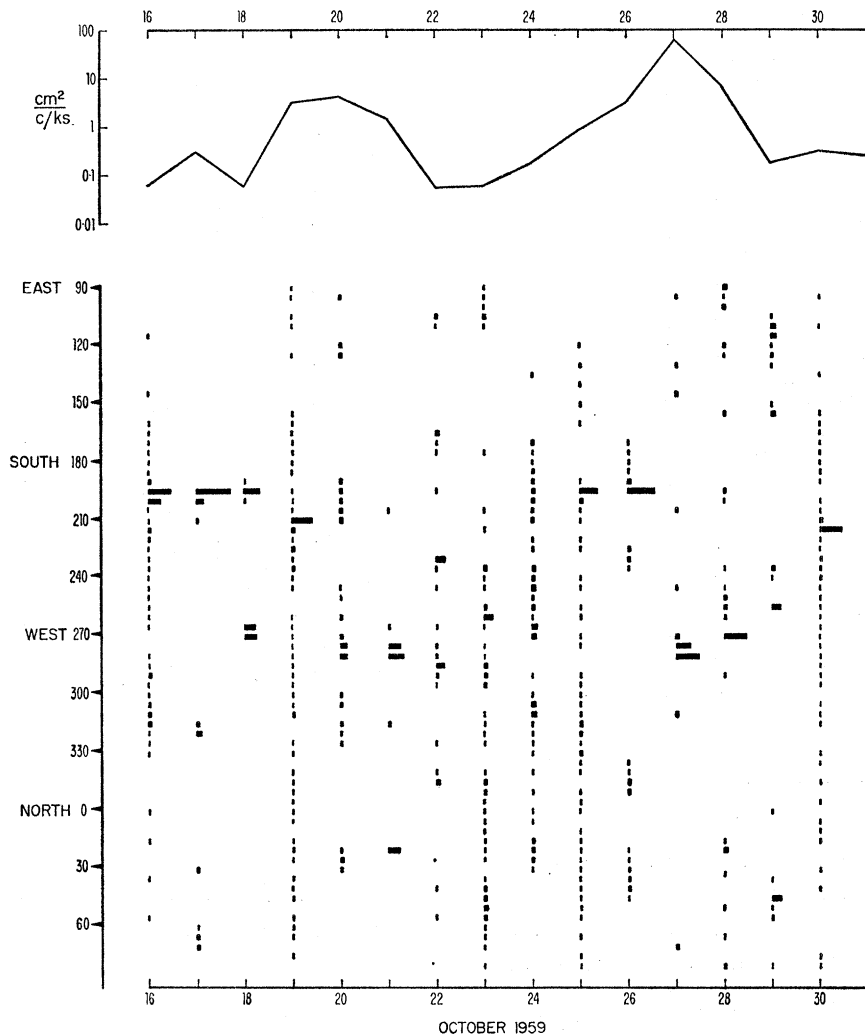


FIGURE 22. The distribution of wave energy among various directions for a frequency band centred at 50 c/ks for 16 successive days (see legend to figure 20).

9. REFRACTION

The direction of waves in shallow water is altered by refraction. The effect is very small for wavelengths shorter than three times the depth (say). In our case the depth is 100 m and the effect is unimportant for frequencies exceeding 70 c/ks.

At very low frequencies the $f-\theta$ diagrams exhibit a tendency for the wave direction to swing normal to shore, as expected. But these diagrams are not the proper presentation for distinguishing the effect of refraction from the effects of moving sources and multiple

sources. The $f-\theta$ diagrams are drawn for a *fixed time of arrival*; consequently different frequencies are associated with different times of origin, with the lowest frequencies corresponding to the most recent source (since the straight lines do not generally intersect). What is needed is a diagram corresponding to a *fixed time of origin*.

As an illustration we again refer to the hurricane of 22 October (figure 23). Let $f = a + bt$ designate the 'ridge' on figure 15 associated with this hurricane. For each of the five days 25 to 29 October ($t = t_i, i = 1, 2, \dots, 5$) we have selected the frequency band nearest

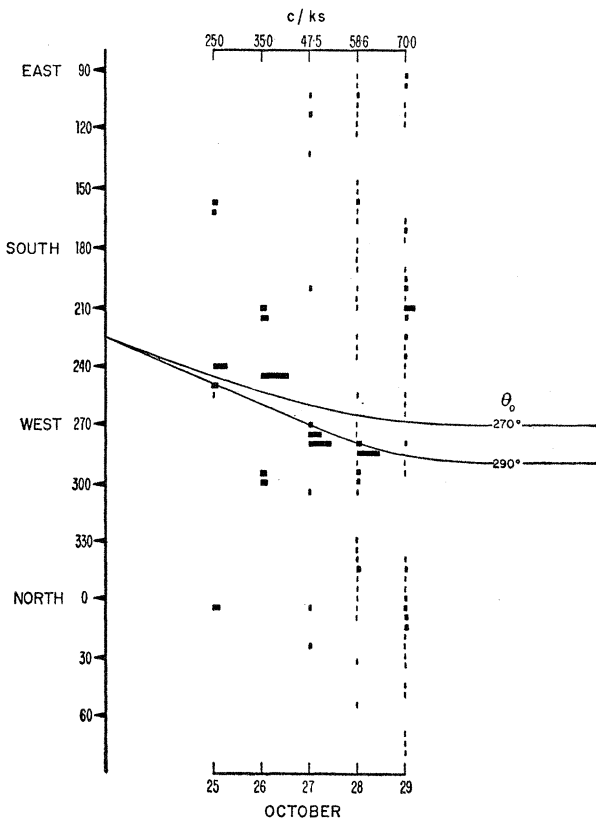


FIGURE 23. Directional distribution of energy associated with the hurricane of 22 October 1959. For each of the 5 days 25 to 29 October (lower scale) the frequency band was selected whose centre frequency (upper scale) was nearest the $f-t$ ridge. Computed directions are plotted for off-shore directions of 270 and 290°, respectively.

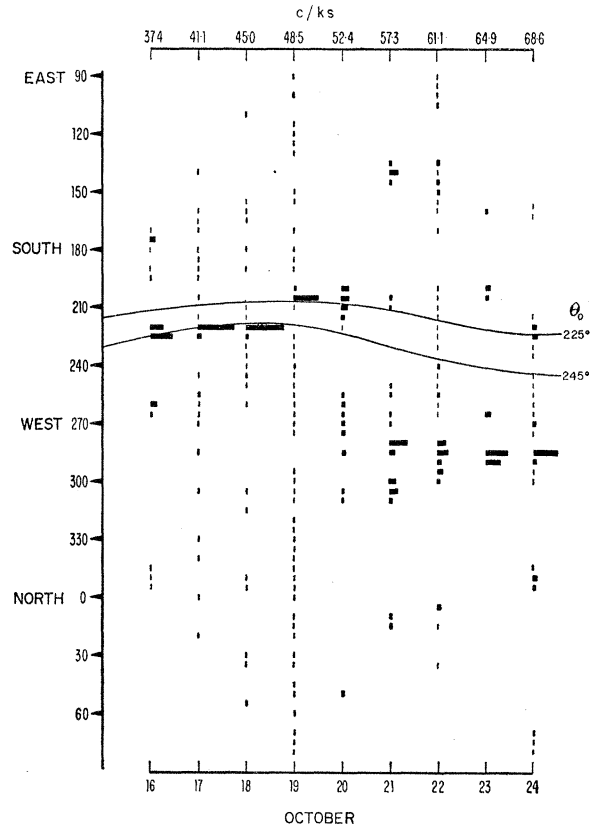


FIGURE 24. Directional distribution of energy associated with the storm of 8 October. See legend figure 23.

$f(t_i) = a + bt_i$; and plotted $E[f(t_i), \theta]$. This can be regarded as an oblique cut along a plane $f = a + bt$ of the three-dimensional distribution $E(f, \theta, t)$. Another example is shown in figure 24. The variation in direction at the low frequencies is attributed to refraction.

There are two regions which contribute to the refraction of the incoming waves. One region is just off-shore from the wave recorders (figure 1); the other is a series of shoals 60 km to the south-west (figure 25). In figure 26 the rays (or orthogonals, or crest-normals) have been constructed for intervals of 5° of recorded direction at the frequency 37.5 c/ks;

similar refraction diagrams were prepared for other frequencies. Figure 27 is a plot of recorded direction against off-shore direction, beyond the shoal areas. At high frequencies the refraction is negligible throughout and the two directions are equal, as indicated. For very low frequencies the recorded directions lie in a narrow interval about the normal to the shore line.

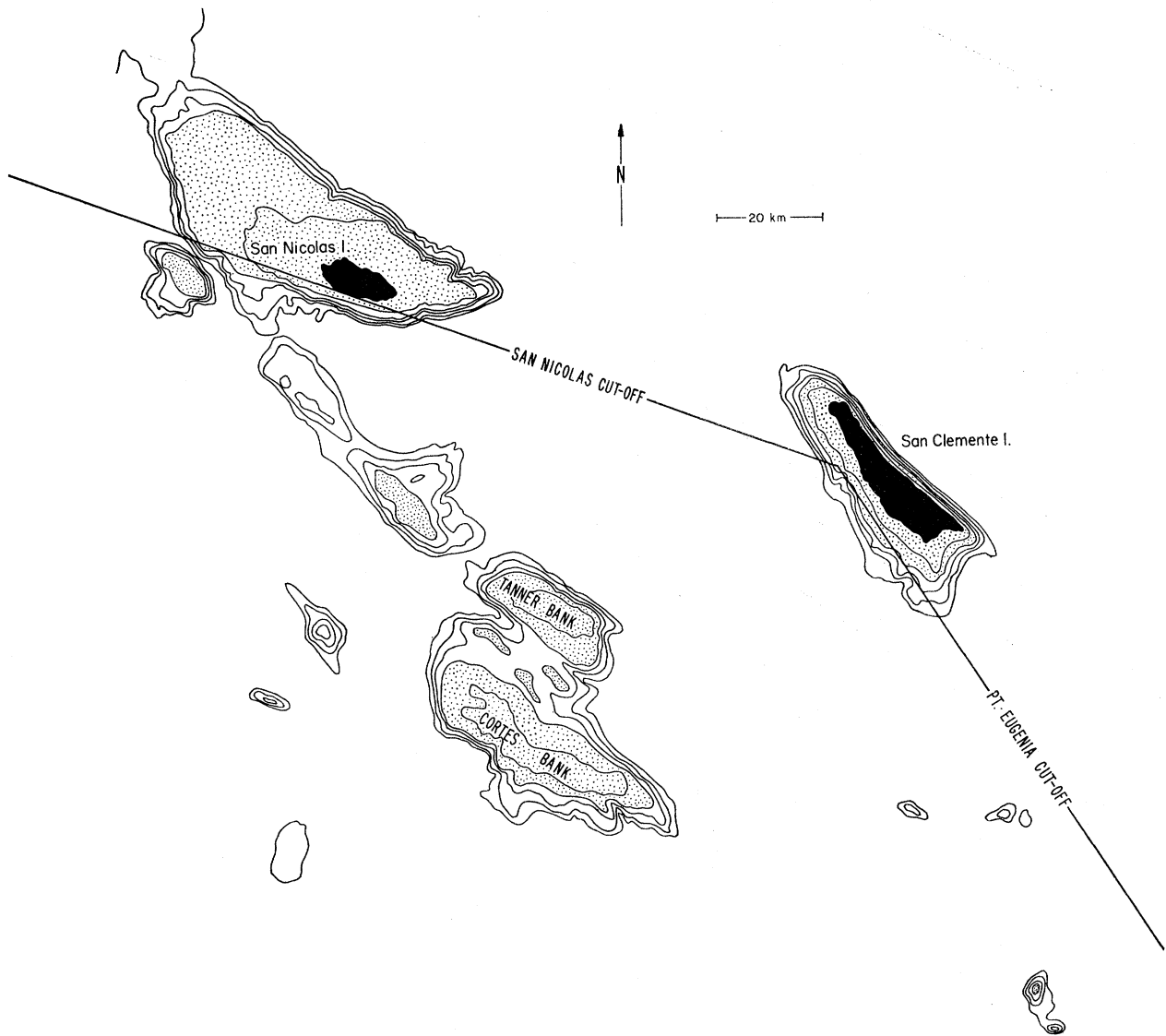


FIGURE 25. The continental borderland off San Clemente Island. Depth contours are drawn for 0, 50, 100, 150, 200 and 250 fm. Areas shallower than 100 fm are shaded. Incoming waves are limited by San Nicolas Island to the north and Point Eugenia on Baja California to the south.

To help visualize the expected dependence of wave direction on frequency, we have plotted the solution to the ray-optics problem for two idealized cases. Figure 28 shows the refraction by a cylindrical shoal (depth 200 m) for a recorder located in deep water (800 m) at a distance of two shoal diameters. For comparison with observations we wish to display the result on a diagram with frequency and recorded direction as co-ordinates, drawing lines of equal off-shore direction (figure 29 right). Rays exceeding a critical angle

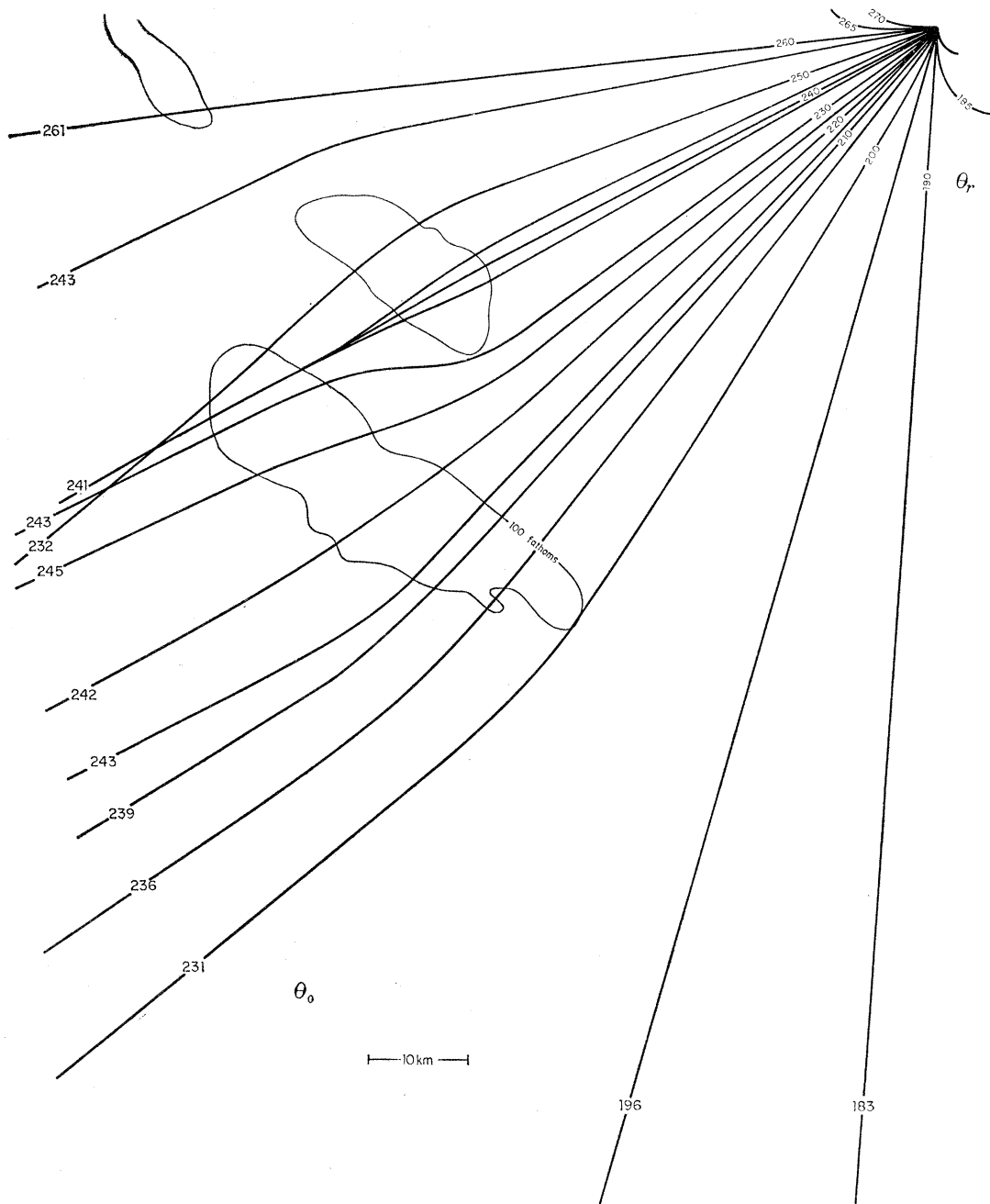


FIGURE 26. The refraction of waves of frequency 37.5 c/ks in the region shown in figure 25. Dashed curves give the 100 fm contours. The solid lines correspond to rays intersecting at the position of the wave recorders. These are drawn for recorded directions of 185, 190, ... 270°. The off-shore directions are indicated.

$\arcsin(\frac{1}{4}) = 14^\circ \cdot 5$ at the recorder are not refracted and appear as vertical lines. For any off-shore direction exceeding the critical value there are two recorded directions, the direct ray and the refracted ray. Suppose $\theta_0 = +20^\circ$. For the direct ray $\theta_r = +20^\circ$; for the refracted ray at 20 c/ks $\theta_r = -8^\circ$ (in the half of the diagram not shown). Figure 29 left shows the corresponding pattern associated with straight parallel contours. The actual situation is in a sense a combination of the two examples, and the relations are complex.

The computed directions are shown in figures 23 and 24. Agreement with observations is somewhat disappointing. In estimating the off-shore direction of other major wave trains we have paid attention largely to the higher frequencies which are relatively unaffected by refraction, keeping, however, in mind the expected refraction at lower frequencies as developed in this section. The essential result is that waves from east of 180° are recorded at nearly 180° , and waves from north of 270° at nearly 270° . Accordingly the direction of storms in the south-east and north-west Pacific are poorly determined.

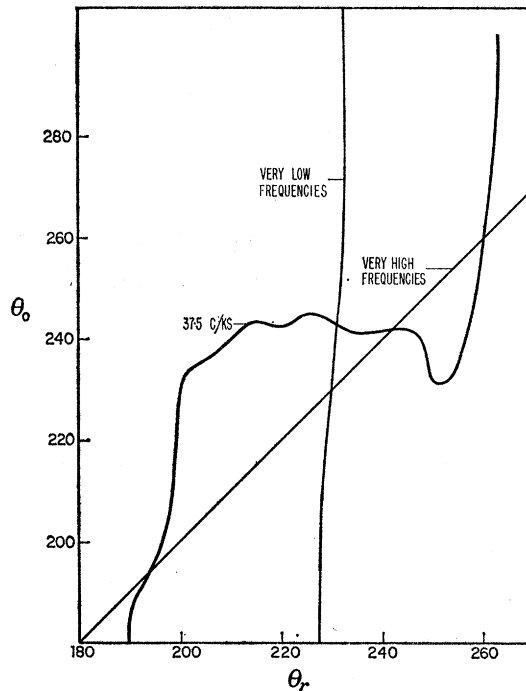


FIGURE 27. Recorded versus off-shore direction for various frequencies.

Nothing has been said thus far about the relation between the recorded spectral densities and those in the open sea before the waves are refracted. This relation can be computed from the result deduced by Longuet-Higgins (1957) that the energy density in wave-number space is conserved. We take the special case of a swell contained within narrow limits of frequency $f \pm \frac{1}{2}\delta f$, and direction $\theta \pm \frac{1}{2}\delta\theta$. The corresponding wave-number limits $k \pm \delta k$ are readily computed from the dispersion relation

$$2\pi f^2 = gk \tanh(2\pi kh).$$

The problem of an off-shore source at near-shore receiver is equivalent to that of a near-shore source and off-shore receiver, by the principle of reciprocity. At the recorder both k and δk will be larger than in deep water (figure 30). The energy in the swell can be written

$$E(l, m) k \delta k \delta\theta,$$

where $E(l, m)$ is the average energy density in the elementary area. The ratio of off-shore energy to recorded energy equals

$$\frac{k_0}{k_r} \frac{\delta k_0}{\delta k_r} \left| \frac{\delta\theta_0}{\delta\theta_r} \right| = \frac{C_r}{C_0} \frac{V_r}{V_0} \frac{\delta\theta_0}{\delta\theta_r}$$

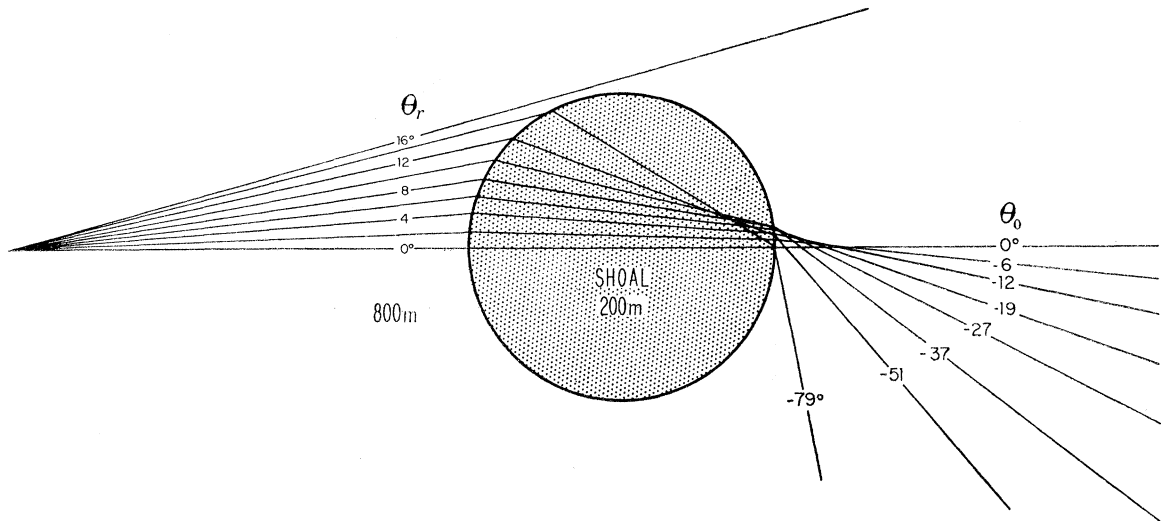


FIGURE 28. Ray diagram for an off-shore shoal at very low frequencies. The depth contrast is 4:1.

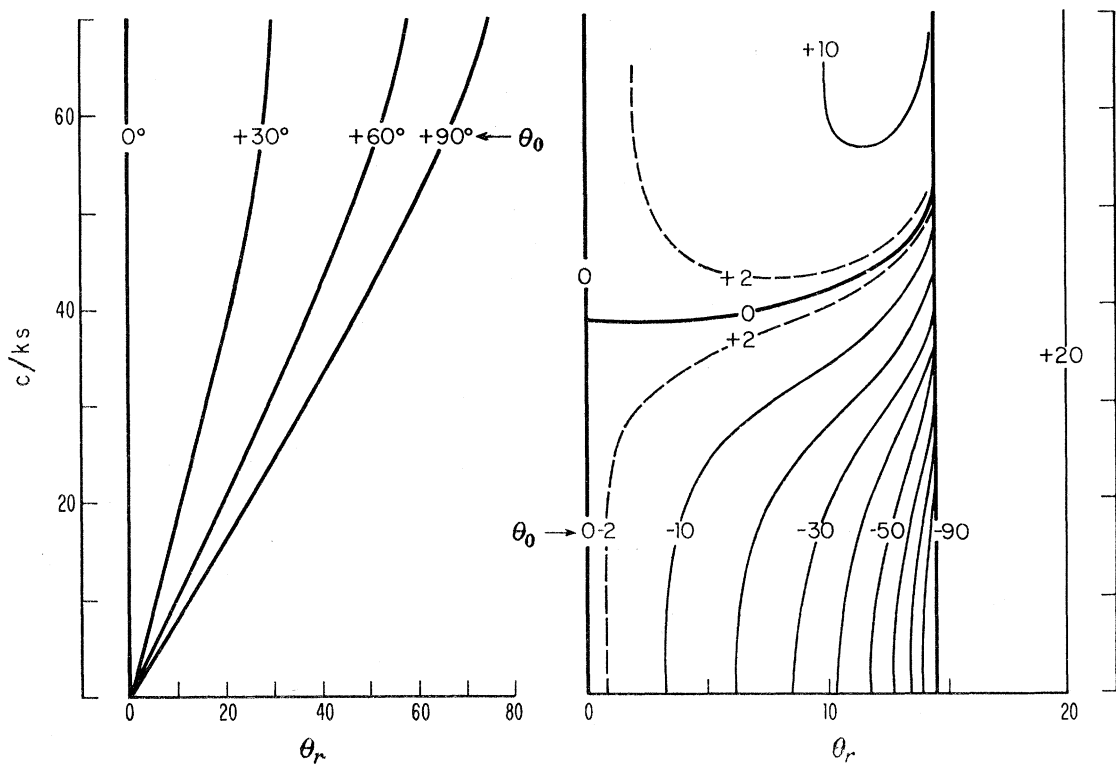


FIGURE 29. *Left:* The recorded direction θ_r (relative to the shore normal) at a depth of 100 m as a function of frequency for various directions in deep water, θ_0 . *Right:* Refraction due to an off-shore shoal. Both graphs are antisymmetric about the frequency axis.

where $C = f/k$ and $V = \delta f/\delta k$ are the phase and group velocities, respectively. The first two terms are obtained from the known frequency and the known depth at the recording station; the 'refraction factor' $\delta\theta_r/\delta\theta_0$ is read off a graph such as figure 27. The method is an improvement over the customary method of measuring the variable separation between wave rays that are parallel in deep water, as has been pointed out by Dorrestein (1960).

For swell from the October hurricane the spectrum on 26 October is peaked at 37.5 c/ks (figure 4). At the recorded depth of 100 m we find

$$\left(\frac{C_r}{C_0}\right) \left(\frac{V_r}{V_0}\right) = (0.68) (1.13) = 0.77.$$

The off-shore direction is 290° ; according to figure 27 the ratio $\delta\theta_0/\delta\theta_r$ is very large and poorly determined. In the case of straight parallel contours the ratio is 2.5 for waves approaching 60° from the shore normal. We conclude that the recorded energy was less than half the off-shore energy. The example is an extreme case of glancing incidence. In most instances the incidence was more nearly normal and accordingly the off-shore energy did not differ by a large factor from the recorded energy. At higher frequencies the two energies are nearly alike.

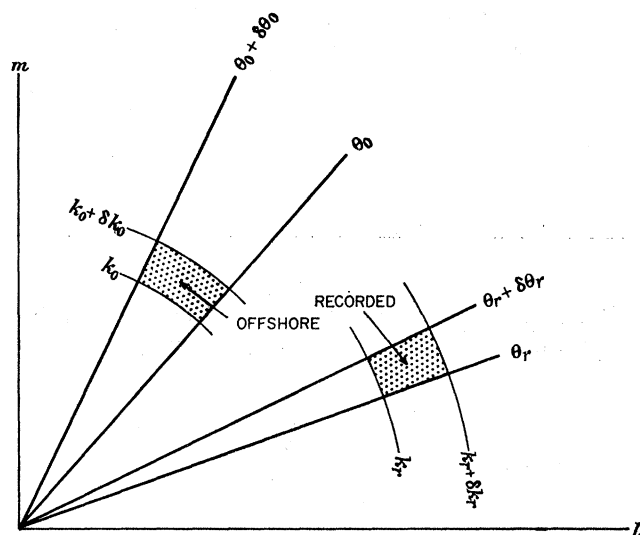


FIGURE 30. An elementary wave train before and after refraction.

10. REFLEXION

The principal reason for the selection of the triangular array was to differentiate between incident and reflected energy. There have been no previous measurements of reflected wave energy. At the frequencies containing most of the wave energy, between 100 and 200 c/ks, say, one expects the breaking of waves to absorb most of the incoming energy. At the very low frequencies one expects effective reflexion; in fact measurements of low-frequency waves on the continental borderland off southern California are consistent with complete reflexion for frequencies below 3 c/ks (Snodgrass, Munk & Miller 1962). The frequencies here under consideration fall between these extremes.

Figures 10 to 12 show the distribution of energy density with direction in the main swell band. In figure 10 nearly all the energy is in the incident wave; on figure 11 there is appreciable energy from shore at 36.3 and 37.5 c/ks. In figure 12 the radiation outside the main beam is fairly isotropic.

Figure 31 shows the reflectivity for 20 and 25 October, 2 days for which the performance of the iterative point-source method was particularly satisfactory (see Discussion §7(e)). The results, which are significant only for swell frequencies (> 30 c/ks), show a drop of reflectivity with frequency. To extend the analysis to frequencies below that of the swell,

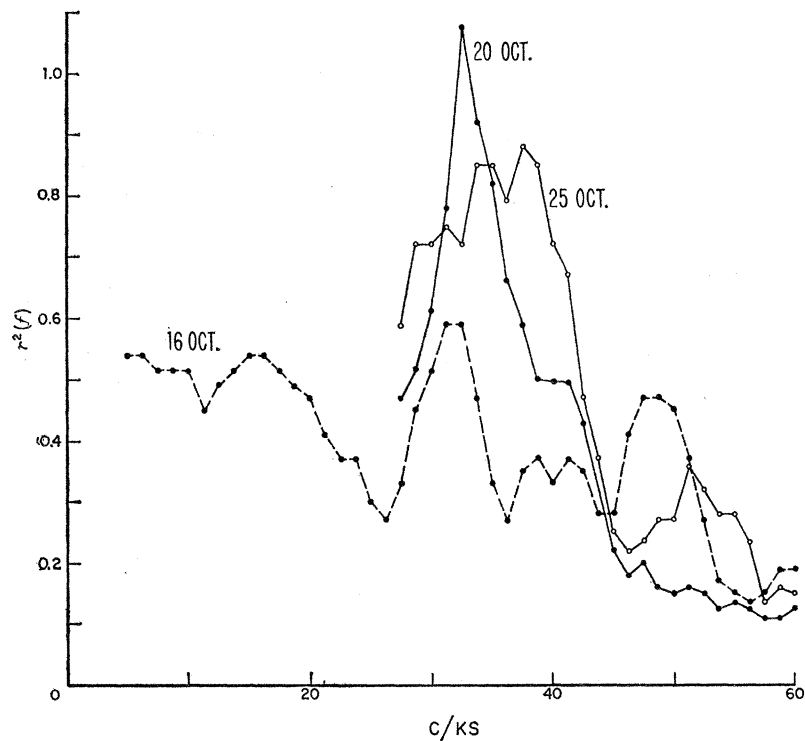


FIGURE 31. The reflectivity, $r^2(f)$, defined as the ratio of energy coming from shore (directions 320° clockwise to 140°) to the energy from off shore (140 to 320°).

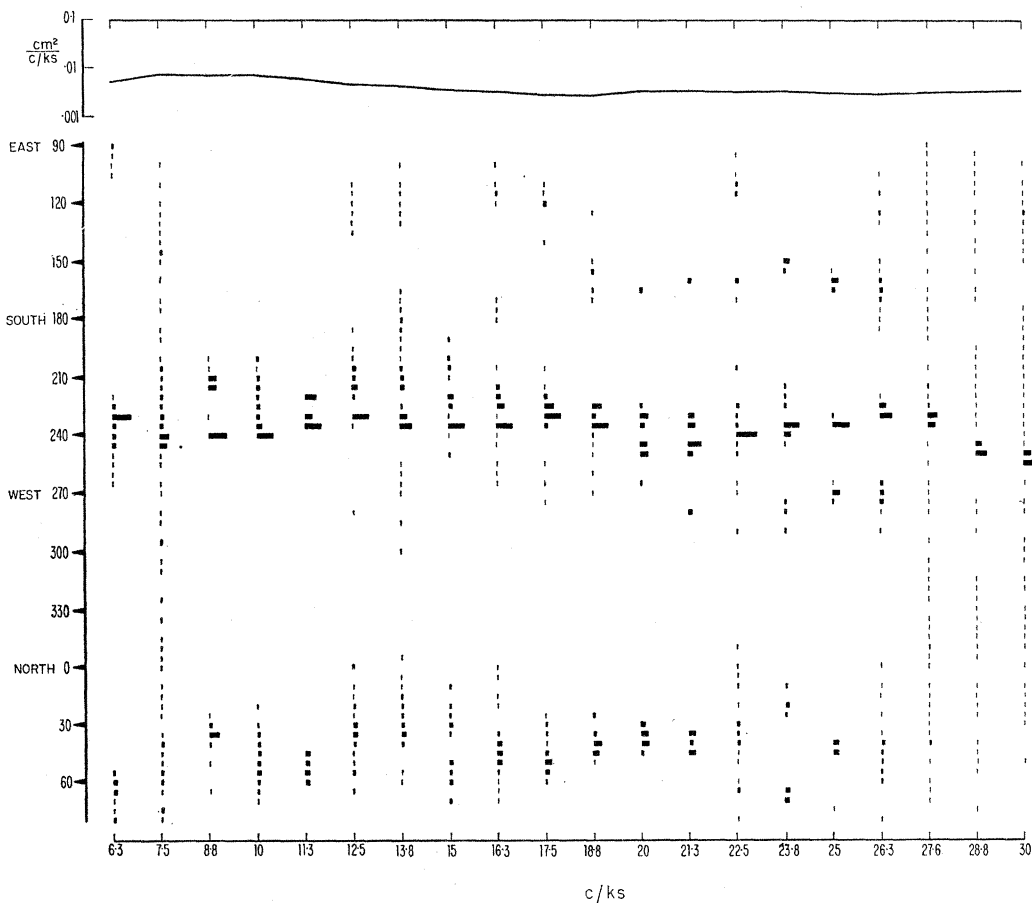


FIGURE 32. The low frequency directional wave spectrum on 16 October 1959 (see legend to figure 10).

we require a record of more than average length. For that purpose we have analyzed the 15 h record of 16 October. Figure 32 shows the directional distribution at these very low frequencies. The striking feature is the concentration of energy along the directions normal to the shore. For the incident wave this concentration is undoubtedly the result of wave refraction (§9). The narrowness of the outgoing beam would suggest that at these very low frequencies the shore-line acts as a specular reflector. But the underlying assumption of our analysis is that the phases of waves from different directions are uncorrelated. Discussion of the spectrum below 25 c/ks requires then special consideration which is not given in this paper. Above 25 c/ks the prominent concentration of energy arriving from 45° is replaced by a general low level isotropic distribution. This is what might be expected as wavelengths become more nearly commensurate with the irregularities in the shore-line.

The results would indicate that the western shore of San Clemente Island (slope 1:30) reflects most of the energy of waves whose frequencies are below 30 c/ks, and absorbs most of the energy above 50 c/ks. The corresponding wavelengths at 100 m depths are 980 m and 522 m respectively, and the characteristic slope spectra are $k^2(f) S(f) = 10^{-11}$ and $10^{-7}/(\text{rad})^2/(\text{c/ks})$ respectively.

11. IDENTIFICATION OF INDIVIDUAL EVENTS

In this section we attempt to identify the storm systems responsible for the significant features of the wave records. The wave information is obtained from the frequency, time-plots of wave energy and direction (figures 13 to 19):

(i) The time or origin, t_0 , is given by the intercept of the ridge lines with the frequency axis (§5(e)).

(ii) The distance, Δ , of the source is determined by the slope of the ridge line (§5(e)). Values of Δ are entered for each ridge line.

(iii) The direction, θ , is inferred from cross-spectral analysis. The October directions are based on the iterated point-source analysis (§7(e)) with the use of three instruments; all other directions follow from the two-instrument method (§5(e)). Estimates of direction are entered for each ridge line, an attempt having been made to allow for refraction (§9).

(iv) The wind speed has been estimated from the energy profile along the ridges (to be discussed in §13). The estimates are not corrected for geometric spreading, and accordingly must be regarded as minimum values.

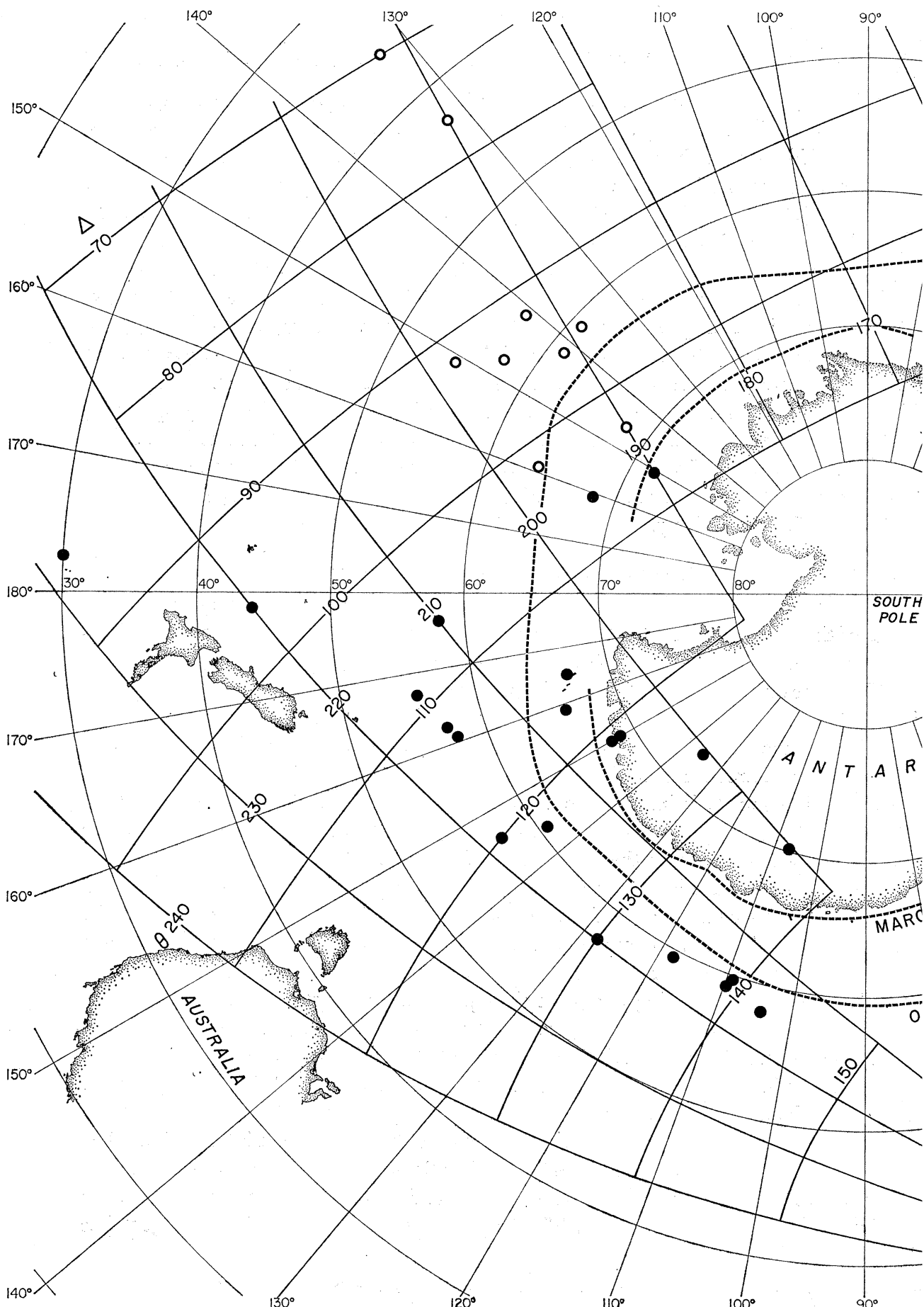
(v) The sharpness of the ridges imposes an upper limit on the storm duration.

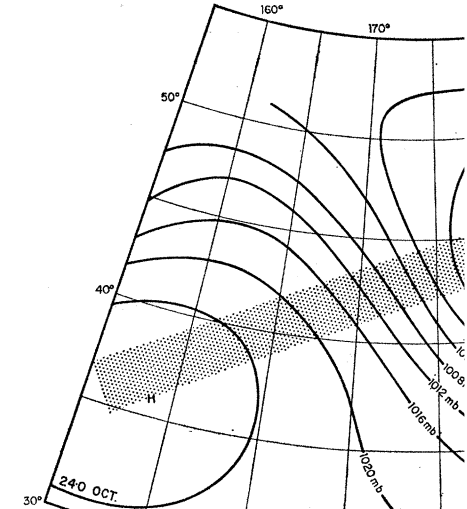
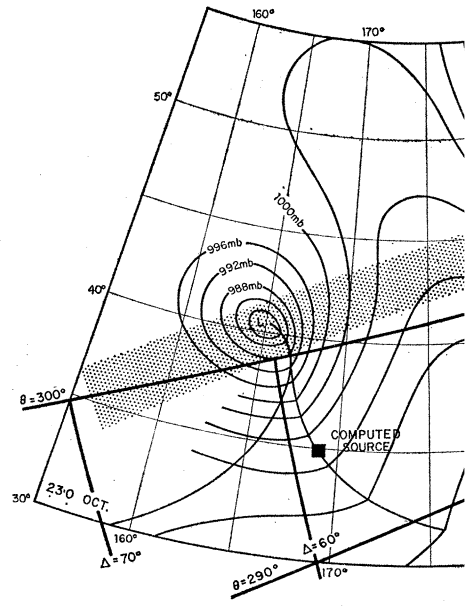
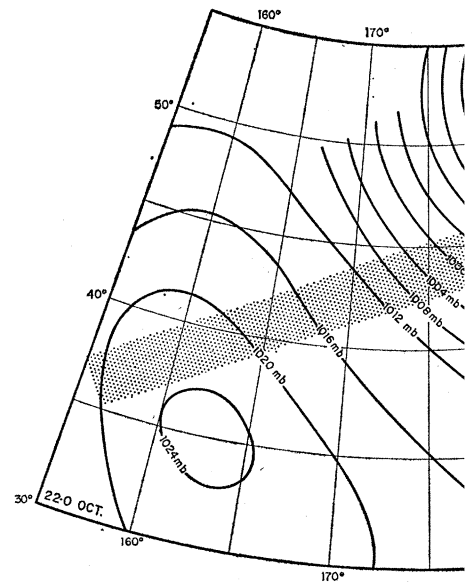
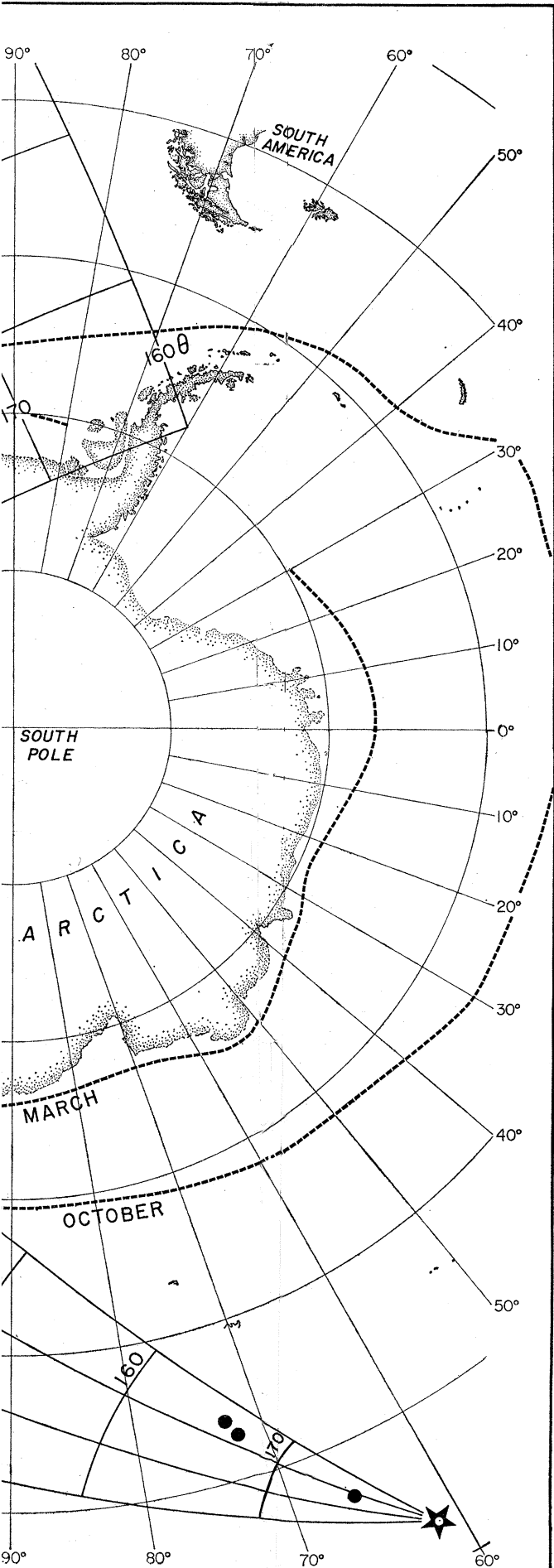
(vi) Under favourable circumstances some information concerning the movement of the storm can be inferred from the variation in wave direction *across* the ridges.

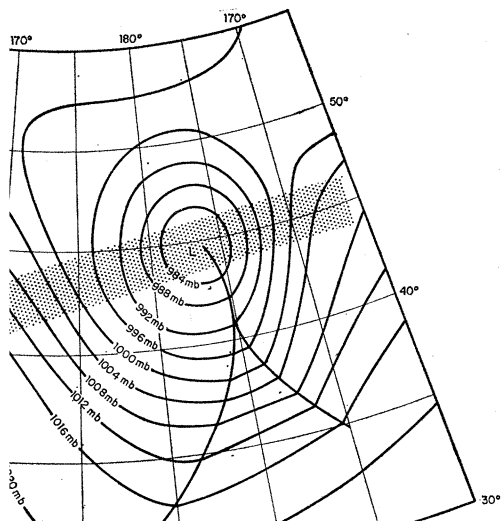
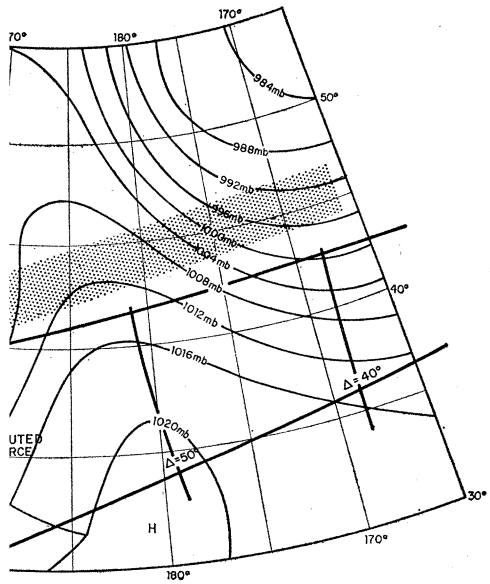
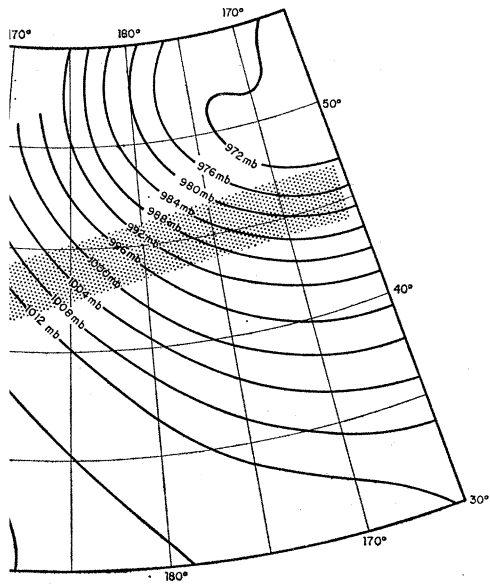
(vii) Attenuation is predominant at frequencies exceeding $f_{\text{cut-off}}$. The cut-off frequency is determined from a comparison of the energy along ridges with generation spectra (§13).

Table 1 summarizes all these parameters together with the pertinent information taken from weather maps.† Figure 33 is a plot of source locations inferred from wave observations. The procedure has been to start with the wave observations and then to search the weather maps for the associated storm system. The only exception is the case of 30·6 August (see below).

† S.O.A. is Southern Ocean Analysis; U.S.W.B.N.H. refers to U.S. Western Bureau Northern Hemisphere Weather Maps; I.A.A.C. refers to analysis by the International Antarctic Circumpolar Weather Center.







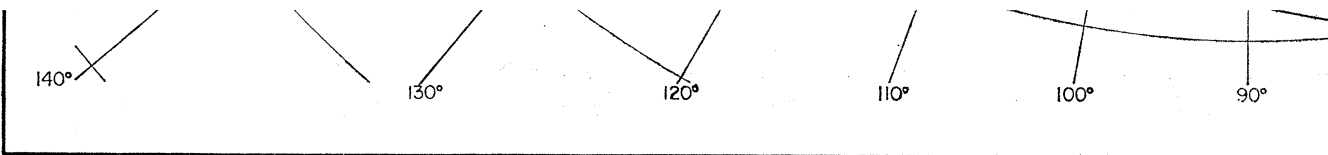
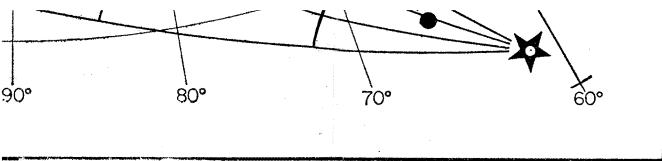


FIGURE 33. The sources as inferred from the wave observations plotted on an Antarctic Azimuthal Equal Area projection. The open circles refer to events for which weather observations were entirely lacking. The diagram includes all observed events except those of 8·9 and 23·2 October, which occurred in the Northern Hemisphere. Great circle routes through San Clemente Island are plotted; they are labelled $\theta = 160^\circ, 170^\circ, \dots$, where θ is the direction *from* San Clemente Island. The curves marked $\Delta = 70, 80, \dots, 180^\circ$ are distance in degrees from San Clemente Island. Average northern limits of pack ice for March and October are shown.



rthal Equidistance
 acking. The chart
 thern Hemisphere.
 70°, ..., 240° giving
 nce in degrees from
 vn.

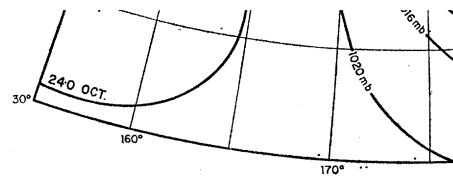
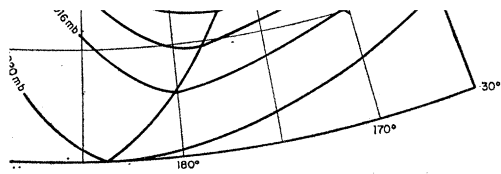


FIGURE 34. Portion of the Northern Hemisphere Weather
 circle routes bearing $\theta = 290$ and 300° from San Cler.
 50, 60, and 70° are indicated The computed source was
 in the central figure. Shaded band indicates path of st



Weather Map of 3 successive days. The great
 an Clemente island, and the distances $\Delta = 40$,
 irce was for 23·2 October at the position shown
 ath of storm.

TABLE 1

based on wave information

U.T. 1959	Δ ($^{\circ}$)	θ ($^{\circ}$)	W (knots)	duration (days)	$\frac{\delta\theta}{\delta f}$ ($\frac{\text{deg}}{\text{c/ks}}$)	$f_{\text{cut-off}}$ (c/ks)	remarks	U.T. 1959
7.4 May	84	228	30	1.0	+1.0	87	only later stages recorded	5 May, S.O.A. 6 May, S.O.A.
9.4 May	92	192	33	0.5	-0.5	79	—	no weather information
11.5 May	96	220	36	0.7	—	59	—	11.25 May, S.O.
12.4 May	113	215	39	0.2	+5.0	63	very sharp ridge	12.25 May, S.O. 12.25 May, S.O. 13.25 May, S.O.
14.1 May	102	197	33	0.8	—	76	—	no weather information
7.0 June	107	190	38	1.0	—	60	only later stages recorded	7.0 June, I.A.A. 7.5 June, I.A.A.
11.8 June	120	218	41	0.7	-1.0	53	gap in data	11.25 June, S.O. 12.0 June, I.A.A.
12.3 June	95	189	35	—	—	72	—	12.25 June, S.O. no weather information
15.1 June	109	215	40	0.8	—	59	—	14.25 June, S.O.
18.4 June	106	195	41	0.6	—	56	—	15.25 June, S.O. 17.0 June, I.A.A.
24.2 June	77	190	39	0.6	—	62	—	no weather information
26.5 June	70	192	39	0.9	—	> 63	—	no weather information
9.0 Aug.	135	217	—	—	—	—	these two events are inadequately resolved on the frequency, time plot, and accordingly Δ and θ are uncertain, and the durations unknown	8.25 Aug., S.O.A. 9.25 Aug., S.O.A.
12.3 Aug.	103	190	32	—	—	+70	—	no weather information
	2	216	34	0.8	—	63	—	12.25 Aug., S.O.
17.1 Aug.	175	223	41	0.7	—	54	usually low background	17.25 Aug., S.O. 18.25 Aug., S.O.
20.3 Aug.	94	195	35	0.7	—	60	$\delta E/\delta f$ on ridge less steep than Darbyshire's; this appears to be the case of a slowly developing storm	no weather observation

TABLE 1 (cont.)

based on wave information

U.T. 1959	Δ ($^{\circ}$)	θ ($^{\circ}$)	W (knots)	duration (days)	$\frac{\delta\theta}{\delta f}$ ($\frac{\text{deg}}{\text{c/ks}}$)	$f_{\text{cut-off}}$ (c/ks)	remarks	U.T. 1959
21.3 Aug.	92	198	34	0.7	—	62	—	no weather observation
21.3 Aug.	107	216	36	1.2	—	62	—	21.25 Aug., S.O.

based on weather maps

1959	Δ ($^{\circ}$)	θ ($^{\circ}$)	W (knots)	remarks
S.O.A.	98	227	—	—
S.O.A.	93	228	—	—
her ation	—	—	—	—
ay, S.O.A.	91	223	—	—
ay, S.O.A.	96	220	—	—
ay, S.O.A.	110	220	—	very short-lived storm south of New Zealand; see §11 (c) and figure 36
ay, S.O.A.	92	212	—	—
ner ation	—	—	—	—
, I.A.A.C.	109	190	—	fetch associated with LOW at 75° S, 150° W, poorly documented; on 8·5 June fetch over Antarctica
, I.A.A.C.	109	190	—	moved to right as expected
ne, S.O.A.	113	220	—	—
ne, I.A.A.C.	110	222	—	—
ne, S.O.A.	120	230	—	—
her ation	—	—	—	—
ne, S.O.A.	111	218	—	unusually long (1500 n.m.) well directed fetch
ne, S.O.A.	110	215	—	two LOWS with favourable 1200 n.m. fetch
e, I.A.A.C.	92-110	198	—	—
her ation	—	—	—	—
her ation	—	—	—	—
g., S.O.A.	133	225	weak	970 mb LOW
g., S.O.A.	118	225	25	—
her ation	—	—	—	—
g., S.O.A.	145	222	—	965 mb LOW, 600 n.m. of favourable fetch. Lasts for 3 days, very station- ary
g., S.O.A.	155	210	35	winds of favourable direction between 965 mb LOW and 1035 mb HIGH; on following day direction much less favourable
g., S.O.A.	170	220	—	—
ner ation	—	—	—	—

based on weather maps

1959	Δ ($^{\circ}$)	θ ($^{\circ}$)	W (knots)	remarks
ner ation	—	—	—	—
g., S.O.A.	165	221	35	strongest development at

554 W. H. MUNK, G. R. MILLER, F. E. SNODGRASS AND N. F. BARBER

DIRI

U.T. 1959	(°)	(°)	(knots)	(days)	(c/ks)	(c/ks)	remarks	
21.3 Aug.	92	198	34	0.7	—	62	—	no weather observation
21.6 Aug.	167	216	36 31	1.2	—	62 > 80	— secondary hump	21.25 Aug., S.O.
24.3 Aug.	122	215	41	0.9	—	50	—	23.25 Aug., S.O.
28.7 Aug.	106	210	36	0.7	—	70	small $\delta E/\delta f$ on ridge high background before and after ridge	24.25 Aug., S.O.
30.6 Aug.	166	216	43	—	—	52		28.25 Aug., S.O.
30.8 Aug.	117	207	42	1.0	—	57	—	30.25 Aug., S.O.
1.4 Sept.	121	206	41	1.0	—	53	—	31.25 Aug., S.O.
4.5 Sept.	135	200	40	1.0	—	58	—	1.25 Sept., S.O.
8.7 Sept.	115	205	41	0.9	—	54	—	1.25 Sept., S.O.
11.6 Sept.	126	200	40	0.8	—	60	—	4.25 Sept., S.O.
14.2 Sept.	121	205	40	0.7	—	49	—	8.4 Sept., S.O.A.
25.3 Sept.	139	215	35	0.7	—	63	—	10.25 Sept., S.O.
								11.25 Sept., S.O.
								14.25 Sept., S.O.
								24.25 Sept., S.O.
								25.25 Sept., S.O.
27.7 Sept.	130	220	45	0.9	—	44	—	28.25 Sept., S.O.
8.4 Oct.	139	215	44	0.7	—	57	—	7.25 Oct., S.O.A.
8.9 Oct.	67	295	40	1.0	—	61	severely refracted	8.25 Oct., S.O.A.
18.7 Oct.	96	191	42	0.6	—	63	—	9.25 Oct., S.O.A.
21.5 Oct.	112	215	—	1.4	—	—	—	10.25 Oct., S.O.
								10.0 Oct., U.S.W.B.N.H.
								no weather information
								21.25 Oct., S.O.
								22.25 Oct., S.O.
23.2 Oct.	59	295	48	1.0	—	50	see § 11 (a) regarding direction	23.0 Oct., U.S.W.B.N.H.
								24.0 Oct., U.S.W.B.N.H.

	(°)	(°)	(knots)	remarks
ber tion g., S.O.A.	165	221	35	strongest development at 21·25, duration 20·25 to 22·25; favourable winds beyond fetch (see figure 35)
g., S.O.A.	120	216	30	—
g., S.O.A.	114	215	35	—
g., S.O.A.	110	215	—	—
g., S.O.A.	158	215	40	—
g., S.O.A.	145	220	—	—
g., S.O.A.	118	214	—	—
g., S.O.A.	115	205	—	—
t., S.O.A.	115	200	—	two storm areas
t., S.O.A.	124	215	—	—
t., S.O.A.	135	214	—	—
, S.O.A.	115	213	—	—
pt., S.O.A.	128	214	—	—
pt., S.O.A.	120	215	—	—
pt., S.O.A.	121	217	—	—
pt., S.O.A.	143	217	20	storm moved rapidly towards east, reached maximum between 24·25 to 25·25 Sept.; almost gone by 26·25 Sept.
pt., S.O.A.	126	217	40	moved from $\Delta = 142^\circ$, $\theta = 223^\circ$ on preceding day, when it was weak and ill-defined; weakened on 29th and strengthened on 30th.
pt., S.O.A.	120	230	—	955 mb Low, with intense winds from 7·25 to 9·25 Oct.
t., S.O.A.	135	215	—	—
t., S.O.A.	138	220	—	—
t., S.O.A.	131	220	—	—
ct., S.O.A.	120	218	—	—
t., B.N.H.	55	295	30	slowly moves eastward into gulf of Alaska
her ation	—	—	—	—
ct., S.O.A.	110	215	35	960 mb Low; favourable fetch
ct., S.O.A.	108	215	35	960 mb Low; less favourable wind direction
t., B.N.H.	60	300	55	storm approaching at 35 knots along line of
t., B.N.H.	53	300	—	site (see figure 34).

There are three main source areas: the Ross Sea, the New Zealand–Australia–Antarctic sector, and the antipodal region. No sources east of the Ross Sea were found, but these would be discriminated against by refraction. For most sources off the Ross Sea the weather information was entirely inadequate to check the wave observations. In all other instances it has been possible to associate the wave-inferred sources with observed storms. Often the weather information is so sparse and the location of storm centres so indefinite that the comparison is not convincing. The weather maps show storms at least as intense as those yielding a ridge line, yet not being associated with a well-defined feature on the $E(f, t)$ diagrams. Major ridge lines stand out more impressively above the spectral background than do the associated storms stand out above the run-of-the-mill storm. Perhaps this is a reflexion of the fact that the power absorbed in the waves is proportional to a high moment of the wind speed, presumably the fourth moment. It might also indicate that very high winds are concentrated in space and time, and are likely to be missed in a loose observational grid. In some sense the wave observations may yield a more reliable though biased indication of the storm system than the weather observations themselves.

Two wave-inferred sources are on land: 4.5 and 11.6 of September. The computed directions are 200° , whereas the nearest storm systems would indicate directions of 210 to 215° . The distances agree. In many other instances the storms lie to the west of the inferred sources.

We now consider some individual cases.

(a) *The hurricane of 23 October*

According to figure 17 the time of origin was early on 23 October 1959 (u.t.) and the distance 59° . The direction is best estimated from figure 23. The well-defined peaks at 47.5 and 58.6 c/ks suggest an off-shore direction between 290 and 300° . At 35 c/ks the directional histogram is split in three parts. At 25 c/ks, the lowest recorded frequency, the refractive effects are so dominant that little can be inferred concerning off-shore direction, but as far as the evidence goes it is consistent with the foregoing estimate. With regard to wave direction the present example is not typical because of the extreme refraction.

We set

$$t_0 = 23.2 \text{ August}, \quad \Delta = 59^\circ, \quad \theta_0 = 295^\circ,$$

as our estimate based on the wave records. Copies of weather maps in the critical area are plotted on figure 34. A hurricane with 55 knot winds appears on the map of 23 October. There is no indication of this storm on the preceding day. On 24 October the storm has moved east and the winds are somewhat weaker. By 25 October the storm had weakened considerably. Our estimates from weather maps are

$$t_0 = 23 \text{ August}, \quad \Delta = 60^\circ, \quad \theta_0 = 300^\circ,$$

and these are in fair agreement with the parameters deduced from the wave records.

The observed duration is roughly in accord with the wave observations. The effect of the rapid approach along the line of site is to steepen and sharpen the ridge at a frequency f whose group velocity $V(f)$ equals the velocity of approach. This is discussed in more detail in connexion with the rapidly moving source of 12.4 May (see §11(c), figure 36). The velocity of approach is 35 knots, and the expected focus is at 49 c/ks. This is in accord with the ridge contours.

Figure 19 shows the directional histogram at 37 c/ks. The arrival of the hurricane swell leads to an interruption on 26 and 27 October of what was otherwise a predominant radiation from the south. Similar effect can be noted at higher frequencies (figures 20 and 21).

(b) *Antipodal swell*

Three ridge lines on figure 15 have an inclination markedly below average. The earliest arrivals had been under way for nearly 2 weeks before they were recorded at San Clemente Island. The inferred distances to the source come close to 180° .

At first glance the detection of an antipodal swell appears to be most unlikely; however, the convergence of longitudinal lines between opposite points on a globe leads to focusing at the antipole, so that the chance for receiving a signal from 180° is better than from 90° , other factors remaining equal.

The Pacific Ocean is too small for antipodal generation, the furthest distance from San Clemente Island being of the order of 110° . But there are two 'windows' into the Indian Ocean. One is between Australia and New Zealand through the Tasman Sea, subtending the directions 230 to 234° (figure 49). The other is south of New Zealand, between 206 and 225° . But the Tongan Islands interfere with directions north of 232° ; the Taumotu and Society Islands with directions east of 216° (§ 15). The south New Zealand window is limited also by Antarctic pack ice. If we discard directions from which more than half the sector is blocked by South Pacific islands, all that is left of the two windows is 230 to 232° , and 215 to 225° . The more likely path is then just south of New Zealand. This places the source area north of Kerguelen Island between the 'roaring forties' and 'fighting fifties' into the stormiest latitude belt on earth.

The parameters associated with the three antipodal arrivals are as follows:

t_0	Δ	θ_0
17.1 August	175°	223°
21.6 August	167°	216°
30.6 August	166°	216°

The third event is barely above background. The waves come from a direction nearly normal to shore with a minimum of refraction, and the directions are well determined. It is reassuring that they fall into the narrow permissible range 216 to 225° just south of New Zealand.

In our initial analysis of the wave records, only the ridge lines for the events of 17.1 and 21.6 August had been drawn. An enquiry concerning the observed surface winds at Kerguelen Island led to the result† that 17 August and 21 August 1959, were indeed days of exceptionally high westerly winds. On both days wind speeds up to force 7 were recorded. But the biggest storm of the month occurred on 29–30 August, with winds up to force 8 being recorded. We then re-examined our spectra and found that a peak on 11 September and an indication of a peak on 10 September were consistent with a source on 30.6 August. The residual background from the event of 1.4 September was so high that the energy in these peaks was actually larger than that associated with the events of 17.1 and 21.6 August. There is no question concerning the reality of the spectral features of 10 and 11 September,

† We are indebted to Mr G. de Q. Robin, Director of the Scott Polar Research Institute, for furnishing this information.

but it should be understood that the associated ridge line was drawn on hindsight. (All other ridge lines in this investigation were drawn without reference to weather maps.)

An examination of daily weather maps (0600 U.T.) provided by the Southern Ocean Analysis led to the following parameters:

t_0	Δ	θ_0
17·25 August	155 to 170°	210 to 220°
21·25 August	165°	221°
30·25 August	158°	215°

The agreement with the wave records is as close as one has any right to expect.

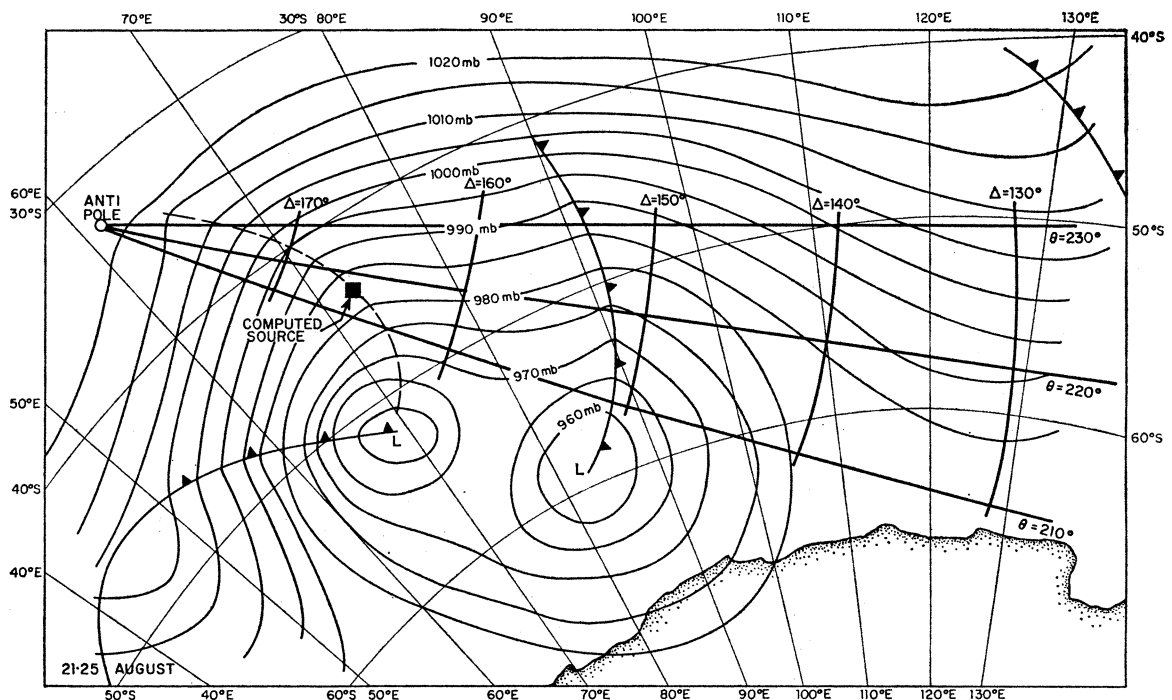


FIGURE 35. Portion of the Southern Ocean Analysis for 0600 G.C.T., 21 August 1951. The great circle routes bearing $\theta = 210, 220$ and 230° from San Clemente Island, and the distances $\Delta = 130, 140, \dots, 180^\circ$ are indicated. The computed source was for 21·6 August at the indicated position.

The widths of the ridges (between half-power contours) for 17·25 and 21·25 August are found to be 0·7 and 1·2 days, respectively. This is in rough accord with what can be inferred from the weather maps. For the case of 17·25 August winds of favourable direction lasted for one day only. In the case of 21·25 August favourable winds lasted from 20·25 to 22·25 August. The weather map for 21·25 August is shown in figure 35.

(c) *The quickly moving storm of 12·4 May*

The source of 12·4 May is exceptional in three ways: it is associated with the narrowest of all observed ridges, and with the largest directional gradient across the ridge (see figure 13). The weather maps show an intense low-pressure area that moves unusually rapidly towards the north-east (figure 36). The agreement between observed and computed positions of the source is fair.

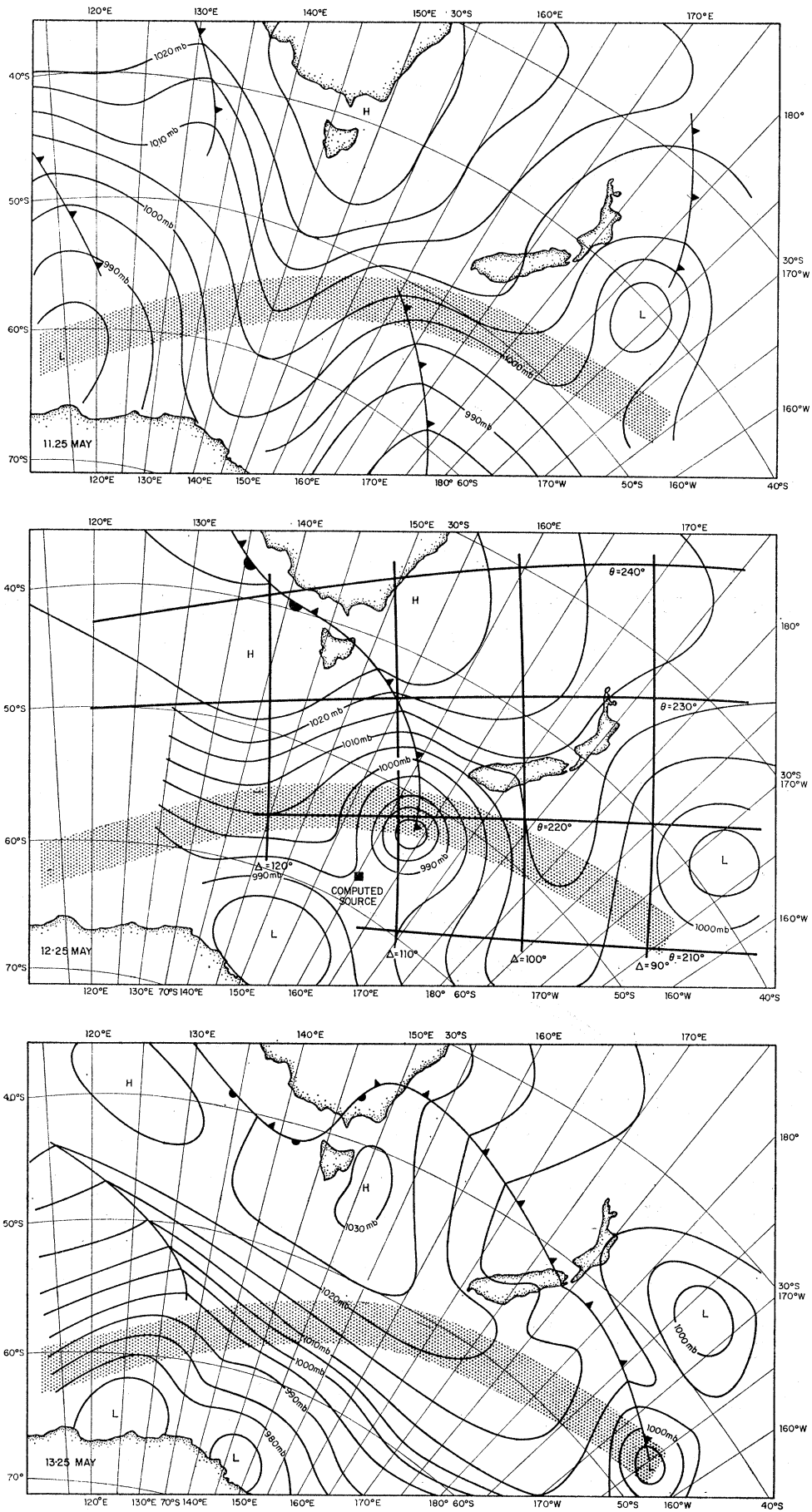


FIGURE 36. Portion of the Southern Ocean Analysis for 0600 u.t., 11, 12 and 13 May. The great circle routes bearing $\theta = 210, 220, 230, 240^\circ$ from San Clemente Island, and the distances $\Delta = 90, 100, 110, 120^\circ$ are indicated. The computed source was for 12.4 May at the position shown in the central figure. Shaded band indicates path of storm.

We suggest that the three observed features, the narrowness of the ridge, the directional gradient, and the speed of the storm are related. For an approaching storm one frequency is amplified over all others: the frequency whose group velocity equals the rate at which the storm approaches. The amplification is particularly pronounced if the storm approaches at a constant rate. The existence of such a 'group velocity peak' has been noted by Eckart (1953) for waves generated by a moving gust, and is implicit in his equation (35). Munk & Snodgrass (1957) have discussed this effect as applied to a source moving at constant speed along some fixed latitude.

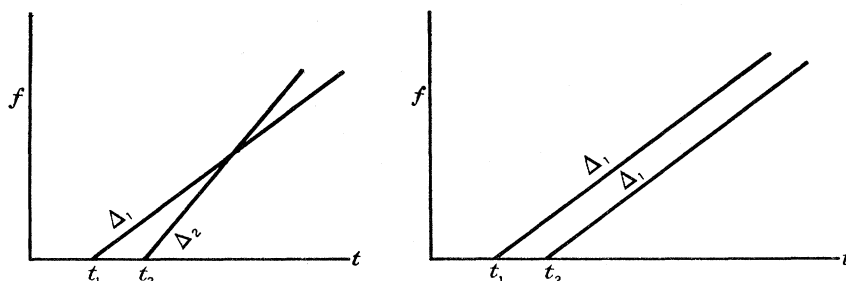


FIGURE 37. The f - t diagram for a stationary source (right) and a source approaching the station with a speed $(\Delta_1 - \Delta_2)/(t_2 - t_1)$ (left).

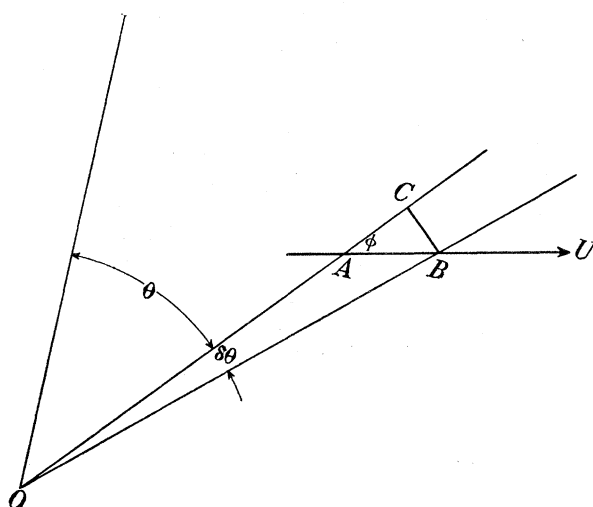


FIGURE 38. Variations in the recorded wave direction and distance resulting from a movement of the source with a speed U in a direction ϕ .

Consider a storm generating waves in a time interval t_1 to t_2 (figure 37). If it remained at a fixed distance, Δ_1 , from the wave station (but not necessarily in a fixed direction), then the recorded duration is t_2 to t_1 and the directional gradient is independent of frequency. But if the storm approaches the station at some velocity, U , then the waves are 'focused' at that particular frequency f for which $V(f) = U$.

Near the focus waves from different directions have nearly the same frequency, and accordingly $\delta\theta/\delta f$ is very large. Consider a source moving at a velocity U in a direction ϕ relative to the line of sight (figure 38). Then in a time δt , the direction and distance of the source vary by an amount

$$\delta\theta = \frac{CB}{OA} = \frac{U\delta t \sin\phi}{\Delta}, \quad \delta\Delta = AC = U\delta t \cos\phi.$$

Let t be the time of the wave observation relative to the time of the source. Then

$$\frac{\Delta}{t} = V(f) = \frac{g}{4\pi f}, \quad \frac{\Delta + \delta\Delta}{t - \delta t} = \frac{g}{4\pi(f + \delta f)},$$

so that

$$\frac{\delta\Delta}{\Delta} + \frac{\delta t}{t} = -\frac{\delta f}{f}.$$

It follows that

$$f \frac{\delta\theta}{\delta f} = -\frac{U \sin \phi}{V(f) + U \cos \phi}. \quad (11.1)$$

The quantity $\delta\theta/\delta f$ is evaluated for a fixed time of observation, i.e. vertically across the ridge in the f - t diagrams. For the particular frequency for which the storm approached the station at group velocity, the denominator vanishes and $\delta\theta/\delta f$ becomes infinite.

According to the weather maps the storm approached at a rate of about 18° per day. The sharpness of the ridge and the directional gradients are at a maximum near 50 c/ks, corresponding to 13° per day. If we set $U \cos \phi = -13^\circ$ per day, we find

f (c/ks)	40	46	52	56	62
$V(f)$ (deg/day)	17.2	15.0	13.2	12.3	11.1
$U \cos \phi$ (deg/day)	-13	-13	-13	-13	-13
$V(f) + U \cos \phi$ (deg/day)	4.2	2.0	0.2	-0.7	-1.9
$\cot \phi (\delta\theta/\delta f)$ (deg/day)	0.08	0.14	1.25	-0.33	-0.11

according to equation (11.1). This yields large positive values of $\cot \phi \delta\theta/\delta f$ at 52 c/ks, and for a reasonable choice of ϕ the numerical value of $\delta\theta/\delta f$ can be made to agree with the observed. At lower frequencies $\cot \phi \delta\theta/\delta f$ is small and positive, at high frequencies small and negative. Observations are not in disagreement with this calculation, and we may conclude that sharp directional gradients across a ridge at some frequency f are an indication of the approach of the source with a speed $V(f)$.

(d) *The end of the storm season*

In October the winter season in the southern hemisphere comes to an end, and the northern hemisphere takes over as the chief region of wave generation. From weather maps we find that the three most intense southern storms during the period were those of 8, 13 and 21 October; the corresponding minimal pressures are 955, 950 and 955 mb respectively. The events of 8 and 21 October are in good agreement with the wave observations, but there is no evidence of waves from the storm of 13 October. With regard to the northern source of 8.9 October, weather maps indicate a later and nearer source. For this case the $E(f, t)$ contours are not too well defined and could have been drawn consistent with a later and nearer source.

(e) *Narrow beams and sharp ridges*

In general it is found that sharp ridges are associated with narrow directional beams. But this need not be the case. On 16 October, for example, we find a narrow beam (directions in bold italics) off the ridge (figure 18). The direction lies within a few degrees of 200° in the frequency range 48 to 52 c/ks, and is remarkably consistent on subsequent analyses. On 22 to 26 October (figure 17) we find a narrow beam of uniform radiation from 285° centred at 70 c/ks, probably associated with the San Nicolas Island cut-off (figure 52).

Narrow beams off the main ridges are probably the result of steady radiation through a narrow window, or radiation from a stationary compact storm. Sources that are both of short duration and of small dimension are associated with sharp ridges *and* narrow beams.

(f) *A discrepancy in wave direction?*

There is a curious indication that the wave-inferred directions are to the left of the location obtained from weather maps. The rotation of the earth will deflect the waves in the sense indicated here, but the computed effect is too small by two orders of magnitude (Backus 1962). The directions inferred from the lower frequencies are in better accord with the observed directions. It appears as if the direction on the ridges at high frequencies is influenced by a southerly background to both sides of the ridge. For narrow, weak ridges the resolution was certainly not adequate to shield the ridge calculations from the effects of sidebands. This can be documented by the event of 8·4 October, when late arrivals were swamped by a westerly background. The early arrivals, up to 19 October, are high above background, and the wave direction (corrected for refraction) is well determined at about 215° . On 20 October the ridge direction is still near 215° , but some westerly energies are already apparent on the $E(f, \theta)$ diagram. On 21 October the radiation from 215° is still noticeable but the primary radiation on the ridge as well as to the sides is now from 280° . If the analysis had been for a single point source (as in the case of the earlier records) one would have inferred a more westerly direction than is actually the case.

If measurements were to be repeated, the question of wave refraction should be given more careful consideration. Plots of recorded direction against frequency for various directions off-shore (such as figure 29) should be plotted, and the measured values $\theta(f)$ along the ridges superimposed for the best choice of deep-sea direction. Preferably a location without off-shore bars should be selected. A comparison with meteorological events in the southern oceans would be far more meaningful if such observations could be made at a time when a weather satellite is in suitable orbit.

12. AN EXPERIMENT IN HETERODYNING

In the previous section we have remarked upon the remarkable sharpness of some of the spectral peaks. In some instances the widths cannot even be determined because the peaks are seriously blurred by the dispersive shift in frequency that occurs during a 3 h record. A much shorter record is inappropriate because then the peak is drowned in the statistical uncertainties of the spectral estimates.

(a) *Removal of frequency shift*

But this uncertainty concerning sharp dispersive peaks is not of a fundamental nature. Suppose we consider a signal

$$\eta(t) = \cos 2\pi ft, \quad f = a + bt,$$

whose frequency increases linearly with time and at a rate sufficiently slow such that the fractional increase in a wave period, f^{-1} , is very small:

$$\left(\frac{1}{f} \frac{df}{dt}\right) f^{-1} = b/a^2 \ll 1.$$

$$\text{Let } c(t) = \eta(t) \cos 2\pi f_0 t, \quad s(t) = \eta(t) \sin 2\pi f_0 t,$$

$$f_0 = a_0 + b_0 t.$$

If we choose the 'heterodyning frequency' f_0 close to f and increasing at approximately the same rate as f , that is, $a \approx a_0$ and $b \approx b_0$, then $a(t)$ and $b(t)$ contain terms $f - f_0$ and $f + f_0$; the latter are removed by smoothing, and we are left with a difference tone that is not blurred by dispersion.

The method has been applied to the very narrow peak of 12.4 May and to the event of 8.4 October which was continuously recorded for nearly a day (figure 19). Values of a_0 and b_0 are then chosen to give $f_0(t)$ along the ridge. Let $\bar{c}(t)$, $\bar{s}(t)$ be smoothed versions of $c(t)$, $s(t)$; more precisely, frequencies in excess of the *width* of the spectral peak are removed. It will be shown that the spectral distribution of the record $x(t)$ relative to the sliding peak frequency $f_0(t)$ is given by

$$S_{\eta\eta}(f_0 \pm \alpha) = 2S_{\bar{c}\bar{c}}(\alpha) \pm 2Q_{\bar{c}\bar{s}}(\alpha), \quad (12.1)$$

where $S_{\bar{c}\bar{c}}$ is the spectrum of $\bar{c}(t)$ and $Q_{\bar{c}\bar{s}}$ the quadrature spectrum between $\bar{c}(t)$ and $\bar{s}(t)$.

(b) Heterodyne theory

Consider the correlation

$$\begin{aligned} \rho_{\bar{c}\bar{c}}(T) &= \langle \eta(t) \eta(t-T) \cos 2\pi f_0 T \cos 2\pi f_0 (t-T) \rangle, \\ &\approx \frac{1}{2} \langle \eta(t) \eta(t-T) \rangle \cos 2\pi f_0 T \\ &= \frac{1}{2} \rho_{\eta\eta}(T) \cos 2\pi f_0 T, \end{aligned}$$

where the approximation refers to the smoothing of $c(t)$. Similarly $\rho_{\bar{s}\bar{s}}(T) = \rho_{\bar{c}\bar{c}}(T)$ and

$$\begin{aligned} \rho_{\bar{c}\bar{s}}(T) &= \langle \eta(t) \eta(t-T) \cos 2\pi f_0 t \sin 2\pi f_0 (t-T) \rangle \\ &\approx \frac{1}{2} \rho_{\eta\eta}(T) \sin 2\pi f_0 T. \end{aligned}$$

The Fourier transforms of the autocorrelations $\rho_{\bar{c}\bar{c}}(T)$ or $\rho_{\bar{s}\bar{s}}(T)$ give the spectra

$$\begin{aligned} S_{\bar{c}\bar{c}}(\alpha) &= 2 \int_{-\infty}^{\infty} \rho_{\bar{c}\bar{c}}(T) \cos 2\pi \alpha T \, dT \\ &= 2 \int_{-\infty}^{\infty} \frac{1}{2} \rho_{\eta\eta}(T) \cos 2\pi f_0 T \cos 2\pi \alpha T \, dT \\ &= \frac{1}{2} \int_{-\infty}^{\infty} \rho_{\eta\eta}(T) [\cos 2\pi(f_0 + \alpha) T + \cos 2\pi(f_0 - \alpha) T] \, dT \\ &= \frac{1}{4} [S_{\eta\eta}(f_0 + \alpha) + S_{\eta\eta}(f_0 - \alpha)], \end{aligned} \quad (12.2)$$

and similarly

$$C_{\bar{c}\bar{s}}(\alpha) = 2 \int_{-\infty}^{\infty} \rho_{\bar{c}\bar{s}}(T) \cos 2\pi \alpha T \, dT = 0,$$

$$\begin{aligned} Q_{\bar{c}\bar{s}}(\alpha) &= 2 \int_{-\infty}^{\infty} \rho_{\bar{c}\bar{s}}(T) \sin 2\pi \alpha T \, dT \\ &= \frac{1}{4} [S_{\eta\eta}(f_0 + \alpha) - S_{\eta\eta}(f_0 - \alpha)]. \end{aligned} \quad (12.3)$$

Equation (12.1) follows from (12.2) and (12.3). We note that the two spectra should be equal and the co-spectrum should vanish, subject of course to the usual statistical fluctuations.

(c) *The results*

Figure 39 shows two successive spectra for the event of 16 October. The essential parameters are

centre time	duration	sample points	degrees of freedom
1710 U.T., 16 October	9.8 h	8820	7
0425 U.T., 17 October	4.8 h	4350	3.5

The resolution is now 0.1 c/ks (as compared to 1.25 c/ks in the standard analyses), and the statistical uncertainty is very great. The central peak has an effective width of perhaps ± 0.2 c/ks, and a corresponding Q of the order of 200. We have now carried the analysis to

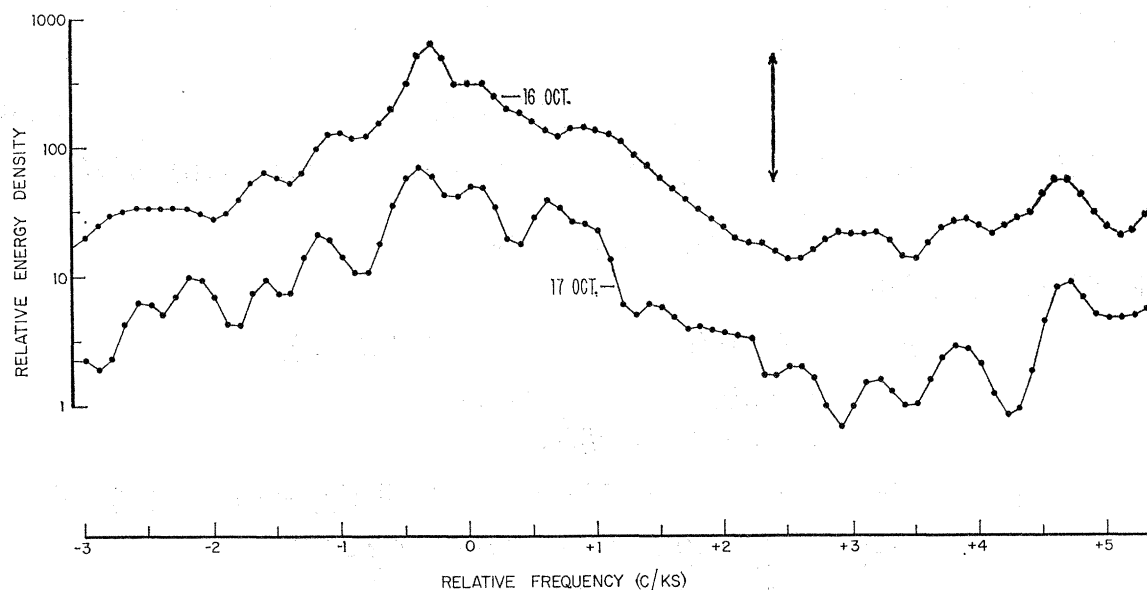


FIGURE 39. The spectrum of the peak associated with the event of 8.4 October relative to the (sliding) central frequency. Energy densities are on a relative logarithmic scale uncorrected for bottom depth. The vertical arrow gives the 95% uncertainty limits pertaining to the spectrum of 16 October.

(or perhaps beyond) its ultimate resolution, limited not by dispersion but by the stationarity of the meteorologic sources.

Some of the fine structure appears to be reproducible between the two records, and to shift slightly relative to the central frequency, thus indicating differences of the sources in space-time. From the Q of the peaks we infer durations of the order of 1% of the travel time, and fetches of 1% of the travel distance. We may then be detecting the effects of squalls within the storm, characterized by durations of several hours and fetches of perhaps a hundred miles. All of these conclusions are uncertain.

Barber & Ursell (1948) were able to detect a 12 h modulation in the frequency of the central peak, and they could attribute this to the effect of the known strong tidal currents in the vicinity of the Pendeen station. The tidal currents off San Clemente Island are much weaker and the effect correspondingly smaller; still we hoped the tidal modulation might be detected by using the fine structure of the heterodyned peaks. This would provide an amusing example of f.m.—f.m.—f.m.: the tides (10^{-5} c/s) modulate the swell (10^{-1} c/s) which in

turn modulates the vibration transducer (10^4 c/s) whose output modulates the radio transmitter (10^8 c/s). An analysis of successive 3 h records failed to show such an effect. This provides an upper limit on the velocity of the near-shore tidal currents. A tidal frequency modulation above one part in 300 could have been detected. The tidal currents are then less than $1/300$ of the phase velocity, or less than $\frac{1}{4}$ knot.

13. GENERATION AND DECAY

(a) Ridge cuts

Figure 40 shows the variation in energy density with frequency along some of the ridges in the f - t diagrams. The significance of the 'ridge cut' is that the effect of dispersion is removed, so that we can infer the spectrum in the source area as modified by attenuation along the path.

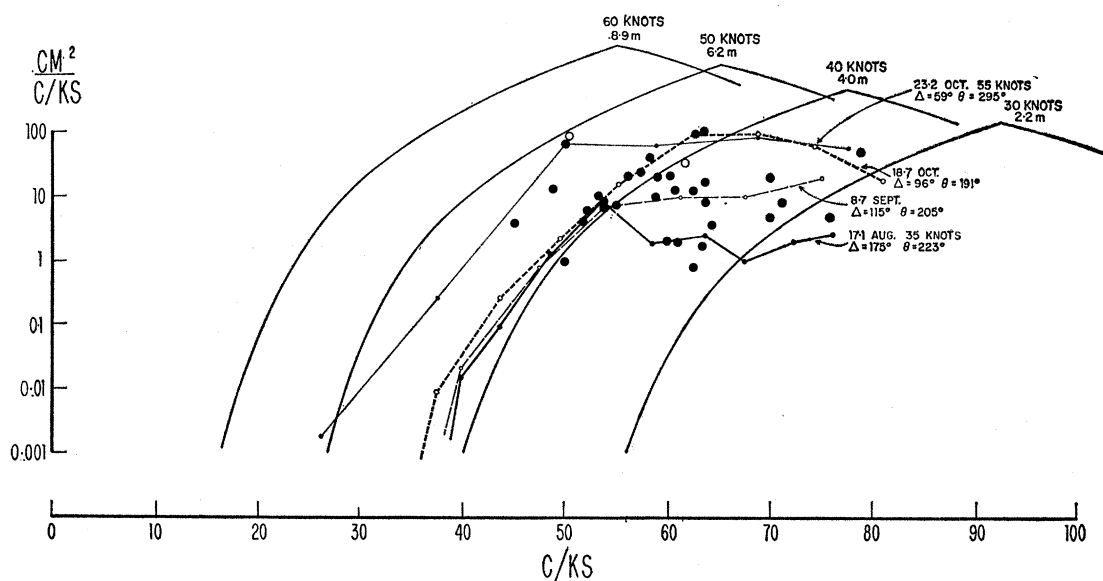


FIGURE 40. The curves marked 30, 40, 50, 60 knots are Darbyshire's empirical spectra in the generation area. The associated root-mean-square heights (crest-to-trough) are entered. For comparison, the variation of energy density with frequency along four well-developed ridges is shown; time, distance and direction, as entered, are those determined from the wave observations. The wind speed in knots is taken from the weather maps. The dots mark the 'cut-off points': to the left the measured $E(f)$ values are in reasonable accord with the empirical curves, to the right they fall below the empirical curves, presumably because of attenuation. The open circles refer to the northern sources of 8.9 and 23.2 October, the remaining circles to all other events.

The characteristic feature is the very sharp cut-off of the low-frequency side of the wave spectra. The energy diminishes by a factor 200:1 between 50 and 40 c/ks, or at a rate of 100 db's per octave. Waves in the generating area similarly show a sharp low-frequency cut-off, so sharp that there has been difficulty in resolving it. In fact the suggestion has been made by Phillips (personal communication) that a discontinuous function

$$E(f) \sim f^{-5} \quad \text{for } f \geq f^*; \quad E(f) = 0 \quad \text{for } f < f^*$$

might be an adequate presentation of the known facts.

The analysis of waves from distant sources offers the peculiar advantage that the sharp frequency front is drawn out in time over a number of days and so can be studied from an analysis of subsequent spectra.

We shall wish to compare our results with empirical knowledge concerning wave spectra in storm areas. Darbyshire (1952, 1955, 1961) has compiled such information over a period of 10 years; he suggests a relation of the form

$$E(f) = E(f_0) \exp -10.8[|f-f_0|(0.042 + |f-f_0|)^{-\frac{1}{2}}]$$

for

$$f > f^* = f_0 - 0.042,$$

and $E(f) = 0$ otherwise. Here f is the frequency in c/s. The energy is peaked at

$$f_0 = [1.94W^{\frac{1}{2}} + 2.5 \times 10^{-7}W^4]^{-1},$$

where W is the surface wind in knots. The peak energy in $\text{cm}^2/(\text{c/s})$ is given by

$$E(f_0) = 3.0H^2, \quad H = 0.247W^2,$$

where $H^2 = 8 \int_0^\infty E(f) df$ is the mean-square height ($8 \times$ variance) in cm^2 .

Darbyshire's empirical relations are plotted on figure 40. For frequencies slightly above the cut-off frequency, f^* , Darbyshire's empirical rule has the asymptotic form $E(f) \sim \exp - (f-f^*)^{-\frac{1}{2}}$ in some appropriate units. Neumann's (1953) spectrum gives an entirely different low-frequency cut-off, $E(f) \sim f^{-6} \exp - (f^{-2})$. The empirical laws are at best a very rough indication of the true situation. Darbyshire has modified his formulas to allow for a limited fetch. For any fetch above 100 n.m. the adjustment to the curves is negligible.

At frequencies below 50 c/ks the observed variation of energy density along the ridges is in fair accord (except for 20.3, 21.3 and 28.7 August) with the empirical curves, and suggests wind speeds of 30 to 50 knots. All this is very reasonable, but not surprising in as much as Darbyshire's curves are based on similar types of wave observations as ours (though not on waves from quite as distant storms).

(b) Geometric spreading

By a theorem due to Barber (1958) the spectral density $E(f, \theta)$ is the same at the receiver as in the generating area, even allowing for earth's curvature (but neglecting loss due to dissipation or non-linear effects).

The total spectrum $E(f)$ in the generating area is

$$E(f)_{\text{storm}} = E(f, \theta) 2\beta,$$

where 2β is the mean angular spread in the generating area. On the other hand the received spectrum is

$$E(f)_{\text{recorder}} = E(f, \theta) 2\alpha,$$

where 2α is the angular width (at the receiver) of that part of the storm which can be seen along great-circle paths. So

$$E(f)_{\text{storm}} = E(f)_{\text{recorder}} \beta/\alpha.$$

Now 2α is about 15° , for a storm near the antipole (and for a storm in the South Pacific) while β both from theory (Phillips) and observation (pitch-and-roll buoy) is of order

$$\beta = \cos^{-1}(c/W),$$

where c = phase velocity, and W = wind speed. Actually 2β varies from about 60° to about 150° , so there is a factor β/α of between 4 and 10 to take spreading into account, depending on c/W .

(c) *Attenuation*

At frequencies above 50 c/ks the observed ridge values deviate from Darbyshire's curves. We interpret this departure as the result of attenuation. The break-off point is remarkably sharp in most cases, thus indicating that attenuation is negligible below 50 c/ks and predominant above 60 c/ks. The result is of interest inasmuch as our observations refer to the most distant sources yet investigated. Clearly it would be preferable to measure the attenuation directly from a comparison of associated ridge cuts at various distance, Δ ; for the time being we shall have to be content with inferring the attenuation from a comparison of the predicted spectrum near the source and the observed spectrum at a distance.

Empirical knowledge concerning attenuation is virtually non-existent. Darbyshire (1952, p. 320) suggests a relation

$$\frac{1}{a} - \frac{1}{a_0} = 0.27 \frac{tf^3}{g} = \beta$$

to account for attenuation in the Atlantic; here a_0 is the amplitude at the source, and a the amplitude after the waves have travelled for a time t .

For small attenuation, $\beta a \ll 1$; for large attenuation $\beta a \approx 1$. Set $t = 4 \times 10^5$ s, $f = 0.05$ c/s and $\frac{1}{2}a^2 = E(f) \Delta f = 1 \text{ cm}^2(\text{c/ks})^{-1} (5 \text{ c/ks}) = 5 \text{ cm}^2$ for the case of small attenuation. This gives $\beta a = 0.04$, so that the attenuation is small, as expected. We expect the attenuation to be large for $t = 4 \times 10^5$ s, $f = 0.07$ c/s, $\frac{1}{2}a^2 = 20 \text{ cm}^2 (\text{c/ks})^{-1} (5 \text{ c/ks}) = 100 \text{ cm}^2$; these values give $\beta a = 0.5$. The conclusion is that the onset of appreciable attenuation as indicated on figure 40 is not out of line with previous experience.

14. MEAN MONTHLY SPECTRA

Average monthly spectra with great statistical reliability are plotted on figure 41. The number of daily spectra comprising the monthly means and the degrees of freedom, ν , of the combined spectra are as follows:

	May	June	Aug.	Sept.	Oct.
record days	12	13	18	23	16
ν	640	710	990	1250	880

The proportional variance is $2/\nu$, and the 95% uncertainty limits are roughly $1 \pm \sqrt{(8/\nu)}$.

The most remarkable feature is the flatness of the spectrum at low frequencies, resembling the output of a 'white-noise' generator. There is always the suspicion that this might be a noise level introduced into the recording or analysis and therefore carry no geophysical significance. However, the following evidence indicates the low-frequency portion of the spectra to be real: (i) at the high-frequency limit the raw spectrum of bottom pressure is lower by an order of magnitude than it is in the flat portion; (ii) previous analyses to frequencies as low as 0.3 c/ks, with the use of specially designed low-frequency instruments, gave results consistent with the present analyses (Snodgrass *et al.* 1962); (iii) the coherence between different instruments is high at the low-frequency limit (figure 4).

Still there remains some concern. Consider for example the spreading of the spectrum due to the limited duration of the record. The time record may be considered as a record of infinite length, multiplied by a function

$$f(t) = 1 \quad \text{between} \quad t = -\frac{1}{2}T \quad \text{to} \quad t = +\frac{1}{2}T,$$

and zero otherwise. The Fourier transform of this function is $T \sin \phi / \phi$, with

$$\phi \pi f T = \pi f N \Delta t = \frac{1}{2} \pi N x, \quad x = f / f_N,$$

where $f_N = (2\Delta t)^{-1}$ is the nyquist frequency for a sampling rate Δt , and N the number of observations in the time series. Then if $E(\phi)$ is the power spectrum of the infinite record, the spectrum for a record of length T is given by

$$\frac{1}{\pi} \int_{-\infty}^{\infty} E(\phi - \phi') \frac{\sin^2 \phi'}{\phi'^2} d\phi'.$$

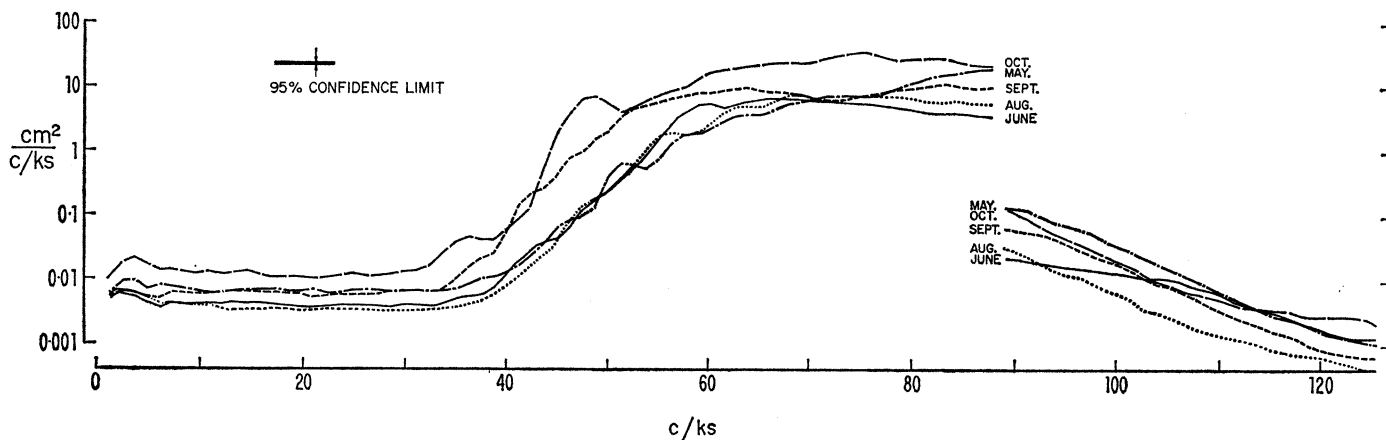


FIGURE 41. The average spectra for all records during the months of May, June, August, September, and October 1959, respectively. The 90 percent confidence limits for May are shown; for other months the expected variance is even smaller.

Suppose $E(\phi)$ is constant in the frequency interval x_1 to x_2 nyquists, and zero elsewhere. We wish to compute the spectrum at x_3 , well outside the range x_1 to x_2 . This permits us to replace $\sin^2 \phi'$ by its mean value, $\frac{1}{2}$. The computed spectrum at x_1 is then given by

$$\frac{1}{\pi^2 N} \int_{x_2 - x_1}^{x_3 - x_1} x^{-2} dx = \frac{1}{\pi^2 N} \left(\frac{1}{x_3 - x_1} - \frac{1}{x_2 - x_1} \right).$$

The expression in the parenthesis contains a numerical factor that increases with the width, $x_2 - x_1$, of the primary spectral band, and with the proximity of x_1 to this band. The ‘contamination’ varies inversely with the record length. For our analyses N is usually 3000, and the contamination from the energetic band into the low frequencies is of the order 10^{-4} . If the energetic band is coherent at the three instruments, then the contamination should be coherent also, and the foregoing argument (iii) is not convincing.

Since the observed energy density at low frequencies is typically 10^{-3} times the peak energy (figure 41) the contamination appears to be barely avoided. To check this conclusion, we have taken the very long record of 16 October ($N = 9000$), split it into three equal lengths, and compared the ratio of low-frequency energy density of the long record to the

mean of the three short records. If the low frequencies were purely the result of contamination, this ratio would be 1:3. If there is no contamination the ratio is 1. The observed ratio is 0.98.

The remarkable whiteness of the low-frequency part of the spectra leads naturally to the question of what might cause such a constant energy level. One would expect that non-linear interactions between the low-frequencies would ultimately lead to an equal distribution of energy. But there is hardly time or space for *local* interaction to be effective. At

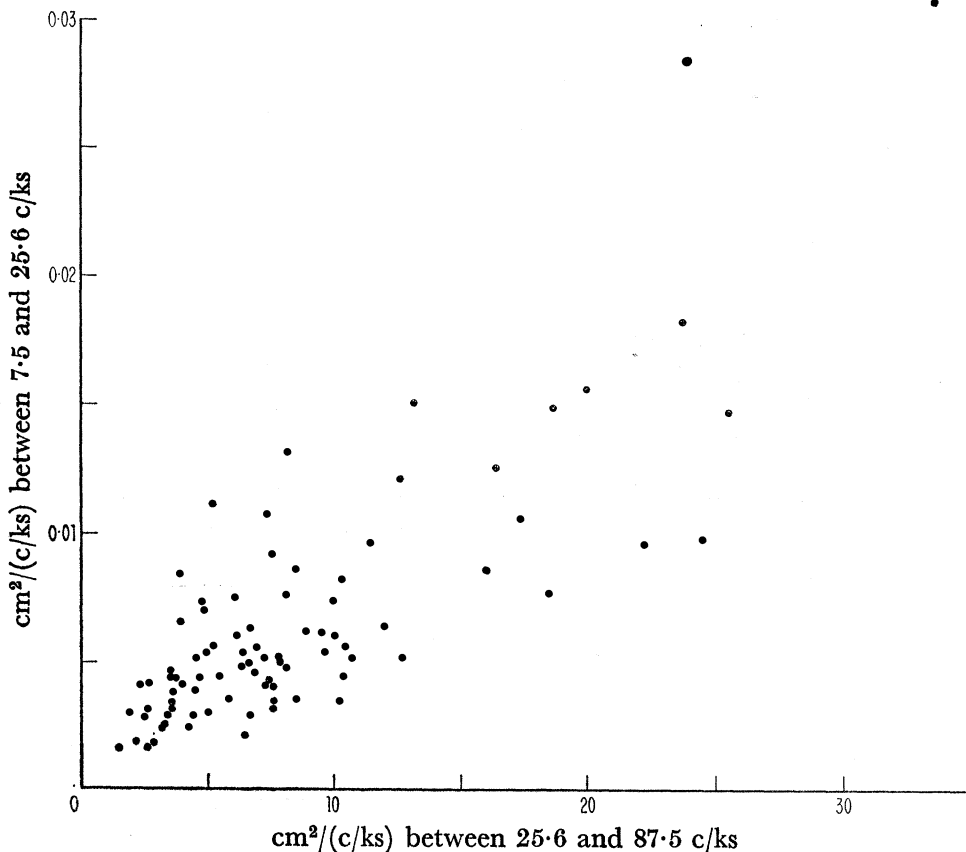


FIGURE 42. Average energy density over the flat part of the spectrum versus average energy density of the swell.

10 c/ks the wavelength is 3000 m in 100 m deep water. San Clemente Island is then only 10 wavelengths long at this depth and frequency. The wavelength is about 10000 m in the channel depths between the banks and the island, and off-shore features like the Tanner and Cortez Banks are even fewer wavelengths distant.

Previous studies have shown a relation between the intensities of the sea and swell and of the frequencies below the swell (Munk 1949; Tucker 1950). The suggestion was that the 'mean' level rose and fell with the variable heights of the incoming waves. Such a process can be interpreted as a 'diffusion' by non-linear processes from the high-energy, high-frequencies to the low-energy, low-frequencies, but this in itself would not necessarily account for the flatness of the low frequencies.

The day-to-day relation between the swell energy and low-frequency energy has been plotted in figure 42. There is some indicated relation, with the swell energy being about

1000 times the low-frequency energy (note the difference in scale). The two quantities were also plotted against time with the object of establishing any phase lags between the variable swell energy and the variable low-frequency energy. None was found. If the low frequencies had originated in the same source region as the swell it would have preceded the swell by a week.

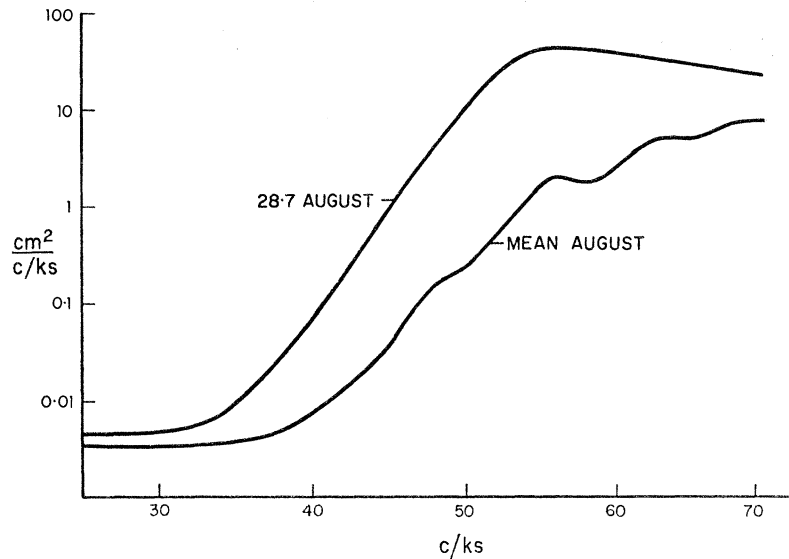


FIGURE 43. The mean spectrum for August and the 'ridge cut' associated with the storm of 28.7 August.

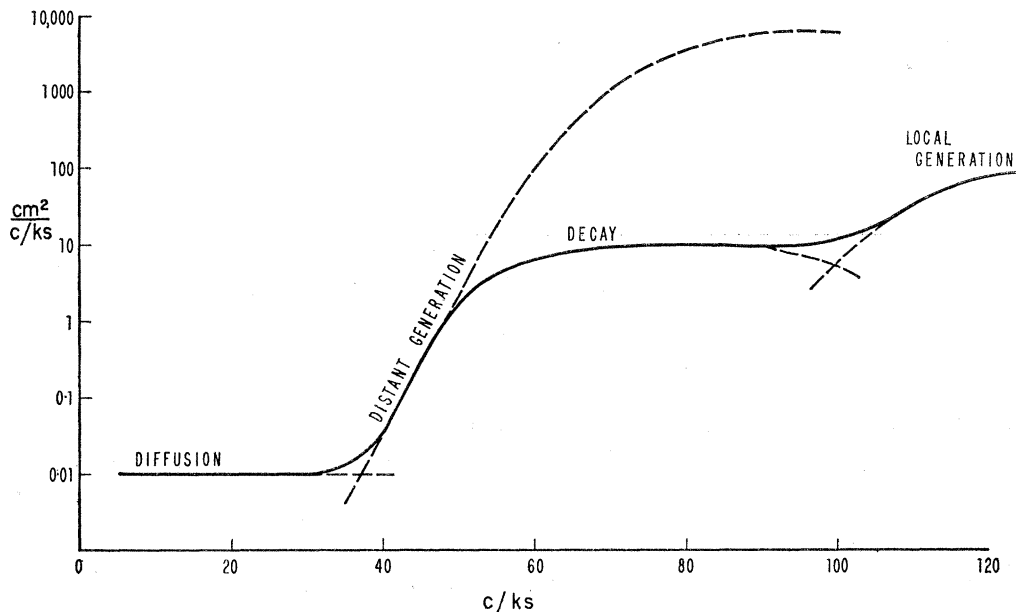


FIGURE 44. Schematic presentation of a mean monthly spectrum.

Above 35 c/ks the low-frequency tail of the swell spectrum rises sharply out of the flat spectrum, increasing by a factor of 10^3 in one octave (figure 41). Ultimately the recording of the low-frequency, low-energy forerunners of the swell is limited by the flat spectrum. For May and October the rising curve shows some peaks. These are the residuals of some strong spectral peaks on one particular day; such peaks would have been blurred out had records

been continuous throughout the month. Evidently the flank of the mean monthly spectrum is closely related to the energy along individual ridges (figure 40) but a more detailed comparison shows that the rise is steeper for the individual ridges (figure 43).

The sharp rise in the spectrum tapers off at 50 c/ks, and the spectral level becomes nearly flat between 75 and 90 c/ks. At even higher frequencies the spectrum is known to rise once again as a result of waves generated in nearby wind systems. In figure 44 we have portrayed what we believe to be the typical situation. The curve marked 'distant generation' is crudely representative of the type of spectra one might expect in the generating area. Above 50 c/ks the observed spectra fall below the expected generation spectra, and this indicates the importance of decay processes at these higher frequencies.

15. SCATTER AND ABSORPTION

The physical processes leading to attenuation are unknown. The direct effect of molecular viscosity is negligible. The last few years have seen a rapid development in the study of non-linear effects on wave motion; wave-wave interactions and wave-turbulence interaction have received particular attention. In general such interactions lead to the *scattering* of the incident wave energy into waves of different lengths and/or direction. Such interactions apply to the present study in a number of ways: forward scattering broadens the beam and augments the spectral peaks on the low-frequency side; backward scattering reduces the energy received at the station; scattering into high wave numbers permits molecular processes to become effective and thus ultimately leads to destruction of wave energy. The interactions are weak and difficult to demonstrate on a laboratory scale. The present measurements refer to the propagation of swell over 10^4 wavelengths.

(a) *The evidence*

(i) Attenuation (apart from the effect of geometric spreading) appears to be small at frequencies below 50 c/ks and predominant above 60 c/ks. This is evident both from individual ridge cuts (figure 40) and the monthly spectra (figure 41). In general the spectra level off at some fixed energy density. This suggests that the absorptive processes may be selective against the high energy rather than the high frequency. If the absorption were frequency controlled, we should expect the spectral peaks to be slightly shifted towards lower frequencies and accordingly the ridges lines would ultimately curve to the right. Yet there is no measurable deviation from straight lines. There is no substantial broadening of the ridge with increasing frequency (figure 45), so that the conclusion would have been similar had we plotted total energy under the ridge rather than energy density at the crest of the ridge.

(ii) The decay following the ridges is best studied by a series of cuts at fixed frequencies (figure 46). The energy rises rapidly to the summit and then decays gradually. For example, during 5 to 7 September at 50 c/ks, the energy rose by a factor of 30 in $\frac{1}{2}$ day, then decayed by a factor of 10 per day for the next 2 days. On 17 September at 45 c/ks the decay by a factor 10 takes place in 0.7 day. The most rapid decay is associated with the event of 12.4 May (factor of 10 in 0.4 day), but this appears to be an exceptional case (§11 (c)). We shall take $\frac{1}{2}$ day as the typical decay time, i.e. the time for the energy to decay by a factor e. The direction of the optimum point source remains fairly constant during the decay though there

appears to be a tendency to swing southward. The same information for October is shown in figures 20, 21 and 22, but here the directional *distribution* is included as well. Beam broadening is not appreciable during the early decay. For example, the signal from the hurricane of 23·2 October at 44 c/ks (figure 21) remains within a 10° sector during 27 and 28 October. On 29 October there is weak radiation from a 90° sector.

(iii) Some evidence concerning energy absorption can be inferred from the distribution of energy density along individual ridges as compared to mean monthly spectra (figure 43).

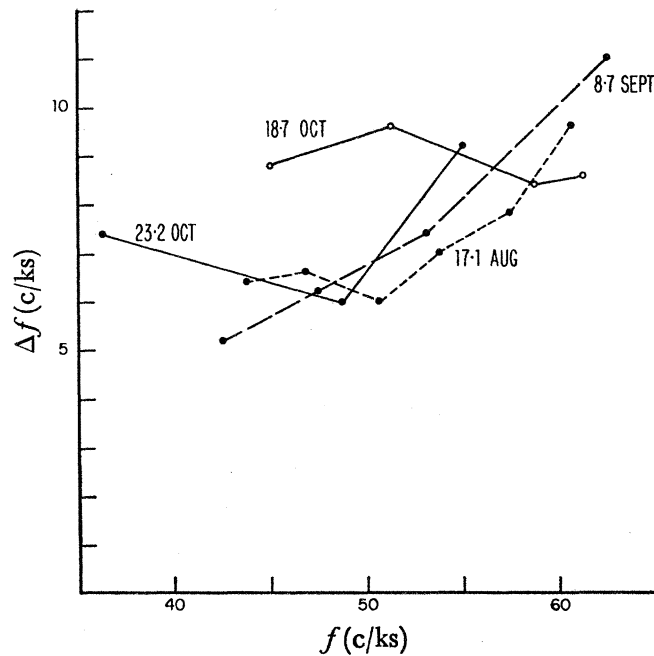


FIGURE 45. The effective ridge widths, Δf , defined by the relation $(\frac{1}{2}E_0) \Delta f = \int E(f) df$ where E_0 is the energy density at the crest of the ridge. For each of the four ridges, associates with the storms of 17·1 August, 8·7 September, 18·7 October and 23·2 October respectively, Δf was determined from successive spectra and plotted against ridge frequency.

(b) Scattering by waves

We shall first consider the evidence of attenuation commencing rather sharply at frequencies above 50 c/ks. Many, if not most, processes of attenuation discriminate against higher frequencies. One possible effect is the variation with frequency of the angular spread in the generating area. Wave generation is less directional at high frequency, and this would lead to further reduction from geometric spreading. The difficulty with this and other hypotheses is that they fail to account for the rather sharp cut-off and the flat energy density above the cut-off frequency. Non-linear processes depend on some power of the wave slope, k_0 , and this increases sharply both because of the rapid rise of the energy density, with frequency, and the dependence of k on f^2 . The quantity $k^2S(k)$ is the mean-square slope per unit wave number, and

$$k^3S(k) = k^3S(f) (df/dk) = 2\pi^2g^{-2}f^5S(f)$$

the mean-square slope per octave of wave number. This may be the pertinent dimensionless number. It rises precipitously from 1.6×10^{-10} at 40 c/ks to 6.2×10^{-8} at 50 c/ks.

One interesting possibility is the wave-wave interaction discussed by Phillips (1960). Let k_0 designate a representative (scalar) wave number for the trade wind waves, and assume these waves to be confined in a directional beam between south-east and north-east, from A to B in figure 47. According to Phillips, resonant interaction with k_0 requires that k_1 terminate along the figure-of-eight. The earliest interaction (left) is with the north-easterly trade sea, giving rise to a scattered wave towards the southwest. The latest interaction (right) is with the south-easterly trade sea, giving rise to a scattered wave towards the northwest.

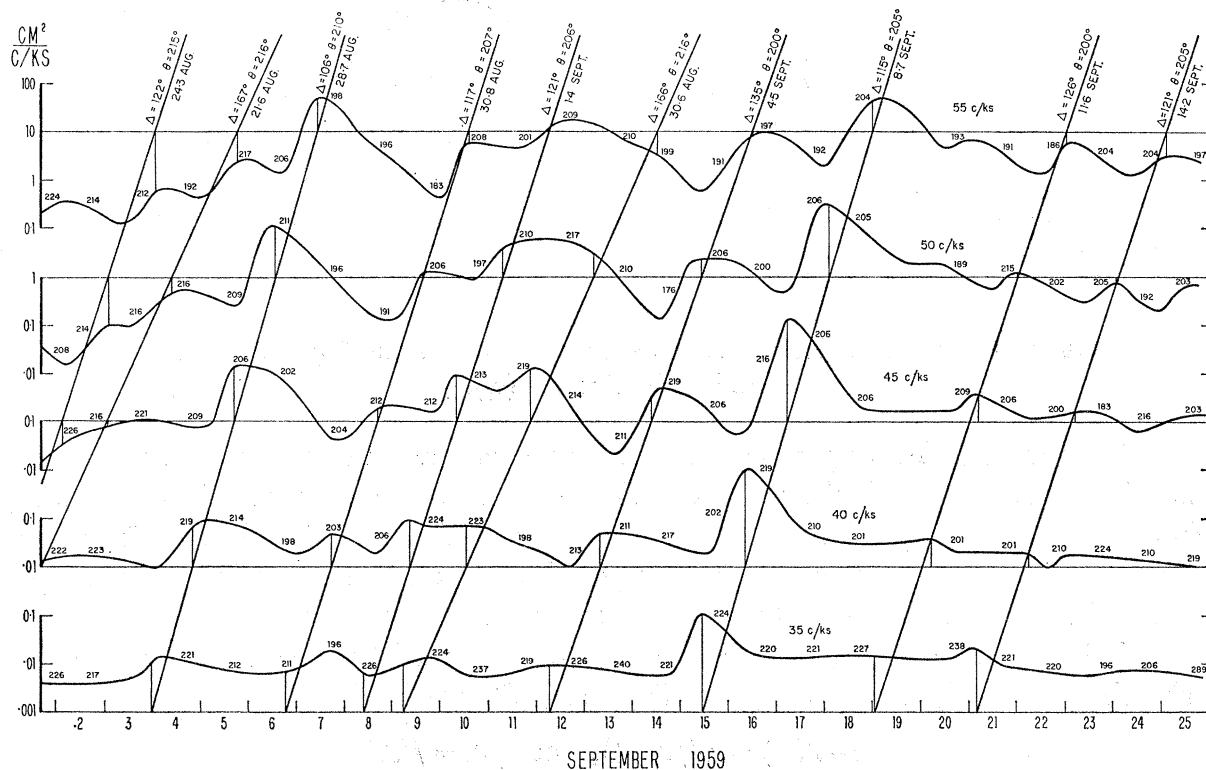


FIGURE 46. Energy densities at indicated frequencies for the period 1 to 25 September. Direction of the optimum point source are entered, and the principal ridge lines are shown. Compare with figures 15 and 16.

In the example k_1 varies from a value $0.26 k_0$ at the earliest interaction to $0.28 k_0$ at the latest interaction. The earliest interaction occurs then when k_1 is about $\frac{1}{4}$ of the lowest wave number, k_0 , in the trade wind sea, or when f_1 is $\frac{1}{2} f_0$. We estimate $f_0 = 100$ c/ks to be the low-frequency cut-off of the trade wind sea, and accordingly expect $f_1 = 50$ c/ks to be the lowest interacting frequency of southern swell. Thus the attenuation should commence sharply at some frequency near 50 c/ks, both because of the onset of resonant interaction and the sharp increase in the mean-square slope of the swell. We have here dealt with a special case of triplet interaction. In the general case there is interaction between four wave numbers. The discussion can also be generalized to allow for a range of wave numbers, k_0 , of the trade wind sea.

Hasselmann (1961) has given an expression for the interaction time, τ . The evaluation has not yet been accomplished, but it appears as if $f_0 \times (\text{mean-square slope of trade wind sea})^2$ is an estimate of τ^{-1} , subject, however, to an uncertainty by one or two orders of magnitude.

For a root-mean-square slope of 0.1 and a frequency of 0.1 c/s the interaction time is 10^5 s. The time required for a 20 s swell to cross the trade wind zone is also of the order of a day.

These results suggest then the hypothesis that the northern hemisphere is shielded from southern swell by scattering in the trade wind sea, and that only the low-energy low-frequency forerunners penetrate the northern oceans to any appreciable extent. The fact that the swell from the two northern sources (open circles, figure 33) show a comparable cut-off is evidence against this hypothesis.

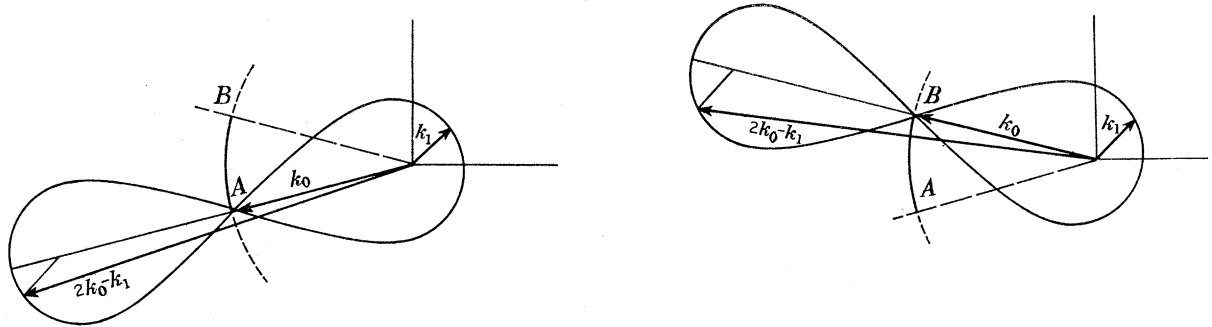


FIGURE 47. Resonance interaction between south-westerly swell (wave number k_1) and trade wind sea (k_0).

At higher frequencies k_0 approaches k_1 , and the wave-wave interaction leads to forward scattering under favourable circumstances. Thus a narrow beam is broadened by a following wind. In the case of dispersion this leads to a widening of the spectral peak in the frequency domain, inasmuch as the scattered low frequencies arrive simultaneously with the high-frequency waves that have travelled the direct route. Let Δ designate the distance along a great circle route, and Δ' the length of the scattered path. The 'direct frequency' f will arrive simultaneously with the scattered frequency, f' , provided

$$\Delta/V(f) = \Delta'/V(f'), \quad \text{or} \quad f\Delta = f'\Delta'.$$

Since $\Delta' > \Delta$, we have $f' < f$, and the peak widens towards the low-frequency side. For the simple geometry shown in figure 48, we have

$$\frac{f-f'}{f} = \frac{\Delta'-\Delta}{\Delta} = \frac{t'-t}{t} = 2 \sin^2 \frac{1}{2}\alpha = 2 \sin^2 \frac{1}{4}\theta, \quad (15.1)$$

where t, t' are the travel times of the direct and scattered waves, respectively. The geometric widening of the beam is then a first-order effect of forward scattering, and the frequency broadening a second-order effect. Even so, the frequency broadening offers a better opportunity for observing the effect (if any), because the frequency resolution is so superior to directional resolution. If the observed decay relative to the peak energy, E_0 , is the result of forward scattering, we find

relative energy, E/E_0	1	e^{-1}	0.1	0.01
days after peak arrived	0	$\frac{1}{2}$	1	2
α	0°	18°	26°	36°

Waves having 10% of peak energy arrive 1 day subsequent to the peak and come from $\pm 26^\circ$ relative to the direction of the direct arrival. This implies a considerable shift in direction

and broadening of the beam, and nothing of this sort is observed, except possibly at frequencies above 70 c/ks. We conclude that forward scattering plays a minor role. The decay as observed, may be related to generation by the decaying storm rather than to the scattered arrival of waves generated during peak intensity.

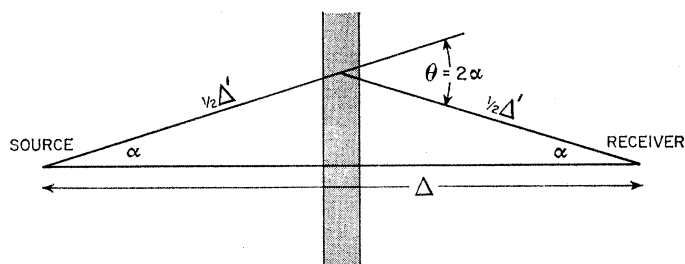


FIGURE 48. Waves are scattered through an angle θ by a scatterer lying along a line midway and normal to the line connecting source and receiver.

(c) *Scattering by turbulence*

Phillips (1959) has demonstrated that with reasonable assumptions turbulence is likely to lead to the forward scattering of swell. This opens the possibility of using waves as probes to estimate turbulence along the transmission path. Since the present measurements have failed to provide any positive evidence for forward scattering, all we can hope to accomplish is to place an upper limit to the turbulent intensity. It might be rewarding to search for the scattered arrivals with an array of adequate directional resolution.

Phillips separates the velocity field uniquely into a surface-induced contribution characteristic of the wave motion and a vorticity-induced contribution associated with the turbulence. The essential 'resonant interaction' is between an incident swell of (scalar) wave number k , and a scattering vector of magnitude

$$K = 2k \sin \frac{1}{2}\theta$$

associated with the vorticity field, to produce a scattered wave of the same wave number, k , as the incident wave, but at an angle θ with respect to it. The direction of \mathbf{K} is perpendicular to the line bisecting the directions of incident and scattered waves. Elements of turbulence large compared to the length of the swell lead to scattering through small angles. We may expect the turbulence to contain eddies of the same lengths as the incident swell, and this precludes the usual approximations for scatterers much greater or much smaller than the wavelength.

Phillips suggests with some caution the application of the similarity theory, and a turbulence spectrum of the order $\epsilon^{\frac{2}{3}}K^{-\frac{2}{3}}$ characteristic of the inertial subrange, where ϵ is the energy dissipation (ergs mass⁻¹ time⁻¹). The directional distribution of the scattered waves is conveniently described by the ratio, $s(\theta, k)$, of the mean energy flux developed in the scattered waves in the direction θ per unit angle per unit length of wave front per unit time, to the flux in the incident wave per unit length of wave front. This ratio is given by

$$s(\theta, k) = g^{-\frac{1}{2}}k^{\frac{5}{2}}\epsilon^{\frac{2}{3}}\sin^{-\frac{2}{3}}\frac{1}{2}\theta \quad (15.2)$$

except for θ near zero where the scattered wave interferes destructively with the direct waves. Equation (15.2) may be considered valid for $\theta > K_0/k$, where K_0 is the wave number

associated with the energy-containing components of the turbulence. The total scattered energy is of the order

$$\gamma(k) = 2 \int_0^\pi s(\theta, k) d\theta \approx 30g^{-\frac{1}{2}}k^{\frac{3}{2}}\epsilon^{\frac{3}{2}}. \quad (15.3)$$

On the basis of some diffusion experiments by Stommel, Phillips suggests $\epsilon = 10^{-5} \text{ cm}^2 \text{ s}^{-3}$, and this leads to $\gamma = 0.02$ per day for waves of frequency 50 c/ks. These waves have a group velocity of 12° latitude per day, and so cross the trade wind belt in 2 days. Total travel times are 10 days. Thus 4% or 20% of the energy is scattered, depending upon whether we consider scattering in the trades only, or along the entire transmission path. In the latter case, 80% of the energy comes along the great circle route, 20% is scattered and most of this through small angles, with a root-mean-square value estimated at 60° . The corresponding angle for the total field, direct plus scattered, is then 12° , and the associated delay, $t - t'$, is 1 h according to (15.1). This amount of forward scattering would then go unnoticed. But the waves are scattered in the surface layers where the value of ϵ might be an order of magnitude above average, and the scattering would then be just below the limits of detection with the existing angular resolution of our array.

(d) Island scattering†

Numerous island groups are in the path of the swell (figures 49 and 50). Typically these are atolls many times larger than the wave lengths here under consideration. A representative slope from the surface to several hundred fathoms is 26° . With this slope the water depth reaches half the wavelength at a distance of 1.03 wavelengths from the shore line. The steep slope suggests effective reflexion of the low frequencies, and forward scattering at the steep sides. Where the islands are dense, multiple reflexion may contribute to small angle scattering. Forward scattering leads to a broadening of the beam and a spreading of the dispersive spectral peaks.

The simplest theoretical construction is to compute the fractional shadow cast by the islands for waves from various directions (figure 51). On this basis the arrival of swell from the Indian Ocean is confined to two narrow windows. The window south of New Zealand is also limited by pack ice.

The shadow method assumes total absorption (by breaking) whenever the wave fronts intersect land, and total penetration otherwise. Reflexion and diffraction are then neglected. We shall consider these processes.

Geometric optics. In the case of specular reflexion from a smooth, cylindrical island of radius $a \gg \lambda$, the ratio of reflected to incident power (as in equation 15.2) is given by

$$s(\theta, k) = \frac{1}{2}ar^2(k) \sin \frac{1}{2}|\theta|, \quad (15.4)$$

where $r^2(k)$ is the energy reflectivity (assumed independent of incidence angle). There is no forward reflexion, $s(0, k) = 0$, and a maximum backward reflexion $s(\pi, k) = \frac{1}{2}ar^2$. The total reflected and absorbed power per unit frequency band are

$$2ar^2, \quad 2a(1 - r^2) \quad (15.5)$$

respectively.

† We are indebted to George Hess for the calculations in this section.



FIGURE 49. Azimuthal equidistant projection centred on San Diego, California. Some great-circle routes ($\theta = \text{constant}$) and equal distances along these ($\Delta = \text{constant}$) are indicated. The Tasman Sea and the region south of New Zealand provide two windows into the Indian Ocean, and these are partially obstructed by the Tongan and Taumotu island groups, respectively. The hatched area is shown on figure 50 on an enlarged scale. The South New Zealand window is further limited by the Antarctic pack ice.

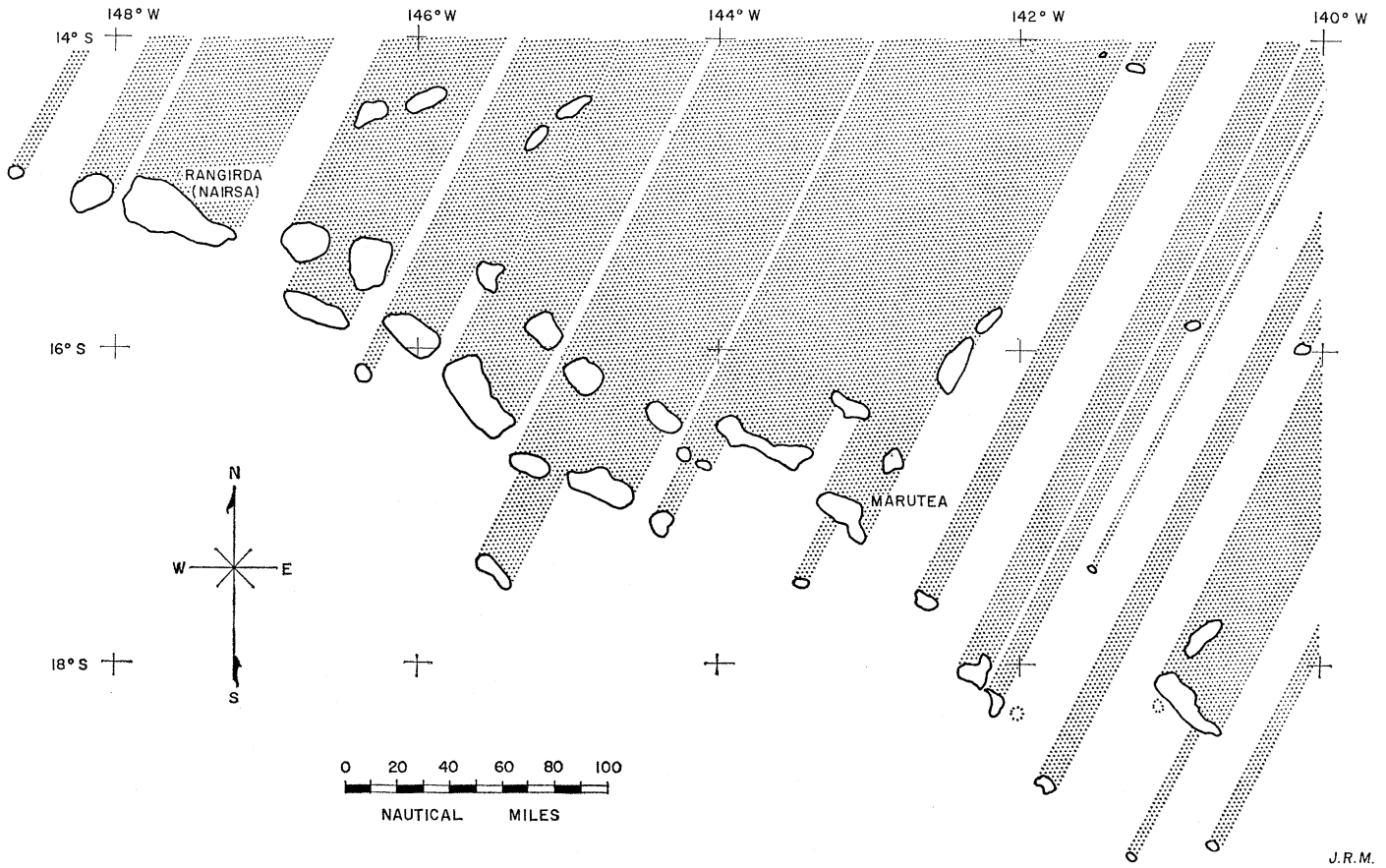
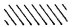



FIGURE 50. The wave 'shadow' cast by a portion of the Taumotu group for waves from $\theta = 216^\circ$ travelling towards San Clemente Island.

 PERCENTAGE OF SECTOR
 NUMBER OF ISLANDS IN SECTOR

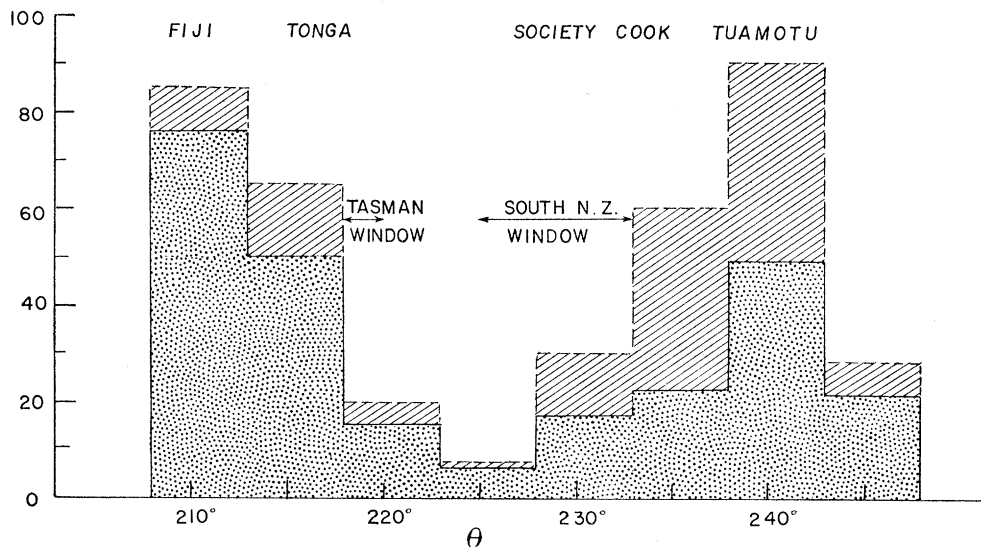


FIGURE 51. Numbers of islands north of 25° S in 5° sectors subtended at San Clemente Island, and the percentage of the sectors blocked by these islands.

The foregoing formulae assume the boundary of the island to be smooth over distances of the order of a wavelength. This is certainly not the case for a coral atoll. A more realistic model might be that of a *diffuse* reflector: the power received by an area of coast line is reflected into a direction β relative to the coast normal according to $\cos^2 \beta$ (β from $-\frac{1}{2}\pi$ to $\frac{1}{2}\pi$). Thus most of the energy is reflected normally outward regardless of the angle of incidence. The result is

$$s(\theta, k) = (8/3\pi) ar^2(k) \sin^4 \frac{1}{2}\theta \quad (15.6)$$

in place of (15.4): forward reflexion is reduced. Equation (15.5) is unchanged. The true situation is probably intermediary between the smooth and diffuse models.

Physical optics. The scattering of waves by cylinders has been treated by many authors (see, for example, Morse & Feshbach 1953, chapter 11). For the case that the wavelength is small compared to the circumference, the result is

$$s(\theta, k) \approx \frac{1}{2}a \sin \frac{1}{2}\theta + (2\pi k)^{-1} \cot^2 \frac{1}{2}\theta \sin^2 ka\theta.$$

The first term corresponds to total specular reflexion (equation (15.4) with $r = 1$), the second term to scattering. In a forward direction, where θ is very near 0, the scattered and incident waves interfere destructively (as in the case of scattering by turbulence) and one must consider the intensity of the total radiation field, not the scattered field separately. However, in practice it is proper to speak of the intensity of the scattered signal by itself provided one considers only values of $|\theta| > \pi/(ka)$. If the scattered radiation is averaged over islands of variable diameter (but always with the provision $ka \gg 1$) the rapid variation contained in the factor $\sin^2 ka\theta$ is averaged out, and the result is

$$s(\theta, k) = \frac{1}{2}a \sin \frac{1}{2}\theta + (4\pi k)^{-1} \cot^2 \frac{1}{2}\theta \quad (|\theta| > \pi/ka),$$

for the geometric reflexion and scattering, respectively. Note that the geometric term depends only on the radius of the island, and the scattering only on the wavelength. The corresponding 'cross-sections' are

$$2 \int_{-\pi}^{-\pi/ka} s(\theta) d\theta = 2a + 2\pi^{-2}a$$

so that 10% of the incident wave energy is scattered into the side lobes of the 'diffraction' term.

For a very rough estimate of the beam pattern we turn again to the simplified geometry of figure 48. The effect of geometric spreading (§ 12*b*) is to reduce the intensity at a distance Δ from the source in the ratio Δ_0/Δ , where Δ_0 is some constant depending on the *width* of the fetch and the directional pattern of radiation. The spherical shape of the earth is now neglected. The intensity at the receiver is $(\Delta_0/\Delta) \delta(\alpha)$, per unit transmitted intensity, where $\delta(\alpha) = 1$ for $\alpha = 0$, and 0 otherwise. The intensity incident on a scatterer is $\Delta_0/\frac{1}{2}\Delta'$, and the scattered intensity at the receiver is

$$\frac{\Delta_0}{\frac{1}{2}\Delta'} \frac{s(2\alpha, k)}{\frac{1}{2}\Delta'},$$

assuming uniform radiation of all scatterers. The shaded portion of figure 48 represents a band of islands of uniform 'density' N , so that $N \sec^2 \alpha d\alpha$ is the number of scatterers subtended between α and $\alpha + d\alpha$. The intensity at the receiver is then proportional to the expression

$$\frac{\Delta}{\Delta_0} I(\alpha) = \delta(\alpha) + \frac{2Nr^2(k) a \sin \alpha}{\Delta} + \frac{N}{\pi k \Delta} \cot^2 \alpha$$

with the three terms corresponding to the direct, reflected and scattered arrivals, respectively; r^2 is the reflectivity, and in the last expression $|\alpha| > \pi/(2ka)$. The geometric term is peaked for wide-angle scattering, the diffraction term for narrow-angle scattering. The mean-square angle from which the radiation arrives is

$$\overline{\alpha^2} = \frac{\int_0^{\frac{1}{2}\pi} \alpha^2 I(\alpha) d\alpha}{\int_{\frac{1}{2}\pi/ka}^{\frac{1}{2}\pi} I(\alpha) d\alpha} = \frac{N}{k\Delta} \frac{2(\pi-2)r^2ka + (\ln 2 - \pi^2/24)}{1 + (2Na/\Delta)(r^2 + \pi^{-2})}.$$

For a numerical example, we set $f = 50$ c/ks, hence

$$k = 10 \text{ km}^{-1}, \quad a = 5 \text{ km}, \quad \Delta = 100^\circ \approx 10^4 \text{ km}, \quad \text{and} \quad N = 50,$$

or $N/\frac{1}{2}\Delta = 10$ islands per 1000 km. Thus 10% is blocked by islands if there is no overlap. For these values the ratio $2Na/\Delta \approx 0.05$, so that

$$\overline{\alpha^2} \approx 0.057r^2 + 0.0014 \text{ rad}^2$$

due to reflexion and diffraction, respectively. At San Clemente Island we found $r^2 = 0.25$ for $f = 50$ c/ks (§10). For steep atolls the reflectivity is larger. Suppose $r^2 = 0.5$, then the root-mean-square angle subtended at the wave station is 10° . This is comparable to the previous estimate of scattering from turbulence, with the important difference that islands are associated largely with wide angle scattering and back scattering (due to reflexions), whereas in the case of turbulence most of the energy is scattered in a forward direction. There is also the distinction that islands are generally large as compared to the wavelengths, whereas the turbulent scales cover the entire spectrum.

(e) Absorption

Suppose the dissipation of wave energy in the Pacific basin were vanishingly small. Then with each major storm a new burst of energy would increment the existing high level until the mean energy was many times larger than the incremental energy from a single storm. In the extreme, the energy level would be almost uniform in time, and only minor fluctuations would accompany meteorological events. In fact the energy level associated with a major meteorological event raises the energy density from 10 to 100 times above the average background. The conclusion is that the absorption time, α^{-1} , is comparable or smaller than the typical time interval, τ , between major storms.

Our measurements permit us to formulate the problem in a semi-quantitative manner. Let $E_r(f)$ designate the energy density along the 'ridges' associated with given events. Then the energy density in the generating area is $GE_r(f)$ where G is a factor to allow for geometric spreading, the effect of dispersion having been compensated by measuring along a ridge. According to §13 (b), G is of the order of 10. Let W designate the *width* of the storm fetch, D the storm duration, and $V(f)$ the group velocity. The energy flux into the Pacific basin arising from a typical storm is $GDWV(f) E_r(f)$ per unit frequency band. The mean flux per unit time is $GDWV(f) E_r(f)/\tau$, where τ is the typical interval between major storms.

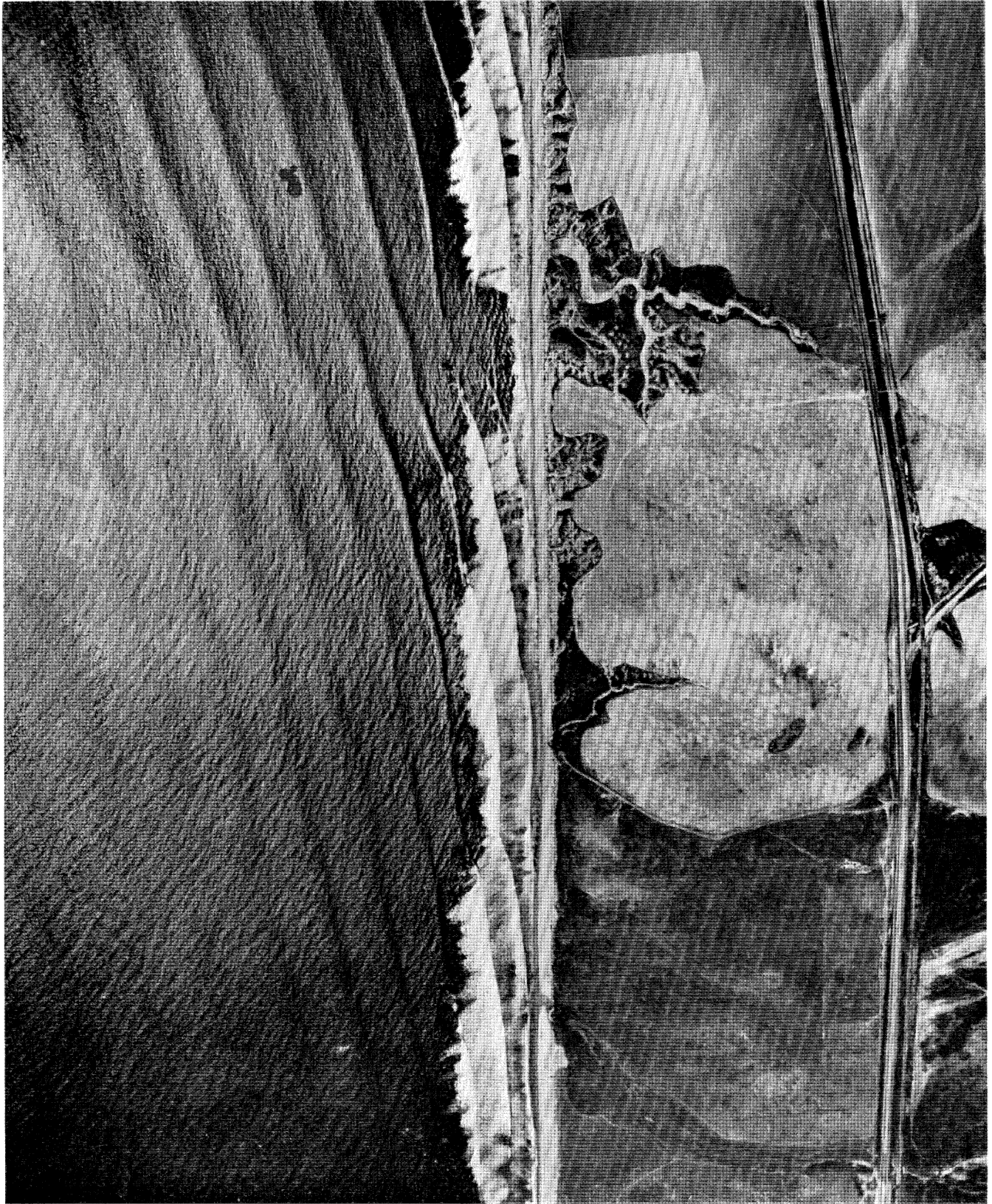


FIGURE 52. Aerial photograph of swell, breakers, and surf north of Oceanside, California, on 16 June 1944.

If $E_m(f)$ denotes the mean energy in the Pacific basin and A its area, then the absorption time is the mean total energy divided by the mean flux:

$$\alpha^{-1} = \frac{E_m(f) A}{GDWV(f) E_r(f)} \tau.$$

Set $A = 2 \times 10^8 \text{ km}^2$, $G = 10$, $D = 1$ day, $W = 10^3 \text{ km}$ and $\tau = 4$ days; furthermore set

$$V(f) = 1720 \text{ km/day}, \quad E_r/E_m = 10 \quad \text{for } f = 40 \text{ c/ks},$$

$$V(f) = 1150 \text{ km/day}, \quad E_r/E_m = 50 \quad \text{for } f = 60 \text{ c/ks},$$

in accordance with the results shown in figure 43. This gives $\alpha^{-1} = 4.6$ and 1.4 days, at 40 and 60 c/ks, respectively.

Suppose the energy is absorbed entirely at the boundaries. Then

$$\alpha^{-1} = \frac{A}{CV(1-r^2)},$$

where $C = 4.5 \times 10^4 \text{ km}$ is the circumference, and $r^2(f)$ the energy reflectivity. Setting $1-r^2 = 0.6$, 0.85 at 40 and 60 c/ks, respectively, in accordance with our measurements at San Clemente Island, we find $\alpha^{-1} = 4.3$ days and 4.5 days at the two frequencies. The conclusion is that absorption at the boundaries is a major factor, particularly at low frequencies.

16. THE SOUTHERN SWELL

Figure 52, plate 7, shows the arrival of a 16 s wave at Oceanside, California. The inferred off-shore direction is from 200° . In deep water these waves are above 2 ft. in height, but owing to their great length-height ratio they are amplified by a factor of about 3 before they break. The southern swell plays a vital role in the north Pacific basin, particularly along the coast of California and in Hawaii. Breaking somewhat obliquely along the California shore line the waves induce a northward littoral drift and sediment transport. Beaches represent a sensitive balance between this northward transport during the months April to September (the southern winter) and a southward transport associated with waves from Alaskan cyclones during the remaining year.

The results in the present study may help to explain some of the known qualitative features. The outstanding characteristics of the southern swell are its length, regularity and long-crestedness. It owes its length to the fact that it comes from the regions of the strongest winds, its regularity and long-crestedness to the great distance of the storms. Dispersion leads to a cumulative sorting of frequencies so that the effective relative width of the frequency band is of the order (storm fetch/storm distance), or (storm duration/travel time), whichever is larger. Typically these ratios are less than 10% for the very distant storms, and they may be further reduced when the storm approaches at group velocity (§11(c)). The regularity of the train is intimately connected to the inverse of this ratio, the 'Q' of the spectral peak. Long-crestedness, on the other hand, varies inversely with the angular spread (with the 'Q' of the beam pattern) and this parameter is large because distant storms subtend small angles. For swell from the Indian Ocean the beam width is

limited by the aperture of the New Zealand–Antarctic window. A typical beam width is 5° ($Q \sim 10$). The beam is not appreciably broadened by scattering along the transmission path. Refraction in shallow water leads to collimation, inasmuch as all rays within the beam tend to approach a direction normal to shore. Under favourable circumstances a single crest can break almost synchronously along several kilometres of beach front.

Owing to the great distance of the storm the wave energy at any given time is then concentrated in a narrow range of frequency and direction (the energy occupies a narrow region on wave-number space). Off-shore shoals of reefs may under favourable circumstances act as effective lenses to this nearly monochromatic radiation, and cause extraordinary focusing of energy into some small areas. We may thus interpret accounts of occasional destruction by swell in one locality when neighbouring areas were not particularly affected. Surf-boarding on southern swell is so popular because of the great regularity of the waves and the effectiveness with which favourable off-shore bars and shoals can concentrate the energy and ‘hump’ the waves prior to breaking.

We have displayed the dispersive wave trains as oblique ridges on a frequency-time plot of spectral density. Typically these ridges level off at $10 \text{ cm}^2/(\text{c/ks})$ above a frequency of 60 to 70 c/ks. The effective width is generally about 5 c/ks, so that the total energy under the ridge is of the order of $(10 \text{ cm}^2/(\text{c/ks})) (5 \text{ c/ks}) = 50 \text{ cm}^2$. This is the mean-square elevation. The mean-square amplitude is then $2 \times 50 \text{ cm}^2$, and the mean-square height

$$8 \times 50 \text{ cm}^2 = 400 \text{ cm}^2.$$

The associated root-mean-square height is 20 cm. In shallow water the concentration of energy flux leads to considerable enhancement. Let V_0, H_0 , designate group velocity and wave height in deep water, and V_b, H_b the corresponding quantities at a depth of breaking, $h_b \approx 2H_b$. Conservation of energy flux requires that

$$V_0 H_0^2 = V_b H_b^2 = \sqrt{gh_b} H_b^2 = \sqrt{g2H_b} H_b^2,$$

so that

$$H_b^3 = \frac{1}{2g} V_0^2 H_0^4 = \frac{g}{32\pi^2 f^2} H_0^4.$$

For $f = 0.07 \text{ c/s}$ (14 s period) and $H_0 = 20 \text{ cm}$, we find $H_b \approx 40 \text{ cm}$. But this calculation does not allow for the concentration of wave crests prior to breaking into narrow humps separated by long flat troughs. This distortion is associated with another doubling of crest-to-trough height, and $H_b = 80 \text{ cm}$ for the cited example. The higher ridges are associated with perhaps three times this value.

Island groups in the South Pacific effectively reduce the energy entering the North Pacific basin. But this cannot account for the sharp discrimination against frequencies above 60 c/ks as compared to the lower frequencies. We have suggested that scattering of the swell by the trade wind sea might be a factor. If this is the case, the intensity of swell in the northern ocean may depend as much on the momentary strength of the trades as on the severity of the winds in the source area. On a climatological time scale, a rapid rise in sea level and the subsequent submergence of some coral atolls would lead (or has led 4000 years ago) to a substantial increase in wave energy in the northern oceans. These remarks are speculative, but there is no doubt concerning the extent to which southern swell is blocked

by the equatorial belt. From the August Sea and Swell Charts (U.S. Navy Hydrographic Office) we find for 5° squares lying along the direction of swell travel:

latitude	longitude	
25 to 30° S	160 to 165° W,	57 % of swell from south-west, of which 88 % is high
20 to 25° S	155 to 160° W,	47 % of swell from south-west, of which 38 % is high
0 to 5° N	140 to 145° W,	0 % of swell from south-west

Wave statistics of this type are notoriously unreliable, but the contrast in observable swell is nevertheless noteworthy.

The severity of southern swell in any one season is limited somewhat by the extent of pack ice surrounding the Antarctic continent (figure 33). These are drifting fields of close ice, mainly consisting of relatively flat ice floes, the edges of which are broken and hummocked. The pack ice is kept in motion by winds and currents. It has in all months a well-defined northern limit, beyond which the great icebergs are found. These originate on the shelves at the shoreward side of the pack and drift through the pack ice. The pack ice is a severe barrier to the swell, though it is not impenetrable; the motion of the ice with typical swell frequencies has been detected with gravimeters located well inside the northern limits. In all events the penetration of swell from the India Ocean, and the generation in the Ross Sea could be severely limited by the pack ice in some years.

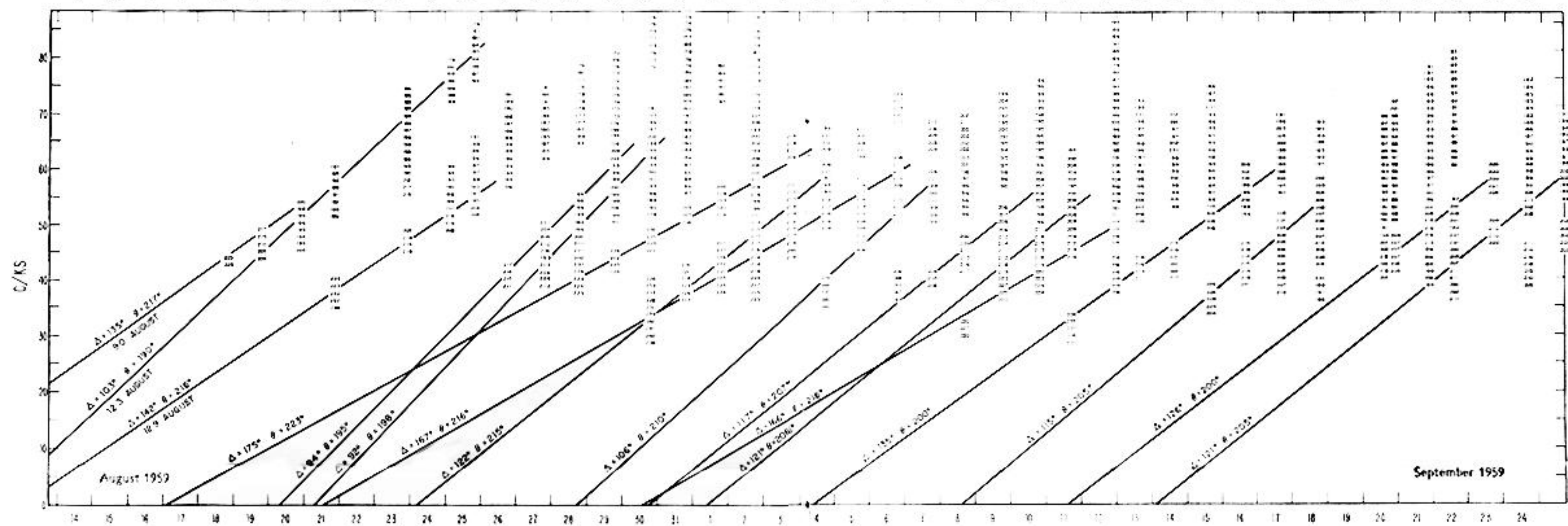
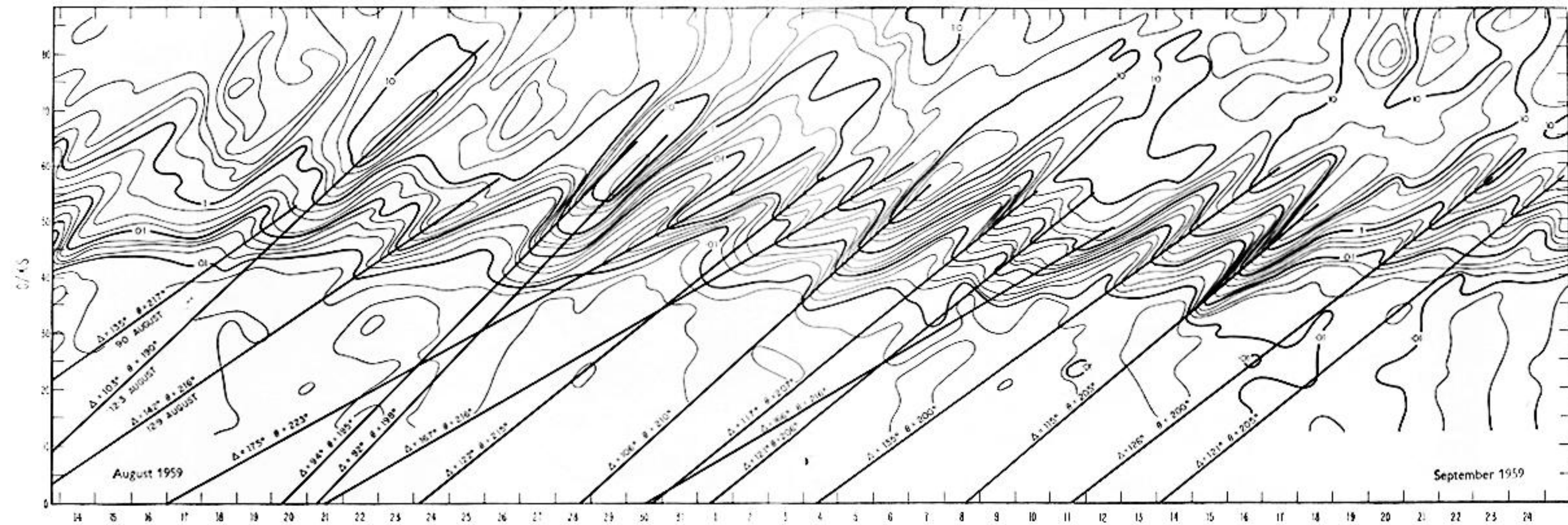
Some of the sources may be associated with katabatic winds along the Antarctic coast. Off-shore velocities up to 120 knots were measured during the International Geophysical Year in the sector 80 to 120° E. These winds may effectively remove the pack ice from some limited sector.

The Office of Naval Research, U.S. Navy has generously supported the experimental programme under contract Nonr-2216(04) administered by the David Taylor Model Basin. The extensive use of computers in the reduction of the observations has been made possible by a grant from the National Science Foundation.

REFERENCES

- Backus, G. E. 1962 *Deep Sea Res.* (in the Press).
 Barber, N. F. 1954 *Nature, Lond.* **174**, 1048.
 Barber, N. F. 1958 *N.Z. J. Sci.*, **1**, 330-341.
 Barber, N. F. & Doyle, D. 1956 *Deep Sea Res.* **3**, 206.
 Barber, B. F. & Ursell, F. 1948 *Phil Trans. A*, **240**, 527-560.
 Blackman, R. & Tukey, J. 1958 *Bell Syst. Tech. J.* **37**, 185.
 Cartwright, D. E. 1962 *The sea.* (In the Press.)
 Darbyshire, J. 1952 *Proc. Roy. Soc. A*, **215**, 299.
 Darbyshire, J. 1955 *Proc. Roy. Soc. A*, **230**, 560-569.
 Darbyshire, J. 1961 Conf. on Ocean Wave Spectra, Easton, Maryland.
 Dorrestein, R. 1960 *J. Geophys. Res.* **65**, 637-642.
 Eckart, C. 1953 *J. appl. Phys.* **24**, 1485-1494.
 Hasselmann, K. 1961 Conf. on Ocean Wave Spectra, Easton, Maryland: Prentice Hall. (In the Press.)
 Longuet-Higgins, M. 1957 *Proc. Camb Phil. Soc.* **53**, 226-229.
 Morse, P. M. & Feshbach, H. 1953 *Methods of theoretical physics.* New York: McGraw-Hill.
 Munk, W. H. 1949 *Trans. Amer. Geophys. Un.* **30**, 849-854.
 Munk, W. H. & Snodgrass, F. E. 1957 *Deep Sea Res.* **4**, 272-286.

- Munk, W. H., Snodgrass, F. E. & Tucker, M. J., 1959 *Bull. Scripps Inst. Oceanogr.* University of California, **7**, 4, 283-362.
- Neumann, G. 1953 *Tech. mem.* Beach Erosion Board.
- Ohman, J. 1955 National Telemetering Conf., Chicago, Illinois, May.
- Phillips, O. M. 1959 *J. Fluid Mech.* **5**, pt. II, 177-192.
- Phillips, O. M. 1960 *J. Fluid Mech.* **9**, pt. II, 193-217.
- Poindexter, R. W. 1952 Presentation AIEE-IRE Symposium, Long Beach, California, August.
- Prast, J. W., Calhoun, S. H., Hartloff, G. S. & Liske, G. W. 1955 National Telemetering Conf., Chicago, Illinois, May.
- Snodgrass, F. E. 1958 *Trans. Amer. Geophys. Un.* **39**, 1, 109-113.
- Snodgrass, F. E., Munk, W. H. & Miller, G. 1962 *J. Marine Res.* **20**, 3-30.
- Tucker, M. J. 1950 *Proc. Roy. Soc. A*, **202**, 565-573.



Above. FIGURE 16. For legend see in figure 13. Directions are plotted in figure 16.

Below. FIGURE 16. Direction of the optimum point sources, $\theta_0(f, t)$. The energy spectrum is plotted in figure 15.

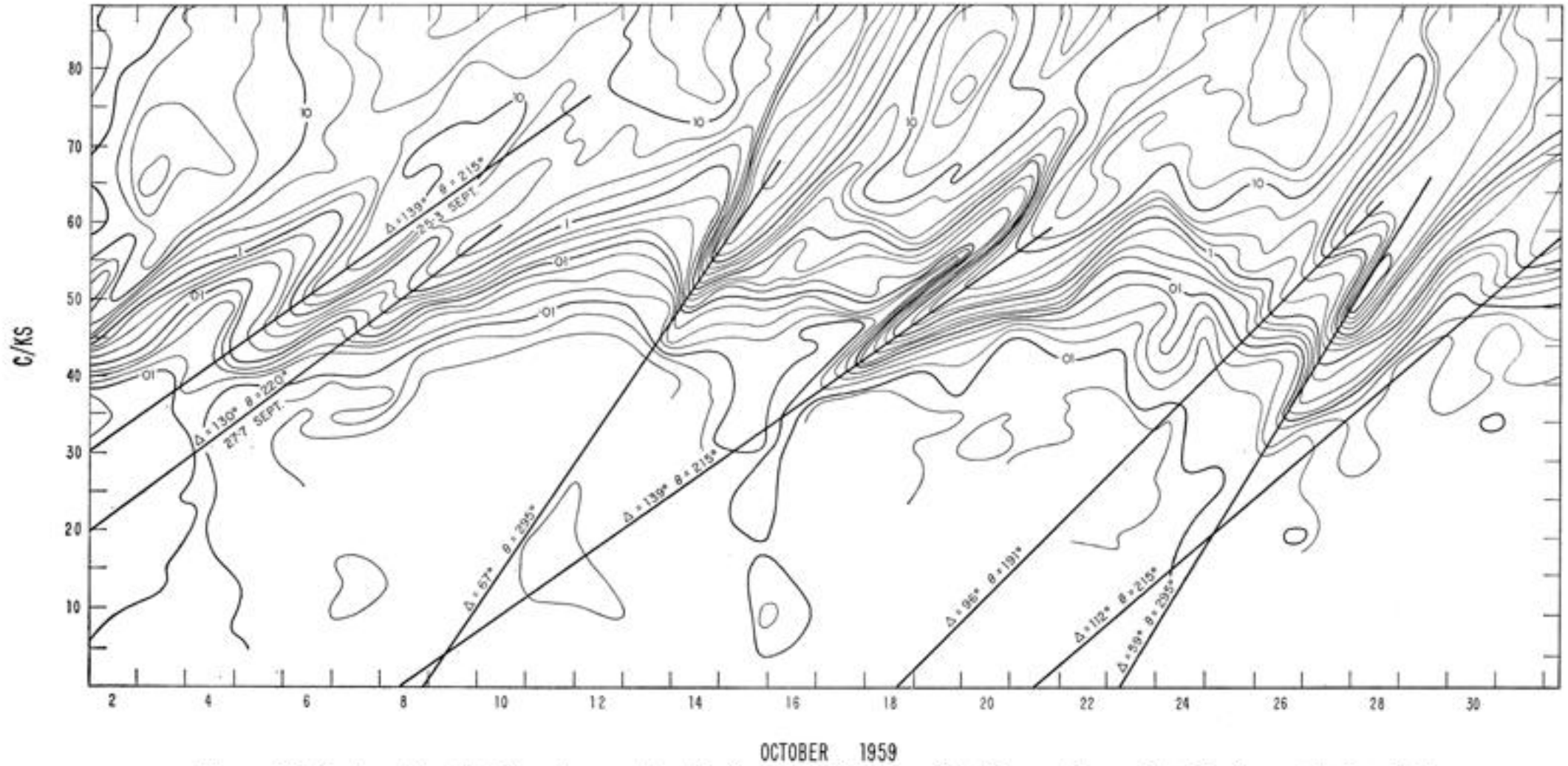


FIGURE 17. For legend see 13. Directions are plotted in figure 18. Cuts along fixed frequencies are plotted in figures 20, 21 and 22.

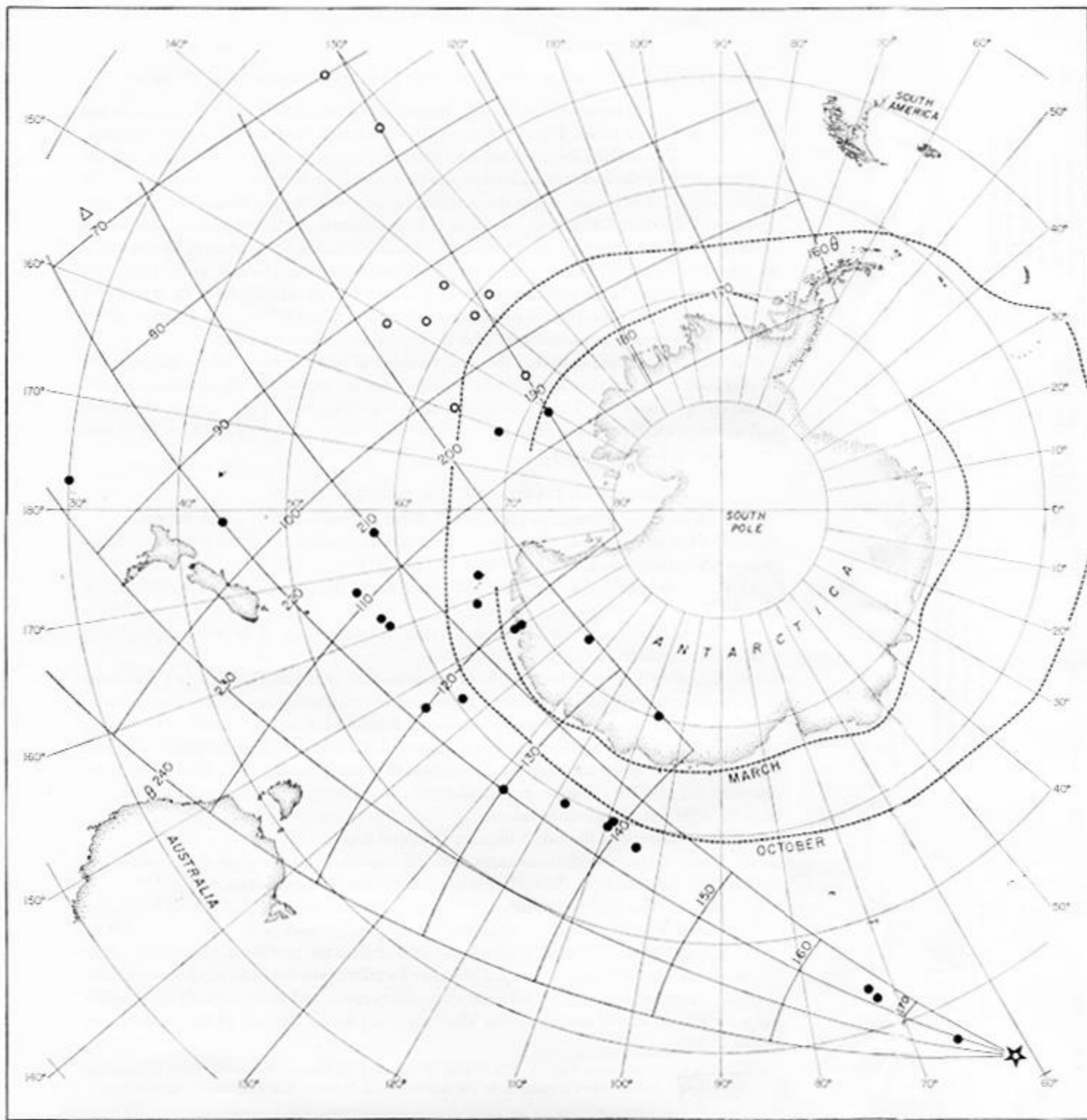


FIGURE 33. The sources as inferred from the wave observations plotted on an Antarctic Azimuthal Equidistance projection. The open circles refer to events for which weather observations were entirely lacking. The chart includes all observed events except those of 8-9 and 23-2 October, which occurred in the Northern Hemisphere. Great circle routes through San Clemente Island are plotted; they are labelled $\theta = 160^\circ, 170^\circ, \dots, 240^\circ$ giving the direction from San Clemente Island. The curves marked $\Delta = 70, 80, \dots, 180^\circ$ are distance in degrees from San Clemente Island. Average northern limits of pack ice for March and October are shown.

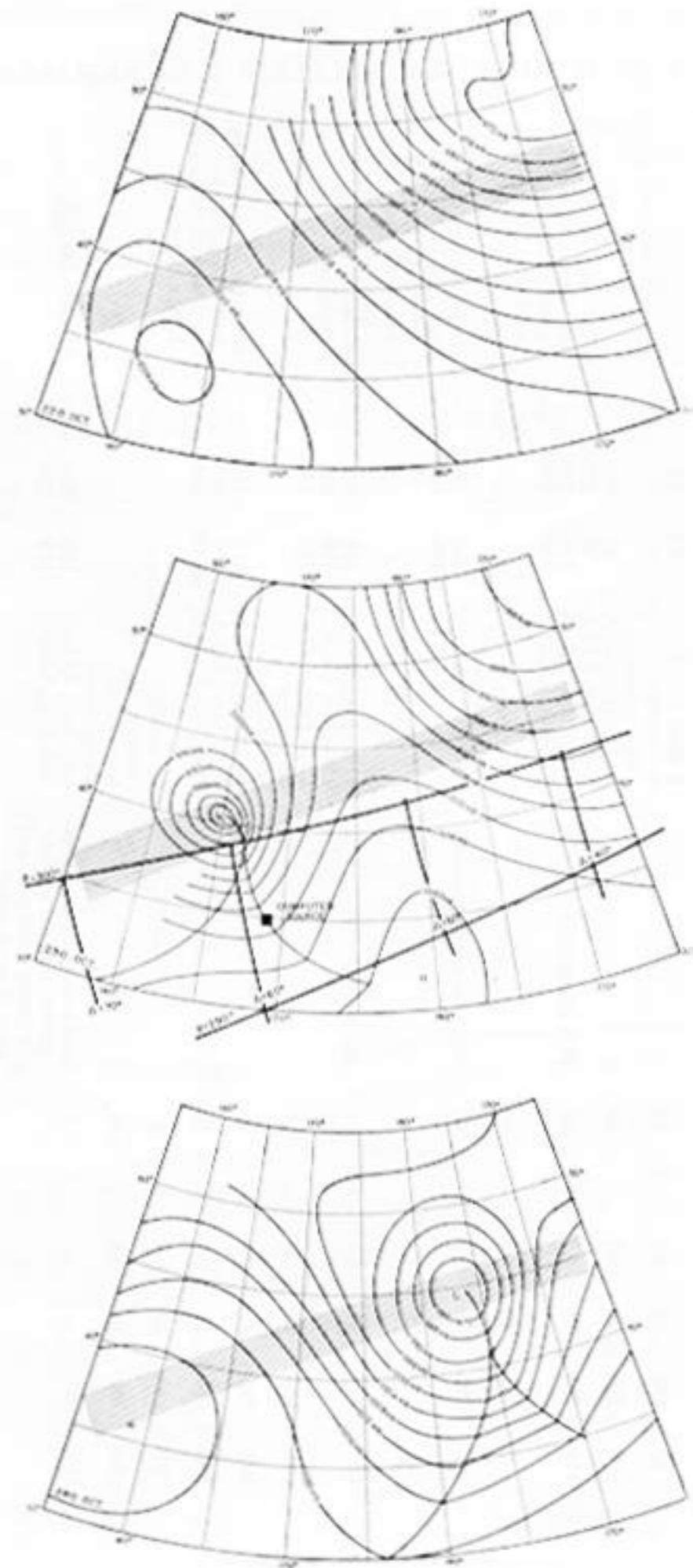


FIGURE 34. Portion of the Northern Hemisphere Weather Map of 3 successive days. The great circle routes bearing $\theta = 290$ and 300° from San Clemente island, and the distances $\Delta = 40, 50, 60,$ and 70° are indicated. The computed source was for 23-2 October at the position shown in the central figure. Shaded band indicates path of storm.

TABLE I

based on wave information							based on weather maps					
U.T. 1959	Δ ($^{\circ}$)	θ ($^{\circ}$)	W (knots)	duration (days)	$\frac{\delta\theta}{\delta f}$ ($\frac{\text{deg}}{\text{c/ks}}$)	$f_{\text{out-off}}$ (c/ks)	remarks	U.T. 1959	Δ ($^{\circ}$)	θ ($^{\circ}$)	W (knots)	remarks
7-4 May	84	228	30	1.0	+1.0	87	only later stages recorded	5 May, S.O.A.	98	227	—	—
9-4 May	92	192	33	0.5	-0.5	79	—	6 May, S.O.A.	93	228	—	—
11-5 May	96	220	36	0.7	—	59	—	no weather information	—	—	—	—
12-4 May	113	215	39	0.2	+5.0	63	very sharp ridge	11-25 May, S.O.A.	91	223	—	—
14-1 May	102	197	33	0.8	—	76	—	12-25 May, S.O.A.	96	220	—	—
7-0 June	107	190	38	1.0	—	60	only later stages recorded	12-25 May, S.O.A.	110	220	—	very short-lived storm south of New Zealand; see §11 (c) and figure 36
11-8 June	120	218	41	0.7	-1.0	53	gap in data	13-25 May, S.O.A.	92	212	—	—
12-3 June	95	189	35	—	—	72	—	no weather information	—	—	—	—
15-1 June	109	215	40	0.8	—	59	—	7-0 June, I.A.A.C.	109	190	—	fetch associated with Low at 75° S, 150° W, poorly documented; on 8-5 June fetch over Antarctica
18-4 June	106	195	41	0.6	—	56	—	7-5 June, I.A.A.C.	109	190	—	moved to right as expected
24-2 June	77	190	39	0.6	—	62	—	11-25 June, S.O.A.	113	220	—	—
26-5 June	70	192	39	0.9	—	>63	—	12-0 June, I.A.A.C.	110	222	—	—
9-0 Aug.	135	217	—	—	—	—	these two events are inadequately resolved on the frequency, time plot, and accordingly Δ and θ are uncertain, and the durations unknown	12-25 June, S.O.A.	120	230	—	—
12-3 Aug.	103	190	32	—	—	+70	—	no weather information	—	—	—	—
	2	216	34	0.8	—	63	—	14-25 June, S.O.A.	111	218	—	unusually long (1500 n.m.) well directed fetch
17-1 Aug.	175	223	41	0.7	—	54	usually low background	15-25 June, S.O.A.	110	215	—	two LOWs with favourable 1200 n.m. fetch
20-3 Aug.	94	195	35	0.7	—	60	$\delta E/\delta f$ on ridge less steep than Darbyshire's; this appears to be the case of a slowly developing storm	17-0 June, I.A.A.C.	92-110	198	—	—
								no weather observation	—	—	—	—
								8-25 Aug., S.O.A.	133	225	weak	970 mb LOW
								9-25 Aug., S.O.A.	118	225	25	—
								no weather information	—	—	—	—
								12-25 Aug., S.O.A.	145	222	—	965 mb LOW, 600 n.m. of favourable fetch. Lasts for 3 days, very stationary
								17-25 Aug., S.O.A.	155	210	35	winds of favourable direction between 965 mb LOW and 1035 mb HIGH; on following day direction much less favourable
								18-25 Aug., S.O.A.	170	220	—	—

TABLE I (cont.)

based on wave information							based on weather maps					
U.T. 1959	Δ ($^{\circ}$)	θ ($^{\circ}$)	W (knots)	duration (days)	$\frac{\delta\theta}{\delta f}$ ($\frac{\text{deg}}{\text{c/ks}}$)	$f_{\text{out-off}}$ (c/ks)	remarks	U.T. 1959	Δ ($^{\circ}$)	θ ($^{\circ}$)	W (knots)	remarks
21-3 Aug.	92	198	34	0.7	—	62	—	no weather observation	—	—	—	—
21-6 Aug.	167	216	36 31	1.2	—	62 >80	secondary hump	21-25 Aug., S.O.A.	165	221	35	strongest development at 21-25, duration 20-25 to 22-25; favourable winds beyond fetch (see figure 35)
24-3 Aug.	122	215	41	0.9	—	50	—	23-25 Aug., S.O.A.	120	216	30	—
28-7 Aug.	106	210	36	0.7	—	70	small $\delta E/\delta f$ on ridge	24-25 Aug., S.O.A.	114	215	35	—
30-6 Aug.	166	216	43	—	—	52	high background before and after ridge	28-25 Aug., S.O.A.	110	215	—	—
30-8 Aug.	117	207	42	1.0	—	57	—	30-25 Aug., S.O.A.	158	215	40	—
1-4 Sept.	121	206	41	1.0	—	53	—	31-25 Aug., S.O.A.	145	220	—	—
4-5 Sept.	135	200	40	1.0	—	58	—	30-25 Aug., S.O.A.	118	214	—	—
8-7 Sept.	115	205	41	0.9	—	54	—	31-25 Aug., S.O.A.	115	205	—	—
11-6 Sept.	126	200	40	0.8	—	60	—	1-25 Sept., S.O.A.	115	200	—	two storm areas
14-2 Sept.	121	205	40	0.7	—	49	—	1-25 Sept., S.O.A.	124	215	—	—
25-3 Sept.	139	215	35	0.7	—	63	—	4-25 Sept., S.O.A.	135	214	—	—
27-7 Sept.	130	220	45	0.9	—	44	—	8-4 Sept., S.O.A.	115	213	—	—
8-4 Oct.	139	215	44	0.7	—	57	—	10-25 Sept., S.O.A.	128	214	—	—
8-9 Oct.	67	295	40	1.0	—	61	severely refracted	11-25 Sept., S.O.A.	120	215	—	—
18-7 Oct.	96	191	42	0.6	—	63	—	14-25 Sept., S.O.A.	121	217	—	—
21-5 Oct.	112	215	—	1.4	—	—	—	24-25 Sept., S.O.A.	143	217	20	storm moved rapidly towards east, reached maximum between 24-25 to 25-25 Sept.; almost gone by 26-25 Sept.
23-2 Oct.	59	295	48	1.0	—	50	see §11 (a) regarding direction	25-25 Sept., S.O.A.	126	217	40	storm moved rapidly towards east, reached maximum between 24-25 to 25-25 Sept.; almost gone by 26-25 Sept.
								28-25 Sept., S.O.A.	120	230	—	moved from $\Delta = 142^{\circ}$, $\theta = 223^{\circ}$ on preceding day, when it was weak and ill-defined; weakened on 29th and strengthened on 30th.
								7-25 Oct., S.O.A.	135	215	—	955 mb Low, with intense winds from 7-25 to 9-25 Oct.
								8-25 Oct., S.O.A.	138	220	—	—
								9-25 Oct., S.O.A.	131	220	—	—
								10-25 Oct., S.O.A.	120	218	—	—
								10-0 Oct., U.S.W.B.N.H.	55	295	30	slowly moves eastward into gulf of Alaska
								no weather information	—	—	—	—
								21-25 Oct., S.O.A.	110	215	35	960 mb Low; favourable fetch
								22-25 Oct., S.O.A.	108	215	35	960 mb Low; less favourable wind direction
								23-0 Oct., U.S.W.B.N.H.	60	300	55	storm approaching at 35 knots along line of site (see figure 34).
								24-0 Oct., U.S.W.B.N.H.	53	300	—	—

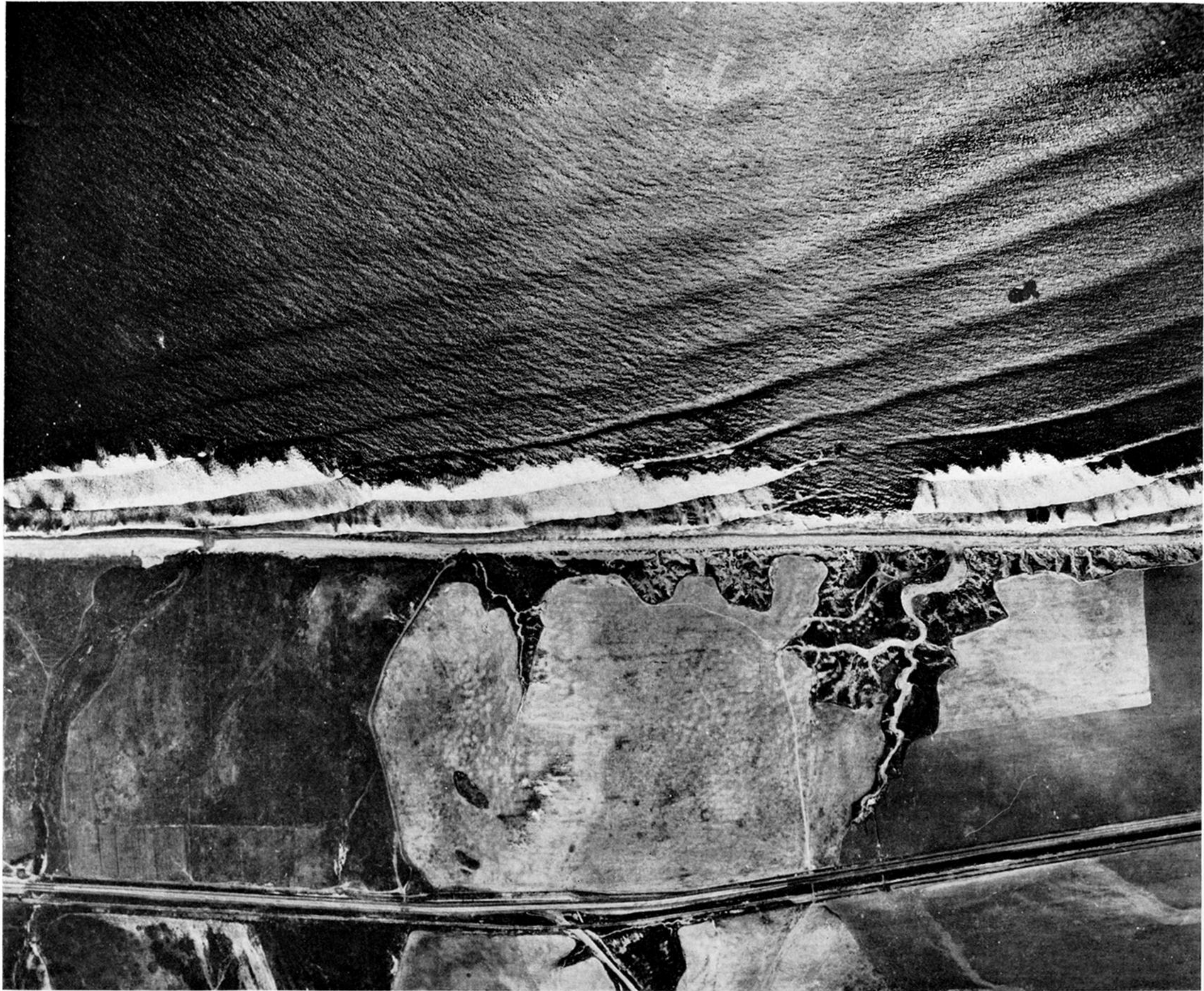


FIGURE 52. Aerial photograph of swell, breakers, and surf north of Oceanside, California, on 16 June 1944.